Rodrigo Augusto Ferreira Antunes

Licenciatura em Engenharia Física

The Role of Halouracils in Radiotherapy Studied by Electron Transfer in Atom-Molecule Collisions Experiments

Dissertação para obtenção do Grau de Doutor em Engenharia Física

Orientador: Prof. Doutor Paulo Manuel Assis Loureiro Limão-Vieira, Professor Auxiliar com Agregação, Faculdade de Ciências e Tecnologia da Universidade Nova de Lisboa.

Júri:

Presidente: Prof. Doutor António Manuel Nunes dos Santos
Arguentes: Prof. Doutor António Joaquim de Campos Varandas
Prof. Doutor Manuel Joaquim de Paula Maneira

Vogais: Prof. Doutor Nigel John Mason
Prof. Doutor Jorge Marques Gonçalves
Prof. Doutor Gustavo García Gomez-Tejedor

FACULDADE DE CIÊNCIAS E TECNOLOGIA
UNIVERSIDADE NOVA DE LISBOA

Setembro 2011

Acknowledgments

Professor Paulo Limão-Vieira for his constant support, encouragement, his exceptional supervision and his confidence in the work in which I have been involved, as well as the opportunities he has given me to visit several international groups.

Professor Manuel Maneira and all the members at the Molecular Physics, Plasmas and Applications research group, CEFITEC (Centre of Physics and Technological Research).

Diogo Almeida, Gonçalo Martins and Vítor Kokhan for their support, hard work and perseverance throughout the several stages associated with this thesis work.

Professor Nigel Mason and Dr. Samuel Eden for all their guidance and also for the hospitality during the visits to the Centre of Molecular and Optical Sciences, The *Open University*, UK.

Professor Gustavo García for his assistance and advising during the implementation of the experimental setup, and also for the hospitality during the visits to Laboratorio de Física Atómica, *Molecular* y de Agregados, CSIC, Madrid.

Dr Søren Vrønning Hoffmann at the Institute for Storage Ring Facilities, University of Aarhus, Denmark, for his supervision, discussion and assistance while working on the synchrotron radiation facility.

The Department of Physics, Universidade Nova de Lisboa for the provided working conditions.

The Portuguese Foundation for Science and Technology for the SFRH/BD/32271/2006 scholarship.

Professor João Lourenço for the advices, encouragement and friendship sustained over past years.

Rui Montenegro, Mauro Guerra, Diana Guimarães and all my colleagues and friends from Universidade Nova de Lisboa, not only for the support but also for the delightful moments shared over the years.

All my close friends and family.

Andreia Soares for the relentless love, encouragement and unconditional support.

And last, but not least, my loving Parents Mário Antunes and Isabel Antunes, for always being there, for their encouragement and support throughout these years.

Abstract

The role of ionising radiation as a source of damage to living tissues and cells has been recognized as a key issue regarding cellular DNA integrity and, ultimately, mutagenesis. The lethal effect of radiation, despite being most of the time undesired, can sometimes be useful, as is the case of radiation therapy. However, still the major concern in medicine is that only the cancerous cell material should be destroyed, keeping as much as possible healthy tissue unaffected. One way to control this damage seems to be the application of radiosensitizers that are incorporated into cancer cells. The cancer tissue doped with these radiation sensitizing molecules may be destroyed preferentially under radiation exposure, in very well defined places and even with radiation doses which may be low enough to prevent healthy cell material to be affected in the surrounding medium. This leads to nanodosimetry and so the sorts of interactions have now to be described at the molecular level. Upon irradiation, the most abundant secondary species produced along the radiation track are low energy electrons and so the study of electron induced damage to biological relevant molecules seems indubitably relevant.

The research described in this thesis covers for the first time the study of electron transfer on two halouracils (5-chlorouracil and 5-fluorouracil) and isolated DNA/RNA basis (thymine and uracil) by atom-molecule collisions. In order to investigate such molecules, a crossed beam experiment, comprising a neutral potassium beam and a biolomecular effusive beam, was improved and a time-of-flight mass spectrometer implemented allowing for the detection of negative ion formation following electron transfer processes in atom-molecule collisions. In these experiments the anionic fragmentation patterns and formation yields were obtained. These results are shown to be significantly different from the dissociative electron attachment (free electrons) results, unveiling that the damaging potential of secondary electrons to biomolecules can be somewhat underestimated. In addition, the halouracils sensibility to electron induced damage appears to be enhanced with respect to thymine and uracil, which may be extremely relevant as it reinforces their effectiveness as radiosensitizer molecules.

Keywords: radiosensitizers; electron transfer; negative ion formation; atom-molecule collisions; time-of-flight mass spectrometer.

Resumo

A radiação ionizante tem vindo a ser reconhecida como fonte preponderante de danos em células e tecidos vivos, principalmente devido à sua capacidade de interferir com a integridade do DNA das células. Existem porém situações em que os efeitos adversos associados à radiação podem ser úteis, nomeadamente no tratamento de patologias oncológicas através de técnicas radioterapêuticas. Estas técnicas, apesar de serem extremamente eficazes na eliminação de células cancerígenas, vão também ser responsáveis pela destruição de tecidos saudáveis nas áreas circundantes ao tecido tumoral. Uma forma de controlar estes efeitos indesejáveis parece ser a aplicação de moléculas radiossensibilizadoras, que ao serem incorporadas no tecido cancerígeno o vão tornar mais sensível à radiação. Desta forma poderá ser possível aplicar doses mais reduzidas de radiação, salvaguardando assim os tecidos saudáveis, sem comprometer a eficácia na destruição dos tecidos oncológicos. Estamos assim perante aspectos de nanodosimetria e o tipo de interacções são descritas a nível molecular.

Neste contexto, parece ser importante perceber que mecanismos estarão, a nível molecular, na origem dos danos estruturais provocados pela radiação ionizante, não só nas moléculas constituintes do DNA mas também nas moléculas radiosensibilizadoras (halouracilos). Sabendo que após a irradiação, as espécies secundárias mais abundantes produzidas ao longo da faixa de radiação são electrões de baixa energia, o estudo de danos induzidos por interações entre electrões secundários e moléculas de interesse biológico parece ser de extrema relevância.

A pesquisa descrita nesta tese aborda pela primeira vez, a formação de iões negativos por transferência de electrões, em colisões átomo-molécula, de dois halouracilos (5-Clorouracilo e 5-Flúoruracilo) e de duas bases isoladas de DNA/RNA (timina e uracila). Para investigar tais moléculas, foi implementado um dispositivo experimental de feixes moleculares cruzados, no qual se utilizaram um feixe neutro de potássio e um feixe efusivo de biomoléculas. Para detectar as espécies aniónicas resultantes dos processos de transferência de electrão, foi construído um espectrómetro de massa do tipo tempo de voo. Assim, foram obtidos experimentalmente os padrões de fragmentação para a formação de iões negativos e as respectivas secções eficazes relativas. Os resultados apresentam, no entanto, diferenças significativas relativamente aos obtidos por captura electrónica dissociativa (electrões livres), evidenciando que o potencial dos electrões (provenientes de um átomo) para provocar danos a nível celular poderá ser maior do que previsto anteriormente. Foi ainda possível verificar que, comparativamente com a timina e o uracilo, os halouracilos são mais susceptíveis de ser deteriorados por acção dos electrões de baixa energia, o que reforça o papel destas moléculas como radiossensibilizadores.

Palavras-Chave: radiosensibilizadores; transferência de electrões; formação de iões negativos; colisões átomo-molécula; espectrómetro de massa do tipo tempo de voo.

Contents

Acknowledgments V
Abstract VII
Resumo IX
Contents XI
Figures XV
Tables XIX
Acronyms and symbols XXI

Chapter 1 Introduction 1

1.1 Radiation effects on biological systems 1
1.2 Direct and indirect DNA damage 3
1.3 Electron transfer processes 5

Chapter 2 Collision Theory and Ion Pair Formation 9

2.1 Two-Particle Collision 9
2.1.1 Born-Oppenheimer approximation: Adiabatic Framework 10
2.1.2 Born-Oppenheimer approximation: Diabatic Framework 12
2.1.3 Landau-Zener model 16
2.1.4 Atom-Atom Collisions 18
2.2 Atom-Molecule Collisions 21
2.2.1 Atom Rigid-Molecule Collisions 21
2.2.2 Frank-Condon Model 22
2.2.3 Surface hopping trajectory method 23
2.3 Final remarks 28

Chapter 3 Experimental Setup 29

3.1 Apparatus Overview 30
3.2 Projectile Beam 33
3.2.1 Potassium Oven/Charge Exchange Oven 33
3.2.2 Potassium Ion Source 34
3.2.3 Deflecting Plates 36
3.2.4 Langmuir-Taylor Detector 36
3.2.5 K Collimation Slit 37
3.2.6 Beam Characterization and Optimization 38
3.2.6.1 Ion Source Temperature 38
3.2.6.2 Potassium Oven Temperature 38
3.2.6.3 Beam Energy 39
3.2.6.4 Energy Spread and Functional Dependence 41
3.3 Target Beam 43
3.3.1 Biomolecules Oven 43

3.3.2 Heating system 44
3.3.3 Liquid Sample System 44
3.3.4 Biomolecular Beam Collimation Slit 45
3.3.5 Baking System 45
3.4 Time-of-Flight Mass Spectrometer 46
3.4.1 Introduction 46
3.4.2 Dual-Stage Linear Time-of-Flight 47
3.4.2.1 Time-of-flight Equation 48
3.4.2.2 Mass Resolution 51
3.4.2.3 Spatial distribution 52
3.4.2.4 Kinetic Energy Distributions 55
3.4.2.5 Temporal Distributions 56
3.4.2.6 Overall Resolution 57
3.4.3 Implemented TOF 58
3.4.3.1 Extraction System 58
3.4.3.2 Drift Tube 60
3.4.3.3 Channeltron Detector 60
3.4.4 System Characterization and Optimization 61
3.4.4.1 TOF Characterization 61
3.4.4.2 Experimental Acceleration Voltage 63
3.4.4.3 Experimental Einzel Lenses Voltage 65
3.4.4.4 Mass Calibration 66
3.5 Acquisition System 70
3.5.1 HP Pulse generator 70
3.5.2 Jordan Pulse Generator 70
3.5.3 Ortec Pre-Amplifier 71
3.5.4 FastComtec Acquisition Board 71
3.5.5 LabView program 73
3.5.6 Operation Mode 74
3.5.6.1 Pulsed operation 75
3.5.6.2 Extraction Delay 76
3.6 Vacuum System 78

Chapter 4 Nitromethane 81

4.1 Introduction 81
4.2 Experimental Conditions 83
4.3 Results and Discussion 85
4.4 Conclusion 95

Chapter 5 Thymine and Uracil 97

5.1 Introduction 97
5.2 Experimental conditions 99
5.3 Results and Discussion 102
5.4 Conclusions 119

Chapter 6 5-Chlorouracil and 5-Fluorouracil 121

6.1 Introduction 121
6.2 Experimental conditions 124
6.3 Results and Discussion 126
6.4 Conclusions 140

Chapter 7 Conclusions and Future work 143

7.1 Experimental setup 143
7.2 Experimental results 143
7.2.1 Nitromethane 144
7.2.2 Thymine and Uracil 145
7.2.3 Chlorouracil and fluorouracil 146
7.3 Future work 148

References 151

Figures

Figure 1.1 - Chronological diagram of radiation induced damage 2

Figure 2.1 – Schematics of the potential energy curves: adiabatic states E_1 and E_2 - full curves; diabatic states H_{11} (covalent) and H_{22} (ionic) - dashed curves, where R_c designates the crossing radius 15

Figure 2.2 - Simplified representation of the high velocity collision trajectories involving an alkali atom (A) and an halogen atom (B). The impact parameter b is given by $R_C/\sqrt{2}$ 17

Figure 2.3 - Approximated diabatic potential energy curves for the lowest diabatic sates of $Na - I$. V_{cov} and V_{ion} are the diabatic potentials corresponding to the covalent and ionic electron configuration respectively. ΔE is the difference between the ionization potential Na and the electron affinity of I [12]. 18

Figure 2.4 - Trajectories on the ionic surface for the $Na^+ + Br_2^-$ system at impact parameter b = 2 A, and collision velocities (a) 4×10^3 ms^{-1}, (b) 5×10^3 ms^{-1}, (c) 10^4 ms^{-1}, (d) 2×10^4 ms^{-1}, and (e) 4×10^4 ms^{-1}. The dashed line denotes the seam between the covalent and ionic surfaces. All trajectories are assumed to switch to the ionic surface at $R = R_c$ and at the equilibrium bond length, $r = r_e$, of the Br_2 molecule, but the probability of return to the covalent surface is a decreasing function of the coordinate R at the point at which the trajectory re-crosses the seam [19]. 24

Figure 2.5 - Schematic neutral and anionic potential energy curves for a generic halogen molecule BB 26

Figure 2.6 - Reduced total cross sections: F_1 defines the atom-atom interaction; F_2 defines the atom rigid-molecules interaction and F_3 defines the atom-molecule interaction considering 27

Figure 3.1 - Experimental schematics: a) Potassium oven; b) Charge exchange oven; c) Potassium ion source; d) Deflecting plates; e) Langmuir-Taylor detector; f) Bio oven; g) TOF mass spectrometer 30

Figure 3.2 - Charge exchange schematics 31

Figure 3.3 - Charge exchange source: a) Charge exchange oven; b) Potassium oven; c) K^+ Ion source; d) Deflecting plates 33

Figure 3.4 - K^+ Ion Source 34

Figure 3.5 - Ion source support: a) Ion source 35

Figure 3.6 - Langmuir-Taylor detector 37

Figure 3.7 - Dependence of beam intensity as function of the potassium oven temperature 39

Figure 3.8 - Dependence of beam intensity with respective acceleration energy 40

Figure 3.9 - SIMION simulation: a) Ion source; b) Charge exchange oven; c) Collimating slit; d) Collision plane; e) Potassium beam 41

Figure 3.10 - Biomolecules' oven structure: a) Biomolecules' oven; b) Heating lamp; 43
Figure 3.11 - Biomolecules' Oven: a) Capillary tip; b) Outer Body; c) Container..... 44
Figure 3.12 - Basic TOF configuration 46
Figure 3.13 - Dual-Stage TOF mass spectrometer 47
Figure 3.14 - Single-stage TOF focal plane 53
Figure 3.15 - Comparison of single-stage (a) and dual-stage (b) extraction 53
Figure 3.16 - Two ions with different initial kinetic energies 55
Figure 3.18 - Extraction system: a) Extraction region; b) Acceleration region; c) Einzel lens; d) Deflecting plates; e) Flight tube..... 58
Figure 3.17 - Schematics of the implemented TOF spectrometer 58
Figure 3.19 - TOF extraction system electrical connections 59
Figure 3.20 - Schematics of channeltron pulsed mode electrical connections for negative ion detection 60
Figure 3.21 - Energy resolution dependence with the ion kinetic energy release 62
Figure 3.22 - NO_2^- peak of nitromethane mass spectrum at different acceleration voltages..... 64
Figure 3.23 - NO_2^- peak of the nitromethane mass spectrum at different einzel lens voltages 65
Figure 3.24 - TOF calibration curve (3º Iteration) 68
Figure 3.25 - Nitromethane anions TOF mass spectrum assignment from the collision of an effusive nitromethane beam and a 100eV neutral potassium beam. 69
Figure 3.26 - MCDWIN Software..... 72
Figure 3.27 - Labview program control layout 73
Figure 3.28 - Acquisition Layout 74
Figure 3.29 - Acquisition system time diagram 75
Figure 3.30 - Nitromethane TOF mass spectra in pulsed and continuous operation modes 76
Figure 3.31 - Nitromethane partial spectra with different collision delays for a..... 77
Figure 3.32 - Vacuum system schematics 78
Figure 4.1 - Three-dimensional schematic representation of nitromethane molecule..... 81
Figure 4.2 - Nitromethane TOF anion spectrum at a collision energy of 183 eV [27]. 85
Figure 4.3 - Nitromethane TOF anion spectra at three collision energies..... 86
Figure 4.4 - Nitromethane Partial Cross Section..... 87
Figure 4.5 - Schematic potential energy curves taken from [45] for neutral ground-state CH_3NO_2 and the two lowest-lying anion states, $^2B_1(\pi^*)$, and $^2A_1(\sigma^*)$ 90
Figure 4.6 - Negative ion TOF mass spectrum of K + CD_3NO_2 at 100 eV collision energy 92
Figure 5.1 - Schematic representation of a) Thymine and b) Uracil. 97
Figure 5.2 - Thymine TOF anion mass spectra at 30, 70 100 eV collision energies..... 104
Figure 5.3 - Uracil TOF anion mass spectra at 30, 70 100 eV collision energies 106

Figure 5.4 – Thymine (upper figure) and uracil (lower figure) partial cross sections (in arbitrary units) 111
Figure 5.5 - The line drawn with circles (o) represents the ion yield as a function of the electron energy of $[T-H]^-$ upon DEA to the NB embedded in He droplets at 0.37 K. The solid line (—) shows the anion efficiency curves of $[T-H]^-$ while the dashed line (----) represents the sum of all other observed product anions, upon DEA to the corresponding bare nucleobase molecules. (Adapted from [73]) 113
Figure 5.6 - Computed real parts of the A′ and A′′ resonance energies as a function of ring-breaking deformations in uracil. The left panel deals with the C_3-N_5 stretch while the right panel is for the C_4-N_2 stretch [69]. 114
Figure 6.1- Schematic representation of a) 5-chlorouracil and b) 5-fluorouracil. 122
Figure 6.2 - 5-chlorouracil TOF anion mass spectra at three collision energies 127
Figure 6.3 - 5-fluorouracil TOF anion mass spectra at three collision energies 129
Figure 6.4 - 5-chlorouracil (upper figure) and 5-fluorouracil (lower figure) partial cross sections 137

Tables

Table 3.1 - Deflecting plates extraction voltage as a function of the potassium beam energy 36
Table 3.2 - SIMION results 42
Table 3.3 - NO_2^- peak characteristics at different acceleration voltages 64
Table 3.4 - Mass Calibration Iterations 66
Table 3.5 - HP 214B Specifications 70
Table 3.6 - FastComtec P7888 Specifications 71
Table 3.7 - Extraction delays 76
Table 4.1 - Experimental acquisitions parameters 84
Table 4.2 - Nitromethane negative ions assignment and respective relative partial cross sections at several collision energies 87
Table 5.1 - CM framework collision energy conversion 99
Table 5.2 - Experimental acquisition parameters used to measure Thymine 100
Table 5.3 - Experimental acquisition parameters used to measure Uracil 100
Table 5.4 - Thymine negative ions assignment and related relative partial cross sections at several collision energies 105
Table 5.5 - Uracil negative ions assignment and respective relative partial cross sections at several collision energies 107
Table 5.6 - Comparative tables on the DEA and electron transfer to thymine (left) uracil(right). 108
Table 6.1 - CM framework collision energy conversion 124
Table 6.2 - Experimental acquisition parameters used to measure 5-chlolouracil 124
Table 6.3 - Experimental acquisition parameters used to measure 5-fluorouracil 125
Table 6.4 - 5-chlorouracil negative ions assignment and relative partial cross sections at several collision energies 128
Table 6.5 - 5-fluorouracil negative ions assignment and respective relative partial cross sections at several collision energies 130
Table 6.6 - Anionic species formed following electron attachment and electron transfer to 5-chlorouracil (left) 5-fluorouracil (right). 131

Acronyms and symbols

1-MeT	1-methil-thymine
3-MeU	3-methil-uracil
5-ClU	5-Chlorouracil
5-FU	5-Fluorouracil
5-BrU	5-Bromouracil
a_a	Acceleration in the extraction region
a_b	Acceleration in the acceleration region
a.m.u	Atomic mass units
a.u.	Arbitrary units
α	Spatial orientation coordinate
b	Impact parameter
CAD	Computer aided design
CE	Charge Exchange
CM	Centre of Mass
d	Acceleration region length
D	Drift region length
DBS	Dipole-bound state
DC	Direct current
DEA	Dissociative electron attachment
DFT	Density functional theory
DNA	Deoxyribonucleic acid
DSB	Double strand Breaks
$\Delta_{cov/ion}$	Energy difference between the covalent and ionic surfaces
$\Delta_f H_g^o$	Enthalpy of formation
E_{CM}	Energy in the centre of mass framework
$EA(r)$	Molecular electron affinity
ε	Electronic Hamiltonian eigenvalue
E	Energy
ε^0	Internal motion Hamiltonian eigenvalue
e^-	Single electron
E_{effec}	Effective energy
E_b	Electric field between first grid and the second grid
E_a	Electric field between repeller plate and the first grid
E_{Lab}	Energy in the laboratory framework

$E_1;E_2$	Adiabatic potential curves
EA	Electron affinity
$EA_{adiabatic}$	Adiabatic electron affinity
EA_v	Vertical electron affinity
$E_{Threshold}$	Threshold energy
ETS	Electron Transmission Spectroscopy
$f(\alpha)$	Angular function of the molecular spatial orientation
F	Force
FWHM	Full-Width Half-Maximum
H_{el}	Electronic Hamiltonian
H	Hamiltonian
h	Planck constant
$\hbar$	Reduced Planck constant
H^0	Hamiltonian for the internal motion
$H_{11};H_{22}$	Diabatic potential curves (diagonal coupling matrix elements)
$H_{12};H_{21}$	Diabatic coupling terms (non-diagonal coupling matrix elements)
$I_{Measured}$	Measured electrical current
I_{REL}	Relative electrical current
$I_{Displayed}$	Displayed electrical current
IE	Ionisation energy
K^0_{Hyper}	Hyperthermal potassium atom
K^+_{Hyper}	Hyperthermal potassium ion
K^+	Potassium cation
K^0_{Ther}	Thermal potassium atom
k	Electronic state
K	Potassium
K^0	Neutral potassium
LEE	Low energy electrons
LUMO	Lowest unoccupied molecular orbital
M^0_{Hyper}	Hyperthermal Alkali atom
M^+_{Hyper}	Hyperthermal alkali ion
$M_{Kinetic}$	Mass resolution associated with initial kinetic distribution of the ions
$M_{Spatial}$	Mass resolution associated with initial spatial distribution of the ions
m_p	Projectile mass
m_t	Target mass

M^0_{Ther}	Thermal alkali atom
M^+_{Ther}	Thermal alkali ion
M_{Total}	Total mass resolution
m	Mass
m/z	Mass to charge ratio
MO	Molecular orbital
μ	Dipolar moment
NB	Nucleobase
ν	Frequency
P	Inelastic scattering probability
p	Landau-Zener probability
PES	Potential energy surface
PID	Proportional integral derivative
Pt100	Platinum resistance thermometers
$\phi(q;R)$	Adiabatic electronic wavefunctions
$\phi(q;R_0);\phi(q)$	Diabatic electronic wavefunctions
π^*	π antibonding orbital
Ψ	Total wave function
q	Electronic coordinates
Q	Total cross section
q	Electrical charge
R_{c1}	First crossing radius
R_{c2}	Second crossing radius
R	Nuclear coordinates
R_c	Crossing radius
RET	Rydberg Electron Transfer
RNA	Ribonucleic acid
R_o	Fixed internuclear distance
r	Vibrational coordinate of the diatomic molecule
s	Covered length in the extraction region
S	Extraction region length
SSB	Single strand breaks
σ^*	σ antibonding orbital
t_b	Time spent in the acceleration region
t_a	Time spent in the extraction region
t_{TOF}	Total time of flight

T_n	Kinetic energy operator
t_D	Drift region flight time
t_b	Acceleration region flight time
t_D	Drift region flight time
t_a	Extraction region flight time
T	Thymine
t_{col}	Collision time
TNI	Temporary negative ion
TOF	Time of Flight
t_{vib}	Vibration period
U_0	Initial kinetic energy
U_b	Kinetic energy acquired in the acceleration region
U_a	Kinetic energy acquired in the extraction region
U	Total kinetic energy
$U_i(r)$	Undistorted Morse potential of the free X_2^- molecular ion
$U_c(r)$	Morse potential of the free X_2 molecule
U	Uracil
$V_c(R)$	Isotropic Lennard-Jones potential for the $M + X_2$ interaction on the covalent surface
V_{k^+}	Potassium cations acceleration voltage
$V_i(R,\alpha)$	Anisotropic potential describing the $M^+ + X_2^-$ interaction
v_0	Ions initial velocity
v_b	Ions velocity as they enter the acceleration zone
v_D	Ions velocity as they enter the drift region
V_{cov}	Covalent potential curve
$V(q;R)$	Interaction potential
V_{ion}	Ionic potential curve
v_r	Radial velocity
v	Velocity
$V_{\mathrm{cov}}(R,r)$	Covalent potential surface
$V_{ion}(R,r,\alpha)$	Ionic potential surface
V_b	Acceleration region voltage

V_{einzel}	Einzel lens voltage
V_a	Extraction region voltage
$V_{Def.Plates}$	Deflecting plates voltage
VFR	Vibrational Feshbach Resonance
$x_0; s_0$	Ion initial position
x_b	Starting point of acceleration region
x_D	Starting point of the drift zone
$\chi(R)$	Nuclear wavefunctions
XU	Generic halouracil

Chapter 1 Introduction

1.1 Radiation effects on biological systems

Over the last years, the international scientific community has taken a special interest in better understanding the various processes capable of damaging and mutating living cells, especially when these might be directly related to the development of severe physiological disorders. Indeed, it is quite well established that ionising radiation (X-rays, γ-rays, ions, protons and electrons) is capable of, within the early stages of irradiation (~10^{-16} s after interaction), triggering mechanisms that, in the long term eventually result in cellular damage. The effects (direct and indirect) of such radiation have been acknowledged as one of the most significant mechanisms when dealing with structural and functional deviations at the cellular level. These deviations can result in cellular mutations, impairment and eventually lead to the development of oncological pathologies.

Owing to its high capability of DNA damage, ionising radiation is also currently used in radio therapeutic treatments as a mean of destroying cancer cells but, as effective as it may be, it is also responsible for destroying and damaging the surrounding healthy cells. In order to increase the effectiveness of such radio therapeutic processes, the interactions of ionising radiation with the physiological constituents should be described not only by the macroscopic evidences of structural impairment (in terms of energy deposition), but more importantly, it must be understood in terms of the fundamental molecular mechanisms that precede cellular damage.

Figure 1.1 represents the different stages of DNA damage by ionising radiation along with their correspondent time scales. Starting with the initial moment of cellular irradiation (10^{-16} s), physical processes govern, proceeding to physical-chemical processes and so forth, up to the stage where biological processes may occur, the field of medical and health sciences. As challenging as it may be to understand the processes within the latter stages of the diagram interaction stage, it is also essential to understand and eventually gain some control over the nascent physical and physical-chemical processes. Such knowledge, to be understood at the molecular level, can provide suitable information for the development of additional detection and suppressing methods of physiological disorders rising from ionising radiation. Additionally, it may also become possible to provide more effective treatments to the related medical conditions.

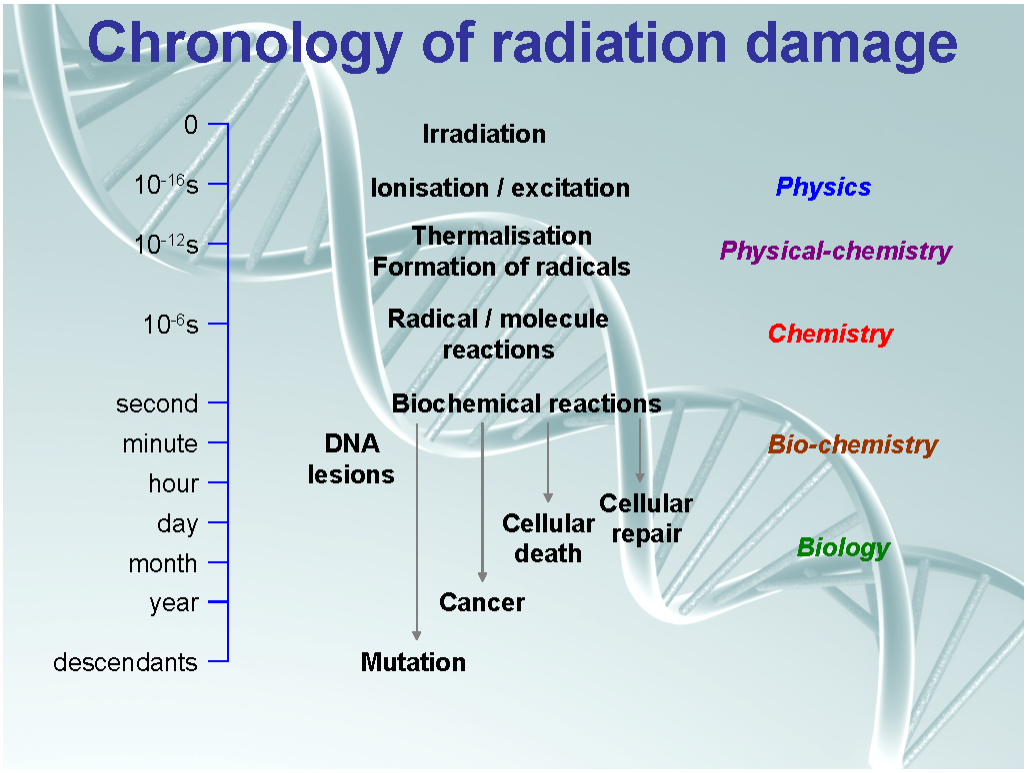

Figure 1.1 - Chronological diagram of radiation induced damage

Over the last century, a significant amount of research efforts were conducted in order to understand the effects (direct and indirect) of high-energy radiation interaction with biological systems, especially with DNA and living cellular tissue. The majority of biological effects carried out by high energy radiation is not associated with direct interactions with the biological material, but are instead related to secondary species created upon direct irradiation [1]. Such secondary species (free electrons, radicals, ionic species) can be more reactive and potentially more damaging than the primary radiation responsible for their formation. As these secondary species may interact with the surrounding medium, favourable conditions are in order for genotoxic, mutagenic and other potentially lethal DNA degradation (DNA and desoxiribose structural damage, DNA basis liberation, single and double strand breaks, among many others [1-5]).

One of the most abundant secondary species created upon irradiation are secondary electrons. In fact, for each MeV of energy deposited in the biological tissue, ~ 5×10^4 secondary electrons are produced with kinetic energies below ~20 eV [6]. Before being fully thermalized by the physiological medium, these low energy electrons (LEE) can be responsible for DNA damaging by direct or indirect interaction. Electron-induced direct DNA damage occurs when LEE become directly attached to the molecules within the DNA strands, causing molecular instability that eventually leads to DNA rupture. On the other hand, indirect DNA damage is caused by secondary LEE's that interact with other

molecules within the physiological medium, producing high quantities of radicals, cations and anions, which can in turn induce further damage.

1.2 Direct and indirect DNA damage

As mentioned above, the majority of DNA damages are induced by secondary species that are created upon the interaction of ionising radiation with the biological material. However, until recently, damage to DNA was thought to be due to the direct interaction of high energy radiation (α, β, γ or x-rays) only. However, in a landmark research publication the group of Sanche and co-workers have experimentally shown that, upon low energy electron beam irradiation (3 to 20 eV) of thin films of plasmid DNA, the number of single strand breaks (SSB), double strand breaks (DSB) and loss of supercoiled helicity (phosphate–ester bond breakdown) showed a resonant-like behaviour [6]. The results have also shown that electron induced DNA damage with energies far below the ionisation energies of its molecular constituents [1], can actually happen at energies as low as 3 eV, followed by a relatively intense structure (resonance) at 10 eV. This behaviour is significantly different from the photon induced DNA damage results, showing an energy threshold around 7 eV followed by a linear increase until it reaches 12 eV. Beyond that, the amount of damage stabilizes for increasing energies during the next hundreds of eVs [6]. Furthermore, when comparing the damage efficiency of a single photon against damage efficiency of single low energy electron, it is possible to realize that 30 photons are necessary to operate a DNA strand break or helicity loss whereas only 4 secondary electrons are needed to achieve the same damage level.

It was also shown that secondary electrons are more efficient in terms of operating DNA damage, with respect to direct radiation related damage. Adding all this to the fact that secondary electrons are one of the most abundant secondary species created upon irradiation, it became rather evident that low energy electrons may play an important role when as far as radiation related DNA damage is concerned. In fact, both Boudaiffa *et al.* [6] and Lennert *et al.* [7] suggest that 70% of the DNA damage is associated to secondary low energy electrons and that only 30% of the damages are related to direct deposition of energy.

In the course of successive inelastic collisions within the medium these electrons are thermalized and become solvated within 10^{-12} s. The relevance of reactions of *presolvated* (nonthermal) electrons with the nucleotides has already been pointed out more than two decades ago by Aldrich *et al.* [8]. They anticipated from time resolved ps-pulse radiolysis experiments the significant importance of fast processes for reactive mechanisms in biological relevant molecules (such as amino acids), i.e. reactions induced by electrons prior to solvation.

Following Sanche´s work, several theoretical and experimental studies concerning dissociative electron attachment processes have been performed, especially on biological relevant molecules (DNA basis, RNA basis, sugars, among many other).

Electron attachment processes can be described as the interaction of a single electron (e^-) and a generic molecule (AB), as follows:

$$e^- + AB \rightarrow (AB^-)^* \rightarrow (AB)^- + h\nu \quad (1.1)$$

$$\rightarrow AB^* + e^- \quad (1.2)$$

$$\rightarrow A + B^- \; or \; A^- + B \quad (1.3)$$

In these reactions, the free electron is captured by the molecule leading to the formation of excited temporary negative ion (TNI), in a so-called metastable state (or quasi-stable state). These electrons are attached to the molecule for a short time period (of the order of 10^{-16} s) through a resonant attachment process, which can only occur for electrons of appropriate energy [9]. This can be seen as the accommodation of the extra electron to one of the normally unoccupied molecular orbitals (MOs), which depending on the electron affinity (positive or negative) of the target molecule can either be a lowest unoccupied molecular orbital (LUMO) or a higher lying virtual MO [9].

After the TNI is created, several reaction paths can follow. In one of them, the molecule is capable of accommodating the "extra" electron but the excess of internal energy causes a photon to be emitted (equation (1.1)). This process is known as radiative stabilization and it is characterized by reaction times between 10^{-8} and 10^{-9}s.

Another reaction channel is characterised by the auto-detachment of an electron from the TNI, as in equation (1.2). In this reaction, the molecule AB suffers no dissociation and becomes neutral once again, but it can remain in a vibrational excited state. The interaction time of such reactions depends greatly on the size of the molecule, but normally of the order of 10^{-12} to 10^{-14} s.

Finally, in equation (1.3), is presented the dissociative electron attachment, which at the molecular level is believed to be responsible for most of the damage on biological structures (direct DNA damage). In this process, the TNI dissociates due to the instability created by the "extra" electron, which not only changes the intramolecular potential but also adds an excess of internal energy that ultimately results in the TNI dissociation. The presence of such process greatly depends not only on the energy of the incoming electron (resonant process) but also it can be site and bond selective, i.e. this process can selectively occur depending if the electron is captured into certain regions of the molecule and, if so, it can selectively induce molecular dissociation of specific chemical bonds [10].

On the other hand, rather than attaching directly to DNA subunits, the secondary electrons may interact with other molecules within the surrounding environment and, by means of DEA, give rise to free radicals which may be extremely reactive species. Free radicals are by definition atoms,

molecules or ions with unpaired electrons on an open shell configuration that may have positive, negative, or zero charge. If allowed to diffuse, they can be potentially quite damaging to other molecules. Considering that 70% of the cells are composed of H_2O, water radiolysis can also play an important role in the formation of free radicals. In this case, however, their formation is not accomplished by dissociative electron attachment processes, but instead by means of radiation induced ionisation of water molecules (equation (1.4)), that will further react with neutral H_2O molecules and eventually lead to $OH^{\bullet}$ radical formation (equation (1.5)).

$$H_2O + h\nu \rightarrow H_2O^+ + e^- \tag{1.4}$$

$$H_2O^+ + H_2O \rightarrow H_3O^+ + OH^{\bullet} \tag{1.5}$$

1.3 Electron transfer processes

Since the discovery of the capability of secondary electrons to cause SSB's and DSB's in DNA, a significant interest in the study of the various DNA constituents in the gas-phase has raised considerable interest in the international research community. Extensive studies on DEA have already been performed to the molecular constituents of the DNA, namely to the isolated DNA bases or sub-units. However, free electron attachment processes may be not sufficiently enough to completely describe the molecular reactions within the physiological medium. In this environment, "free" electrons have very limited lifetimes, i.e. through inelastic scattering electrons will quickly lose energy to the medium and eventually react with or be solvated by the surrounding molecules. As such, these collisions are defined not only by the free electrons and the "target" molecules but also by the molecules in the surrounding medium, especially the molecules from which the electrons were initially ejected. In this context, studies on electronic capture of 'bound' electrons (as in atom-molecule collisions) may present a good alternative to better simulate the molecular damage processes induced by secondary electrons at cellular level.

In atom-molecule collisions, a neutral atom (A) possessing a weakly bound electron acts as an electron "donor". When the collision with a molecule (BC) occurs, an electron may be ejected from the source atom A to the "target" molecule BC. After that, several reaction channels may occur, as presented below:

$$A + BC \rightarrow A^+ + BC^- \quad \text{(Non Dissociative Ionisation)} \tag{1.6}$$

$$A + BC \rightarrow A^+ + B^- + C \quad \text{(Dissociative ionisation)} \tag{1.7}$$

$$A + BC \rightarrow A^+ + (B + C) + e^- \quad \text{(Dissociative ionisation)} \tag{1.8}$$

$$A + BC \rightarrow AB^+ + C + e^- \quad \text{(Dissociative ionisation)} \tag{1.9}$$

$$A + BC \rightarrow AB + C^+ + e^- \quad \text{(Dissociative ionisation)} \tag{1.10}$$

$$A + BC \rightarrow AB^+ + C^- \quad \text{(Reactive chemical ionisation)} \tag{1.11}$$

$$A + BC \rightarrow ABC^+ + e^- \quad \text{(Associative chemical ionisation)} \tag{1.12}$$

$$A + BC \rightarrow A + B^+ + C^- \quad \text{(Polar dissociation)} \tag{1.13}$$

The electron transfer processes, may also be pictured in two separate stages. First it is necessary for the neutral atom (A) to undergo ionisation in the surroundings of the "target" molecule (BC). The ejected electron must then be captured by the molecular target (BC), leading to the formation a TNI.

This process greatly depends on two key physical properties. One is the ionisation energy (IE) of the electron "donor" atom (A) and the other is the electron affinity (EA) of the "target" molecule (BC). EA is defined as the amount of energy needed for the electron to detach from the negative ion to the neutral and is designated as $EA_{adiabatic}$ when referring to adiabatic electron affinity or by EA_v when referring to vertical electron affinity. Another important physical property as far as atom-molecule collisions are concerned is the endoergicity of the process, shown in equation (1.14). If the ionisation energy is higher that the electron affinity, the endoergicity is positive, meaning that the process is endothermic.

$$\Delta E = IE(A) - EA(BC) \tag{1.14}$$

Following electron transfer processes in atom-molecule collisions, it is possible for certain amounts of excessive internal energy to be transferred back to the positive species A^+. This is in contrast to electron-molecule systems where such release of internal energy (to a third body) is not possible, at least within a time frame capable of competing with autodetachment and dissociation processes. In comparison to free electron attachment, atom-molecule collisions can induce the formation of stable parent ions (BC^-), change the probability for certain reaction channels or even induce the formation of additional fragmentation channels. Nevertheless, the set of results presented in this thesis suggest that the basic interactions of secondary radiolytic species, such as nonthermal free electrons, may in general disrupt the natural chemistry of DNA. Thus, a detailed knowledge of resonant electron induced damage to most of the chemical species found in cells will be required before a complete understanding of the nascent effects of ionising radiation on living tissue can be achieved.

In this thesis, studies are presented on electron transfer processes of 'bound' electrons to biological relevant molecules. In order to study such processes we have developed and improved a

crossed beam experimental setup (Chapter 3) to investigate negative ion formation induced by charge transfer processes between neutral potassium atoms (K) and isolated biomolecules.

Neutral potassium atoms are used as electron “donors” due to their low ionisation energies (IE(K) = 4.34 eV). Even though neutral potassium does not exist in the physiological environment, it could provide some insight on the role of charge “carriers” in the degradation of DNA molecules caused by low energy secondary electrons. Being so, and following the use of nitromethane as calibration molecule, studies of negative ion formation on DNA basis (thymine), RNA basis (uracil) and halouracils (5-chlorouracil and 5-fluorouracil) were performed. A comprehensive comparison was also established between DEA results and the results presented within this thesis.

Both 5-chlorouracil (5-ClU) and 5-fluorouracil (5-FU) have long been proposed as radiosensitiers due to their ability to easily dissociate in the presence of radiation yielding large cross sections for halogen anion formation. Due to the similarity between the chemical structure of halouracils and DNA basis, it is possible to operate the replacement of a DNA basis for an halouracil without producing changes in the genetic sequence or expression before irradiation [11]. By adding these halouracils in the DNA structure, it can be possible to greatly enhance the radiation induced dissociation yield of DNA. When administrated to tumoral cells, radiosensitizers can enhance the effectiveness of radio therapeutic treatments. As a consequence, lower radiation doses could be used in order to reduce the damage to healthy cells, which is usually a problem in this type of cancer treatments. The experiments on negative ion formation, in atom-molecule collisions, of both DNA basis and halouracils may provide some additional insight on whether the radiosensitisers are, comparatively to DNA basis, more capable of inducing DNA damage.

Chapter 2

Collision Theory and Ion Pair Formation

In this chapter a general formulation of the collision problem applied to the atom-atom collision will be presented, followed by the ion-pair formation probability given by the Landau-Zener formula. The problem arising from collision involving more complex systems will also be discussed followed by an introductory and conceptual presentation of a few models used to simplify the problem, namely for atom-diatomic collisions.

2.1 Two-Particle Collision

The most common way to describe the forces involved in the interaction of two atoms is to make use of the Born-Oppenheimer approximation. In this approximation it is assumed that the electronic and nuclear motion can be separated because of the large mass difference and subsequent large difference in velocity between the electrons and the nuclei. Because of this large velocity difference the nuclei motion is considered to have no influence on the electronic motion. The interactions between atoms are therefore determined by potentials that are dependent on the energy of the electronic states, which in turn are parametrically dictated by the internuclear distance of the two atoms. As a result the electronic states define the forces applied on the nucleus and not the other way around [12].

2.1.1 Born-Oppenheimer approximation: Adiabatic Framework

The interaction between two particles can be described in quantum mechanics by the Schrödinger equation

$$H\Psi = E\Psi \,, \tag{2.1}$$

which can be alternatively [13] expressed as

$$\big[H - E\big]\Psi = 0 \tag{2.2}$$

The Hamiltonian H can be written as

$$H = T_n(R) + H_{el}(q;R) \ , \tag{2.3}$$

in which the nuclear coordinates are described by R and the electronic coordinates by q. The term $T_n(R)$ is the kinetic energy operator that describes the motion of the nuclei and $H_{el}(q,R)$ is the electronic Hamiltonian, which contains electronic kinetic energy operator and the nuclear Coulomb interactions that depends parametrically on the nuclear coordinates (in this formulation the spin-orbit coupling is ignored).

The first step of the Born-Oppenheimer approximation consists in separating the nuclear motion from the electronic motion. Towards that end, the total wavefunction $\Psi(q;R)$ is expanded in a complete, orthogonal set of adiabatic electronic wavefunctions $\phi(q;R)$ that depend parametrically on the nuclear coordinates R. In other words the nuclear motion is considered to be slow, allowing the electrons to adjust their positions for each new internuclear distance. The total wavefunction can now be written as

$$\Psi(q;R) = \sum_k \phi_k(q;R)\chi_k(R) \ , \tag{2.4}$$

in which $\chi_k(R)$ is the nuclear wave function associated with each electronic state k.

Replacing equations (2.4) and (2.3) in (2.2) we obtain

$$\sum_k [T_n + H_{el} - E]\phi_k(q;R)\chi_k(R) = 0 \tag{2.5}$$

which can be shown as follows

$$\sum_k \left[\underbrace{[T_n]\phi_k(q;R)\chi_k(R)}_{(1)} + \underbrace{[H_{el}]\phi_k(q;R)\chi_k(R)}_{(2)} - E\phi_k(q;R)\chi_k(R) \right] = 0 \ . \tag{2.6}$$

In the first term of equation (2.6), the adiabatic electronic wave functions are derived assuming that $\phi_k(q;R)$ are slowly varying functions of R, meaning that the terms like $\frac{\partial \phi_k(q;R)}{\partial R}$ can be neglected. Therefore it is possible to write:

$$[T_n]\phi_k(q;R)\chi_k(R) = \phi_k(q;R).[T_n]\chi_k(R) \tag{2.7}$$

Regarding the second term of equation (2.6), if we consider that the differentiation terms within the electronic Hamiltonian $[H_{el}]$ are operated only with respect to the electronic coordinates q, is possible to write

$$[H_{el}]\phi_k(q;R)\chi_k(R) = \chi_k(R).[H_{el}]\phi_k(q;R) \ , \tag{2.8}$$

where $\phi_k(q;R)$ are the eigentstates (known as adiabatic states [14]) of the electronic Hamiltonian given by

$$[H_{el}]\phi_k(q;R) = \varepsilon_k(R)\phi_k(q;R) \, , \tag{2.9}$$

meaning that equation (2.8) can be expressed as

$$[H_{el}]\phi_k(q;R)\chi_k(R) = \varepsilon_k(R)\phi_k(q;R)\chi_k(R) \tag{2.10}$$

If equation (2.7) and (2.10) are replaced in equation (2.6) we obtain

$$\sum_k \left[\phi_k(q;R).[T_n] + \varepsilon_k(R)\phi_k(q;R) - E\phi_k(q;R) \right]\chi_k(R) = 0 \tag{2.11}$$

By multiplying the above equation from the left by each of the basis functions $\phi_i(q;R)$ and integrating over q [13], we obtain:

$$\sum_k \left[\left\langle \phi_i(q;R) \right| [T_n] + \varepsilon_k(R) - E \left| \phi_k(q;R) \right\rangle \right]\chi_k(R) = 0 \ , \tag{2.12}$$

which from the orthogonality of the basis becomes

$$\left[[T_n] + \varepsilon_i(R) - E \right]\chi_i(R) = 0 \ . \tag{2.13}$$

Equation (2.13) represents the Born-Oppenheimer set of coupled equations (in an adiabatic framework), where each electronic eigenvalue $\varepsilon_i(R)$ will give rise to a full internuclear potential energy surface (known as *Born-Oppenheimer* surface), that is parametrically dependent on the internuclear distance.

However, these surfaces can (and often do) become coupled by the so called non-adiabatic effects, contained in the terms that have been neglected in approximation in equation (2.7), meaning that the Born-Oppenheimer approximation is violated. For example, when a transition between two adiabatic states of the same symmetry occurs (knowing that the respective potential surfaces cannot cross each other [14]), the Born-Oppenheimer principle is not fulfilled. In this case the complete Hamiltonian is no longer diagonal in the electronic basis $\phi_k(q;R)$, meaning that the adiabatic electronic states k are coupled by the terms involving the nuclear kinetic energy operator neglected above. This corresponds to the fact that if two adiabatic states of equal symmetry come together, the non-crossing rule forces the respective wave functions to significantly change their character. If, however, two particles come across each other along one of these states with high velocity, the time spent in the avoided crossing region could be too short for the electrons to adjust their positions. This means that the system violates the non-crossing rule and moves along a so-called diabatic potential curve [14].

2.1.2 Born-Oppenheimer approximation: Diabatic Framework

The major difference between the diabatic and adiabatic approach of the collision problem is that, in the diabatic framework, the total wavefunction $\Psi(q;R)$ is expanded in a complete, orthogonal set of diabatic electronic wavefunctions $\phi(q;R_0)$ that no longer depend on the nuclear coordinates R and are determined for a fixed internuclear distance R_0 (normally at infinite separation). In other words, the collision partners' motion is considered to be so fast that the electronic states will keep the same character independently of the nuclear distance R.

In the diabatic framework the Hamiltonian H should be written as

$$H = T_n(R) + \underbrace{V(q;R) + H^0(q)}_{H_{el}} , \tag{2.14}$$

where $T_n(R)$ is the kinetic energy operator that describes the motion of the nuclei and where the electronic Hamiltonian $H_{el}(q,R)$ has been divided in two parts, the interaction potential $V(q;R)$ and the Hamiltonian for the internal motion $H_0(q)$.

The total wavefunction can be written as

$$\Psi(q;R) = \sum_k \phi_k(q)\chi_k(R), \tag{2.15}$$

in which nuclear coordinates are described by R and the electronic coordinates by q and $\chi_k(R)$ is the nuclear wavefunction associated with each diabatic electronic state k.The orthonormal set of electronic wavefunctions $\phi_k(q)$ are the eigenstates of $H^0(q)$ that is given by

$$[H^0(q)]\phi_k(q) = \varepsilon_k^0\phi_k(q) \ . \tag{2.16}$$

If equations (2.15) and (2.14) are replaced in the Schrödinger's equation (2.2), we get

$$\sum_k [T_n(R) + V(q;R) + H^0(q) - E]\phi_k(q)\chi_k(R) = 0 \ , \tag{2.17}$$

which from equation (2.16) can be written as

$$\sum_k [T_n(R) + V(q;R) + \varepsilon_k^0 - E]\phi_k(q)\chi_k(R) = 0 \tag{2.18}$$

Contrarily to the approximation needed in the adiabatic framework, in this case the nuclear kinetic energy operator when operated on the electronic wavefunction will be null, since $\phi_k(q)$ does not depend on the nuclear coordinate R.

By multiplying the left terms of equation (2.18) each of the basis functions $\phi_i(q)$ and integrating over q [13], it is possible to obtain:

$$\sum_k \Big[\big\langle \phi_i(q)\big|[T_n](R) + \varepsilon_k^0 - E\big|\phi_k(q)\big\rangle + \big\langle \phi_i(q)\big|V(q;R)\big|\phi_k(q)\big\rangle\Big]\chi_k(R) = 0 \tag{2.19}$$

which from orthogonality of the basis becomes

$$\Big[[T_n(R)] + V_{ii}(R) + \varepsilon_i^0 - E\Big]\chi_i(R) + \sum_{i\neq k} V_{ik}(R)\chi_k(R) = 0 \ , \tag{2.20}$$

with $V_{ik} = \big\langle \phi_i(q)\big|V(q;R)\big|\phi_k(q)\big\rangle$

In this case the electronic Hamiltonian (in the matricial form) is non-diagonal in the diabatic electronic basis ϕ , as follows

$$[H_{el}(R)]\phi = \begin{pmatrix} V_{11}(R) + \varepsilon_1^0 & \cdots & V_{1k}(R) \\ \vdots & \ddots & \vdots \\ V_{i1}(R) & \cdots & V_{ik}(R) + \varepsilon_i^0 \end{pmatrix} \phi \tag{2.21}$$

where diagonal elements $(i = k)$ represent the diabatic potentials, which are coupled by the off-diagonal elements $(i \neq k)$ of the interacting potential $V_{ik}(R)$.

In the diabatic framework an atom-atom collision between an alkali atom (A) and a halogen atom (B) can be described within the two states approximation, where the collision is defined by inelastic processes where only two diabatic states are relevant. The covalent wavefunction ϕ_1 is associated with the electronic state (A+B) and an ionic wavefunction ϕ_2 is associated with the electronic state (A^++B^-). In this case the electronic Hamiltonian of the electronic diabatic wavefunctions ϕ_1 and ϕ_2 is given by

$$[H_{el}(R)]\phi = \begin{pmatrix} V_{11}(R) + \varepsilon_1^0 & V_{12}(R) \\ V_{21}(R) & V_{22}(R) + \varepsilon_2^0 \end{pmatrix} \phi = \begin{pmatrix} H_{11} & H_{12} \\ H_{21} & H_{22} \end{pmatrix} \phi \tag{2.22}$$

where $\begin{pmatrix} H_{11} & H_{12} \\ H_{21} & H_{22} \end{pmatrix}$ is the coupling matrix between the ionic and covalent states and, as mentioned above, the diagonal terms H_{11} and H_{22} describe the diabatic potential curves that are coupled by the terms H_{12} and H_{21}. These coupling terms can be considered equivalent ($H_{12} = H_{21}$) if magnetic interactions (introducing quadrupolar, octapolar, … terms) are neglected [14].

From the diagonalization of this coupling matrix, the adiabatic states can be easily found:

$$E_{1,2} = \frac{1}{2}\left(H_{11} + H_{22} \pm \sqrt{\left(H_{22} - H_{11}\right)^2 + 4H_{12}^2} \right). \tag{2.23}$$

From the previous equation is possible to conclude that when H_{12} is very small in respect to $H_{22} - H_{11}$ (i.e. away from the crossing point R_c) the adiabatic and diabatic states will show a similar behaviour (as observed in Figure 2.1). On the other hand, in the vicinity of R_c where $H_{11}(R_c) = H_{22}(R_c)$, these states show a different behaviour, as the diabatic cross and the adiabatic do not. At this internuclear distance the energy gap between the adiabatic states is given by $2H_{12}(R_c)$. Moreover, for these adiabatic states to cross ($E_1(R_c) = E_2(R_c)$), the coupling term must equal to zero

$(H_{12}(R_c) = 0)$ which, from the non-crossing rule, could only happen if the two wavefunctions that describe these adiabatic states show different symmetry and multiplicity.

The analysis of the curve crossing schematically presented in Figure 2.1 can be very useful when trying to understand the atom-atom collision process (ion-pair formation) from the charge transfer (electron jump) point of view.

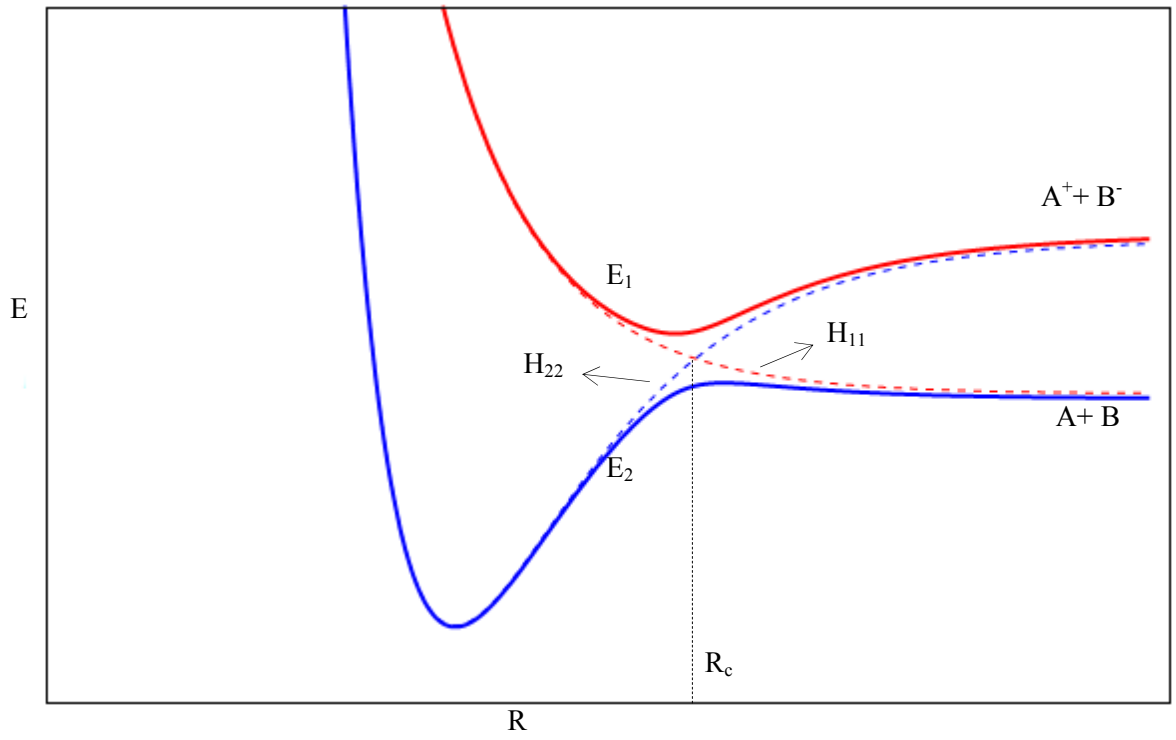

Figure 2.1 – Schematics of the potential energy curves: adiabatic states E_1 and E_2 - full curves; diabatic states H_{11} (covalent) and H_{22} (ionic) - dashed curves, where R_c designates the crossing radius

Considering that two atoms on the covalent state $(A + B)$ are approaching each other and reach the crossing point, one of two processes can occur. If the crossing is passed adiabatically the electronic wavefunctions will present a dramatic change in their character, meaning that an electron jump has occurred leading to ion-pair formation $(A^+ + B^-)$. If, however on the other hand, the crossing is passed diabatically, the electronic wavefunctions will maintain their character and no electron jump will occur, which leaves the collision partners in the same covalent state as before, i.e. $(A + B)$.

After the first crossing and as the atoms come close together, they start to move apart, eventually reaching the crossing point again. If this second crossing is reached from the covalent state $(A + B)$, the cross can once again be passed diabatically leading to $(A + B)$ where no electron jump

has occurred, or it can be passed adiabatically leading $\left(A^+ + B^-\right)$ where an electron jump took place. If the second crossing arises from the ionic state $\left(A^+ + B^-\right)$, the cross can be passed diabatically leaving the atoms in the same ionic state $\left(A^+ + B^-\right)$, or it can be passed adiabatically where reneutralization occurs leading to the covalent state $\left(A + B\right)$.

From the analysis performed above is possible to conclude that, after the collision, the atoms are left in the ionic state (ion-pair formation) if the crossings are passed first diabatically and then adiabatically or vice-versa (often called non-adiabatic transitions).

2.1.3 **Landau-Zener model**

The Landau-Zener formula was obtained by solving the time-dependent Schrödinger equation for a simple one dimensional, two state system where it was assumed that colliding particles follow a given classical trajectory [12]. This model assumes a single collision coordinate described by the internuclear distance $R(t)$, a constant and equivalent collision radial velocity $\left(v_r = \frac{\partial R(t)}{\partial t}\right)$ for both electronic states around the crossing point R_c (straight trajectory) [15].

The time-dependent Schrödinger equation was solved within the diabatic framework and from it the probability *p* was derived, defining the probability for the two-particle system to stay in the diabatic potential energy curve (i.e. the probability of passing R_c diabatically) [14]. As such, the Landau-Zener formula for the diabatic transition probability is then given by:

$$p = \exp\left(-\frac{2\pi H_{12}^2(R_c)}{\hbar v_r \left|\frac{d}{dR}\left(H_{11} - H_{22}\right)\right|_{R=R_c}}\right) \tag{2.24}$$

where v_r defines the collision radial velocity and where H_{12}, H_{11} and H_{22} are taken from the diabatic coupling matrix in equation (2.22) described in the previous section.

The classical trajectory approximation used in the Landau-Zener derivation is more accurate for high velocity collisions where a straight line trajectory can be considered. These straight line collision trajectories are described by the impact parameter method (illustrated in Figure 2.2), where the system moves along a trajectory given by:

$$R = \sqrt{b^2 + (vt)^2} \tag{2.25}$$

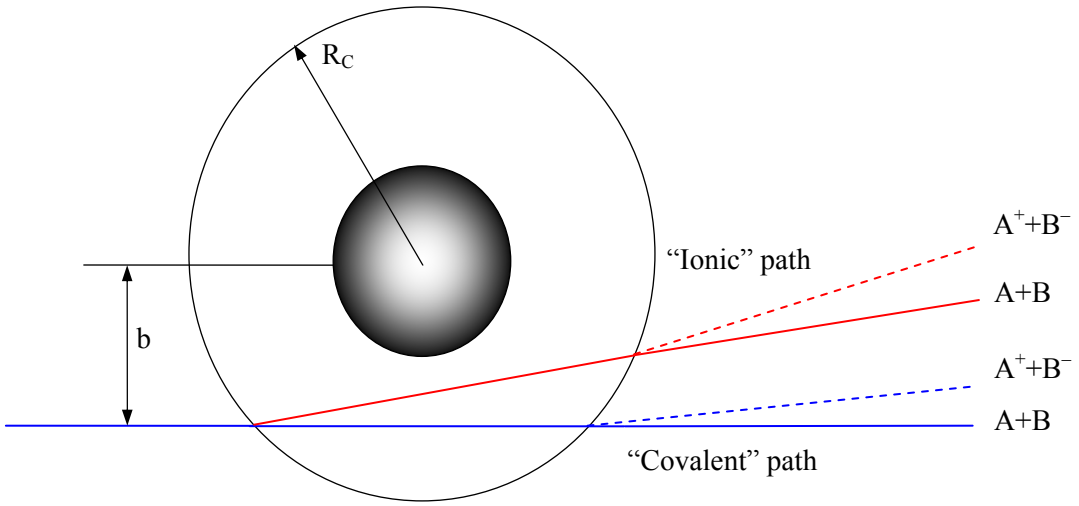

Figure 2.2 - Simplified representation of the high velocity collision trajectories involving an alkali atom (A) and an halogen atom (B). The impact parameter b is given by $R_C/\sqrt{2}$

When the electron jump occurs at the first crossing, the scattering happens along the "ionic" path (red line). If no electron jump occurs at the first crossing, the scattering happens along the "covalent" path (blue line). It is important to note that both ionic (dashed lines) and covalent states (full lines) can result from the so-called "covalent" or "ionic" paths.

Considering that the outcome of the two particle collision is described within the impact parameter model through four different trajectories (if $b < R_c$) , it is possible to realize that two of them give rise to ionic states (inelastic scattering) and the other two are responsible for covalent states (elastic scattering). Being so, it is possible to express the probability of ion-pair formation using equation (2.24), as follows

$$P_{inelastic\ scattering} = p(1-p) + (1-p)p = 2p(1-p) \tag{2.26}$$

where p(1-p) represents the probability for passing the first crossing diabatically and the second adiabatically. The term (1-p)p represents the other case, where the first crossing is passed adiabatically and the second diabatically.

2.1.4 Atom-Atom Collisions

As reported before, when two neutral atoms collide in their ground state, two separate processes can occur. One of them is identified as elastic scattering, meaning that after the collision the atoms are left in the covalent state where both species are kept neutral and where the total kinetic energy of the system is conserved. The other process is inelastic scattering, where the atoms undergo a charge exchange mechanism and after the collision are left in an ionic state, where no conservation of total kinetic energy of the system is observed. As such, these inelastic scattering processes are extremely relevant to the analysis of the negative ion formation through electron transfer processes (the topic of this thesis).

To characterise the electron transfer processes in atom-atom collisions we will consider the following alkali-atom iodine-atom collision

$$Na + I \rightarrow Na^{+} + I^{-} \tag{2.27}$$

The relevant diabatic covalent ($Na + I$) and ionic ($Na^{+} + I^{-}$) states are described by the potential energy curves shown in Figure 2.3. Considering that both states are of the $^{2}\sum^{+}$ type and have the same symmetry, the corresponding adiabatic potential curves will show an avoided crossing point at R_c [12].

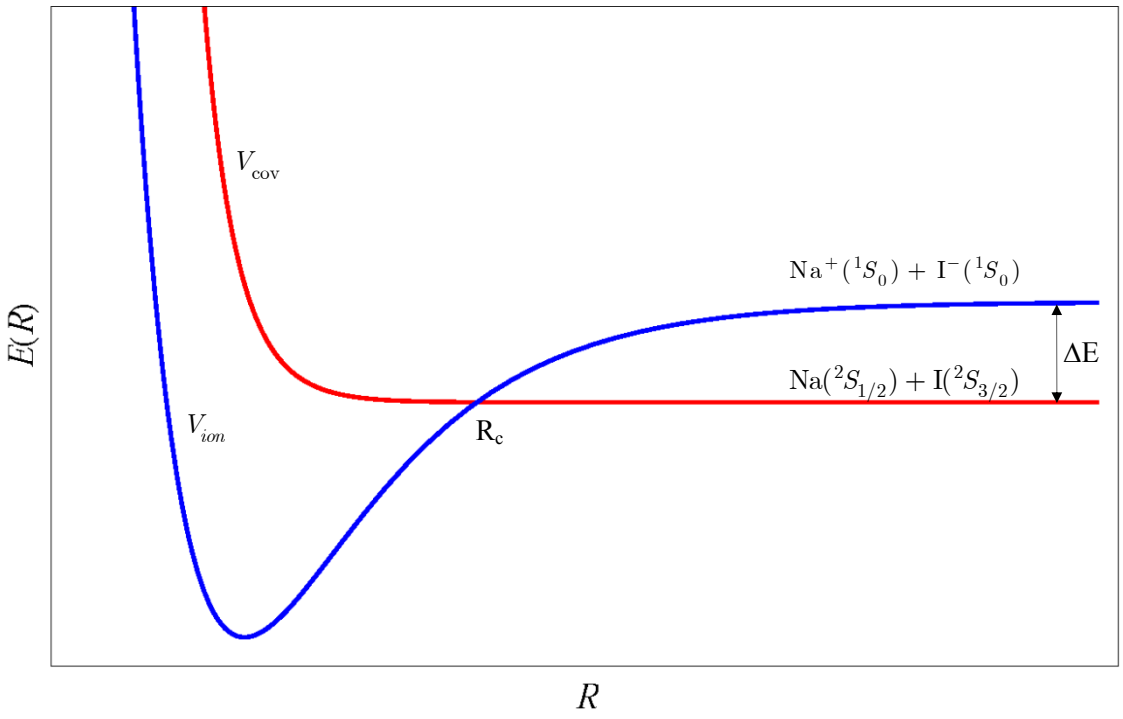

Figure 2.3 - Approximated diabatic potential energy curves for the lowest diabatic sates of $Na - I$. V_{cov} and V_{ion} are the diabatic potentials corresponding to the covalent and ionic electron configuration respectively. ΔE is the difference between the ionization potential Na and the electron affinity of I [12].

The separation between the diabatic potentials V_{cov} and V_{ion} at infinite $Na-I$ internuclear distance is given by

$$\Delta E = IE - EA \ , \tag{2.28}$$

where IE is the ionisation energy of the alkali atom, $\mathrm{Na}(5.14\,eV)$, and EA is the electron affinity of the halogen, $\mathrm{I}(3.06\,eV)$ [12]. Considering that the crossing point R_c occurs at large internuclear distances, is possible to neglect the Van der Waals and induction forces, which means that the covalent potential can be considered zero and that the ionic potential can be given by a Coulombic potential. Though, the crossing point is given by

$$R_c = \frac{14.41}{\Delta E} \tag{2.29}$$

where R_c is expressed in Å and ΔE in eV.

When R_c is reached, transitions between two diabatic states can occur (i.e. the crossing point is passed adiabatically) if the relative kinetic energy is larger than ΔE. In other words, the electron can jump from the alkali atom to the halogen atom if there is sufficient kinetic energy between the atoms for the system to go from the covalent to the ionic state. However, if the impact parameter $b < R_c$ (see Figure 2.2) the crossing point will be passed twice and electron transfer is possible on either crossings, yielding four different trajectories.

For ion-pair formation, the electron jump should merely occur at the first or at the second crossing, which will only happen within two trajectories (inelastic scattering). If the electron jump occurs at both crossings or if does not occurs at all (within the same trajectory), no ion-pair formation will happen (elastic scattering).

To evaluate the ion-pair formation probability, the Landau-Zener formula (2.24), presented in section 2.1.3 , was used. If V_{ion} is assumed to be given by a Coulomb potential and V_{cov} through a constant, the Landau-Zener formula can be simplified to

$$p = \exp\left(-\frac{2\pi H_{12}^2(R_c)R_c}{v_r(b;R_c)}\right) \tag{2.30}$$

where all units are defined in atomic units. The coupling element H_{12} is evaluated at R_c and the radial velocity v_r is given by

$$v_r = v\left(1-\frac{b^2}{R_c^2}\right)^{\frac{1}{2}} \ , \tag{2.31}$$

where b is the parameter impact and v is the relative velocity between atoms.

After being calculated for various alkali-halide systems the coupling element H_{12} can be approximated by the semi-empirical relation of Olson *et.al.* [16]

$$H_{12} = \frac{cR_c \times \exp\left(-0.86\, cR_c\right)}{d} \tag{2.32}$$

where $c = \frac{\left(\sqrt{2IE} + \sqrt{2EA}\right)}{2}$ and $d = \sqrt{2IE}\sqrt{2EA}$, all in atomic units. From this equation it is possible to note that the coupling element H_{12} depends exponentially on the crossing point R_c. This fact illustrates the extreme importance of the value R_c in the Landau-Zener transition probability p.

Given that R_c can be calculated using equation (2.29), is possible to estimate the transition probability *P* by replacing equation (2.32) and (2.31) in equation (2.30). The transition probability *P* can then be used to evaluate the total probability for ion-pair formation given by

$$P(b) = 2p(1 - p)\,, \tag{2.33}$$

Finally, the total cross section for ion-pair formation can be estimated by integrating equation (2.33) for any given value of *b* from 0 to R_c, as given in equation (2.34).

$$Q = 2\pi \int_0^{R_c} P(b) b\, db \tag{2.34}$$

2.2 Atom-Molecule Collisions

In comparison with collisions involving two ground state atoms, the collisions between one atom and one molecule (also in their ground state) are associated with an increased number of processes (i.e. elastic scattering, rotational excitation, vibrational excitation, collision induced dissociation, electronic excitation and combinations of these processes). Atom-molecule collisions can no longer be described by making use of one-dimentional potential curves but by a multi-dimensional potential hypersurfaces instead. In addition, when going from atom-atom to atom-molecule collisions, new characteristic time scales have to be considered. For instance, in atom-atom collisions the collision time should be compared with the time of rotation of an electron in its Bohr orbit. In atom-molecule collisions, however, two additional characteristic times have to be considered, the rotational and vibrational times associated with the molecule. The first is normally long when compared with the collision time thus being normally considered to be frozen. The second, however, is in the same order of magnitude of the collision time, meaning that vibrational effects have to be considered in the collision process [17].

Several approaches have been developed to describe electronically inelastic atom-molecule collisions (i.e. non-adiabatic processes in molecular collisions.) [17]. In the following sections a brief description of some will be given. In the classical approach the nuclear motion of the nuclei is described using classic mechanics (interference effects are neglected) and the transition probabilities are calculated using quantum mechanical methods.

2.2.1 Atom Rigid-Molecule Collisions

The simplest way to deal with atom-molecule collisions is to consider the molecule as a single atom. This approach is made assuming that during the collision (i.e. between crossings) molecular rotation and vibration do not exist. In other words, the molecule is considered to be rigid or “frozen” during the collision process. This approximation is valid if the atom-molecule potential is isotropic and if the electronic properties of the molecule are independent of internal degrees of freedom, especially its electron affinity. Normally this is not the case, but if the collision time (t_{col}) is made sufficiently short with respect to the vibration period (t_{vib}) of the molecule, this approximation could be useful to characterize some atom-molecule collision within the high velocity region ($t_{col} \ll t_{vib}$) [12] [15].

For collisions between alkali atoms and halogen molecules (atom-diatom collision) the total cross section for ion pair-formation in the high velocity region can be evaluated using the Landau-Zener formulation presented before. The only difference to the atom-atom case is that the coupling

factor will also be dependent on the spatial orientation of the molecule when the first crossing point is reached. The coupling element will in this case be given by

$$H_{12}(\alpha) = H_{12}\ f(\alpha)\ , \tag{2.35}$$

where H_{12} is given by the reduced relation of Olson (see equation (2.32)) and $f(\alpha)$ is an angular function related to the spatial orientation of the molecule.

2.2.2 Frank-Condon Model

In the previous model, the internal degrees of freedom of the molecule have been completely neglected. In this model, however, the vibrational degrees of freedom are accounted, but the molecule is considered to be rigid during the collision. Assuming that the transition probabilities at the curve crossing are the same for all vibrational levels, the final vibrational distributions may be calculated by making use of a direct Frank-Condon overlap calculation. Moreover, if highly excited vibrational states or continuum states are involved in the calculations, it is possible to make use of the reflection approximation [18].

2.2.3 Surface hopping trajectory method

The methods discussed in sections 2.2.1 and 2.2.2 are usually applicable for collisions where $t_{col} < 0.1 < t_{vib}$, which is a condition normally not satisfied [17]. In fact, the internal degrees of freedom cannot be considered rigid for the majority of atom-molecule systems, especially the vibrational motion (as stated before), meaning that atom-molecule collision should be described in contrast to atom-atom collisions, by multi-dimensional potential hypersurfaces. Unfortunately, obtaining such hypersurfaces is an extensive and extremely complicated task, especially when dealing with atom-polyatomic collisions. In addition, the collision trajectories on such multidimensional surfaces are critically dependent on the characteristics of the hypersurfaces and, contrarily to the atom-atom collisions, the crossing region can be reached several times within the same trajectory. In other words, for a given single atom-molecule interaction, several crossing radius can exist.

In the surface hopping trajectory method the nuclear motion is described classically and only the transition probabilities are treated quantum mechanically. In addition, the molecular vibrations degrees of freedom are accounted but also from a classical point of view. This method requires, however, good potential energy surfaces to be obtained. To this end, and as presented in references [12, 17], a simplified empirical model for the determination of potential surfaces regarding collisions between alkali atoms and halogen molecules $M + X_2$ is shown below (this model may be of special interest when trying to understand the relevance of vibrational effects in the collision process).

The collision between an alkali atom and a halogen molecule can be described through the diabatic potentials given by:

$$V_{ion}(R,r,\alpha) = V_i(R,\alpha) + U_i(r) + \Delta_{\mathrm{cov}/ion} \tag{2.36}$$

$$V_{\mathrm{cov}}(R,r) = V_c(R) + U_c(r) \tag{2.37}$$

where R is the distance between the alkali atom and the centre of mass of the molecule, r defines the vibrational coordinate of the diatomic molecule and α denotes the spatial orientation coordinate. The $V_i(R,\alpha)$ is an R dependent anisotropic potential describing the $M^+ + X_2^-$ interaction, where the total charge of the negative ion is equally divided on the two atoms of the molecule. $U_i(r)$ is the undistorted Morse potential of the free X_2^- molecular ion and $\Delta_{cov/ion}$ is the anisotropic energy difference between the covalent and ionic surfaces. $V_c(R)$ an isotropic Lennard-Jones potential for the $M + X_2$ interaction on the covalent surface and $U_c(r)$ defines the Morse potential of the free X_2 molecule [12]. It is important to note that, considering the expressions for the covalent and ionic potentials defined by equations (2.36) and (2.37), the vibration of the molecule, given by r, is assumed to be decoupled from the relative motion between the alkali atom and the molecule (given by R). In other words, the

internuclear motion of the molecule or the molecular ion is assumed to be not influenced by the proximity of the projectile [12].

Contrarily to the atom-atom case where the crossing between surfaces is given by one particular point R_c, the crossing between these atom-diatom surfaces will be given by a seam (see example in Figure 2.4).

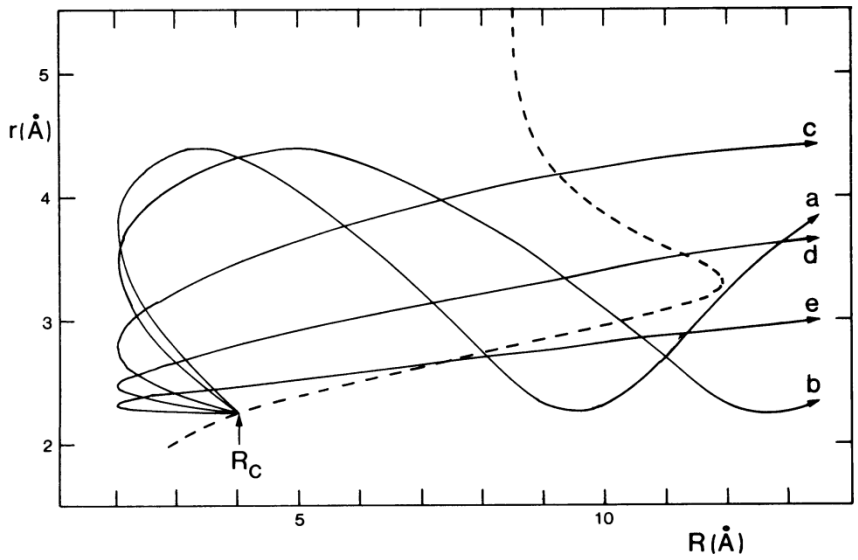

Figure 2.4 - Trajectories on the ionic surface for the $Na^+ + Br_2^-$ system at impact parameter b = 2 A, and collision velocities (a) 4×10^3 ms^{-1}, (b) 5×10^3 ms^{-1}, (c) 10^4 ms^{-1}, (d) 2×10^4 ms^{-1}, and (e) 4×10^4 ms^{-1}. The dashed line denotes the seam between the covalent and ionic surfaces. All trajectories are assumed to switch to the ionic surface at $R = R_c$ and at the equilibrium bond length, $r = r_e$, of the Br_2 molecule, but the probability of return to the covalent surface is a decreasing function of the coordinate R at the point at which the trajectory re-crosses the seam [19].

In the regions where the repulsive part of the potential $V_i(R,\alpha)$ could be neglected and the covalent state is approximately zero, the crossing seam can be given by

$$R_c(r) = \frac{14.4}{IE - EA(r)} \ . \tag{2.38}$$

Additionally, the coupling term $H_{12}(\alpha)$ between these two surfaces can be obtained as

$$H_{12}(\alpha) = H_{12} f(\alpha) \ , \tag{2.39}$$

where $f(\alpha)$ is an angular function related to the spatial orientation of the molecule and H_{12} is given by the reduce relation of Olson shown in equation (2.40).

$$H_{12} = \frac{cR_c \times \exp\left(-0.86c\ R_c\right)}{d} \tag{2.40}$$

where $c = \frac{\left(\sqrt{2IE} + \sqrt{2EA(r)}\right)}{2}$ and $d = \sqrt{2IE}\sqrt{2EA(r)}$. It is also important to note that in equation (2.40), the electron affinity is dependent on the internuclear distance of the halogen molecule *r*.

Now by making use of (2.38), (2.39) and (2.40) presented above, the Landau-Zener transition probability given in equation (2.30) can thus be estimated, as long as the EA(r) of the molecule is known (i.e. the *r* dependent potential energy curves of the neutral and the anionic states of the molecule). Moreover, since H_{12} depends exponentially on R_c, the Landau-Zener transition probability will be strongly dependent on *r* (through R_c and H_{12}), which will have dramatic effects on the collision process [17].

As such, if the transition between the neutral molecular and the anionic molecular states is assumed to be Franck-Condon transitions (i.e. the electron jump from the alkali atom to the molecule happens so fast that the internuclear distance of the molecule is kept the same) it should be possible to evaluate the influence of the molecular vibration in the collision process (in terms of electronic transition probabilities) through the analysis of the potential energy curves of both the neutral molecule and the anionic molecule.

As an example one can consider the generic collision between the alkali atom (A) and the halogen molecule (BB) given by (2.41), in which the neutral and a repulsive anionic molecular states can be represented as depicted in Figure 2.5.

$$A + (BB) \rightarrow A^{+} + (BB)^{-} \tag{2.41}$$

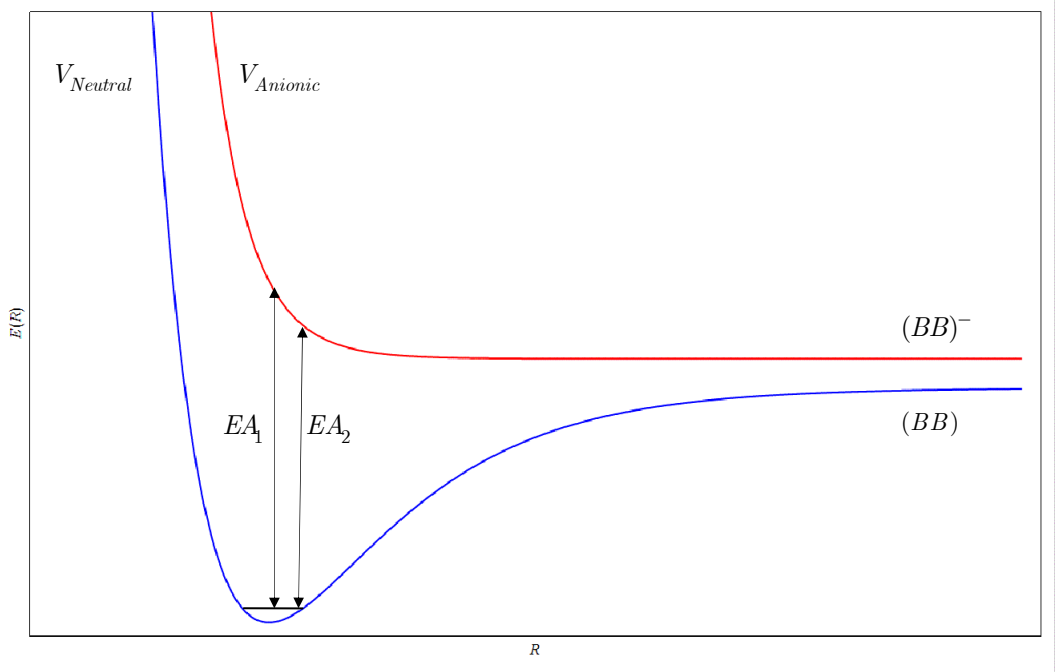

Figure 2.5 - Schematic neutral and anionic potential energy curves for a generic halogen molecule BB

From the picture above is possible to infer that in this collision there will be two different R_c values, one when the collision partners approach (determined by EA_1) and other when they are moving apart (determined by EA_2). This would happen especially for small collision velocities, where the molecule, upon suffering a transition from the neutral state to the repulsive region of the anionic potential, has enough time to show an extension in its internuclear distance. This behaviour is normally described as *bond stretching* and can be very relevant in the total ion-pair formation probability, mainly because of the exponential dependence of H_{12} with respect to R_c. In the case presented in Figure 2.5 this dependence will cause the coupling factor H_{12} to be much smaller for R_{c2} than for R_{c1}, which in turn will increase the probability for the molecule to stay in the anionic state, thereby favouring the formation of negative ions.

The ion-pair formation probability defined in equation (2.26) is based on the assumption that both crossings are passed in equivalent physical conditions, which in atom-atom collisions seems to be fairly true. However, when dealing with atom-molecule collisions this principle is no longer valid (as discussed above). The total cross section for ion-pair formation can then be calculated by integrating the Landau-Zener transition probability for all the relevant values of the impact parameter *b*. The total cross section is then given by

$$Q = 2\pi \int_0^{R_c} \left(p_2(1 - p_1) + (1 - p_3)p_1 \right) b db \tag{2.42}$$

where p_1 defines the diabatic Landau-Zener transition probability, p_2 is the transition probability at the second crossing when the first is passed adiabatically. Finally, p_3 represents the transition probability at the second crossing when the first is diabatic. The total cross section given by equation (2.42) can also be given according to [12, 20] as:

$$Q = 4\pi R_c^2 F\left(\frac{v}{\delta}\right) \tag{2.43}$$

where $\delta = 2\pi H_{12}^2 R_c^2$ and v is the relative velocity between the projectile and target.

The universal function $F\left(\frac{v}{\delta}\right)$ can be modified in order to incorporate the specific effects that describe the different collision cases mentioned before. As such, in Figure 2.6 is shown the reduced total cross section for atom-atom (F_1), atom-rigid-molecule (F_2) and atom-molecule collisions (F_3). The latter describes the limit case where a complete extension of the molecular bond length occurs between the first and second crossings.

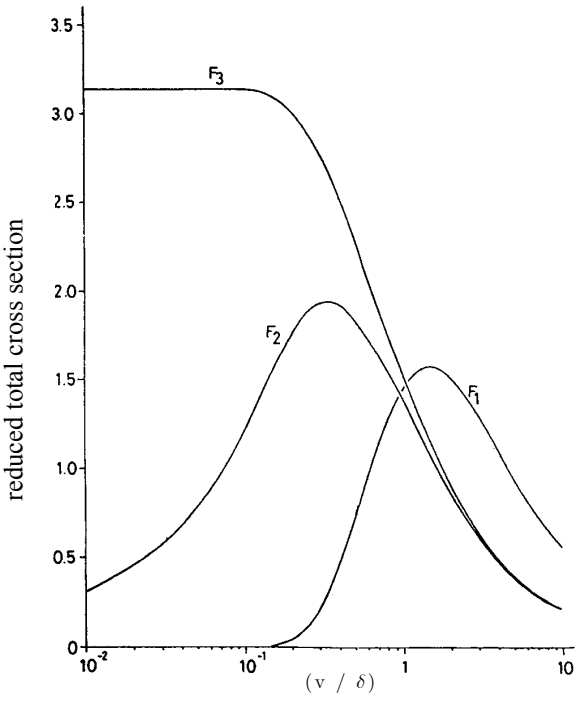

Figure 2.6 - Reduced total cross sections: F_1 defines the atom-atom interaction; F_2 defines the atom rigid-molecules interaction and F_3 defines the atom-molecule interaction considering the bond length extension. (adapted from [15])

It is also important to note that in collisions represented by F_3, when the lower collision velocity region is reached, the cross section should fall to zero. This is due to the threshold behaviour, resulting from the fact that a minimum collision energy will be needed for the electron jump to occur between the alkali atom and the target molecule. When the thresholds are experimentally determined it is possible to evaluate the adiabatic electron affinity of the anionic state, using the equation

$$EA_{adiabatic} = IE - E_{Threshold} \tag{2.44}$$

2.3 Final remarks

The aim of this chapter was to perform an introduction to the collision theory and the ion-pair formation in the context of atom-molecule collisions, starting with formulation and theory associated with the two-particle collision problem and from there evolving to atom-diatomic collisions. It was also pointed out how the molecular behaviour of the target in the atom-molecule collisions could be relevant to characterize the collisions, especially as far as ion-pair formation is concerned.

The collisions studied in this thesis are associated with negative ion formation resulting from the collision between neutral potassium atoms and molecules comprising six or more atoms. As such, it would be extremely difficult and time consuming to characterize the collision processes from the theoretical point of view or even to evaluate the total or partial cross sections. However, the concepts and notions introduced in this chapter can be particularly useful for the discussion of the experimental results.

Chapter 3 Experimental Setup

This chapter is devoted to the construction, characterisation and optimization of the experimental set-up developed to study electron transfer processes in collisions between neutral potassium atoms and biomolecules. It is important to note that the majority of the detection system was specifically constructed and implemented during the course of this thesis, especially the TOF mass spectrometer and all of the acquisition related sub-systems.

In the first sub-chapter a general introduction to the system components and operation are presented. The second and third sub-chapters comprise a detailed description of the components involved in the production of the projectile and target beams, respectively. The fourth sub-chapter is dedicated to the TOF mass spectrometer, where an introduction to basic TOF concepts plus the description and characterisation of the implemented mass spectrometer are addressed. The fifth sub-chapter comprises the characterization of the data acquisition system and its operation mode. In the sixth sub-chapter the vacuum system is presented.

3.1 Apparatus Overview

The experimental device is schematically shown in Figure 3.1 . The vacuum system comprises two chambers separately pumped through independent diffusion pumps, capable of reaching working pressures below 5×10^{-7} mbar. These two chambers are connected by a gate valve.

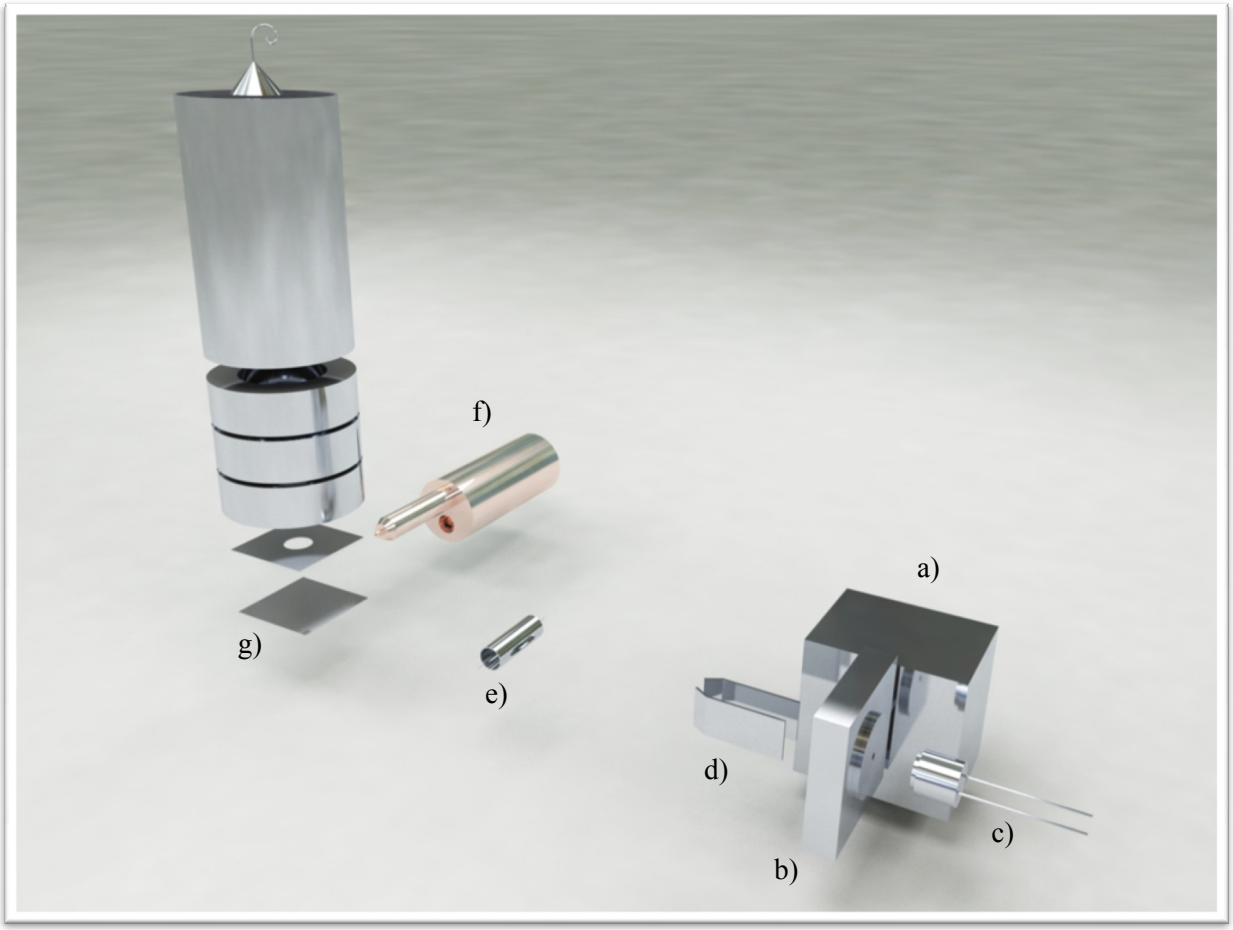

Figure 3.1 - Experimental schematics: a) Potassium oven; b) Charge exchange oven; c) Potassium ion source; d) Deflecting plates; e) Langmuir-Taylor detector; f) Bio oven; g) TOF mass spectrometer

In the potassium chamber a hyperthermal neutral potassium beam, which in the present thesis comprises kinetic energies between 20 and 100 eV, is produced by *resonant charge exchange*. This projectile beam is produced in a charge exchange source, which is essentially composed by a potassium oven, a charge exchange oven, a potassium ion source and a pair of deflecting plates (Figure 3.2)

The working principle of the charge exchange source is based on the collision between a hyperthermal alkali ion $\left(M^{+}_{Hyper}\right)$ and a thermal alkali atom $\left(M^{0}_{Ther}\right)$, resulting in an electron jump (or charge exchange) from the thermal alkali atom to the hyperthermal alkali ion. The hyperthermal alkali

ion becomes neutral and maintains its original kinetic energy, originating a hyperthermal alkali atom $\left(M^0_{Hyper}\right)$, as described in the reaction scheme below [21]:

$$M^+_{Hyper} + M^0_{Ther} \rightarrow M^0_{Hyper} + M^+_{Ther}$$

In this particular source (Figure 3.2), the alkali metal (in the case of this thesis potassium - K) is placed in the potassium oven, where it is heated and vaporized into the charge exchange oven. A potassium ion source is placed at ~2mm next to the entrance slit of the charge exchange oven, and a pair of deflecting plates are placed (~10mm) on the opposite side, at the exiting slit.

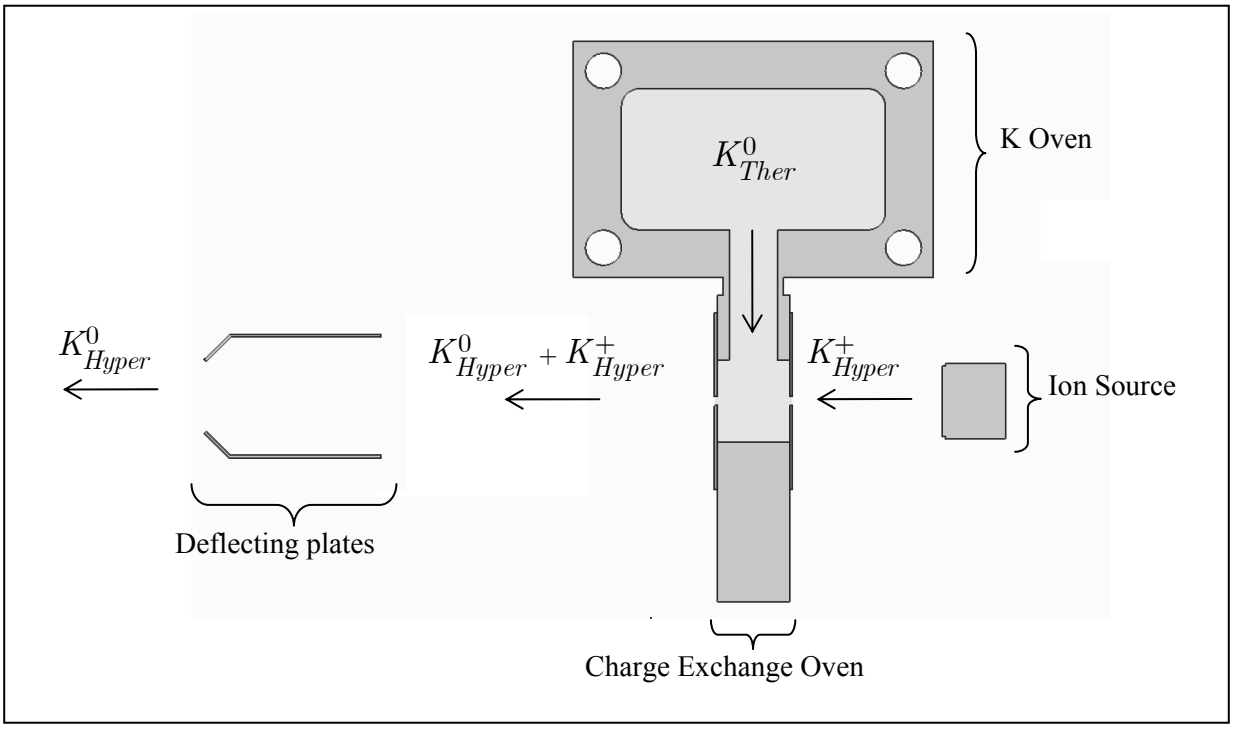

Figure 3.2 - Charge exchange schematics

An acceleration voltage is applied between the ion source and the charge exchange oven in order to push the potassium ions into the charge exchange oven, where the thermal potassium vapour lies. Some of the accelerated potassium ions, that enter the oven, undergo resonant charge exchange and become neutral. Due to the fact that not all of the potassium ions suffer charge exchange, a number of hyperthermal ions exit the charge exchange oven simultaneously with the hyperthermal neutrals. In order to remove as many ions as possible, an electric field is applied to the deflecting plates resulting mainly in a neutral fast beam.

Another important fact to note is that, while the charge exchange oven is filled with potassium vapour arriving from the potassium oven, some of it escapes through the entrance and exit slits. The thermal potassium atoms that leave through the entrance slit hit the ion source and are surface ionised,

but the thermal potassium atoms that escape through the exit slit contaminate the preferred hyperthermal potassium beam. However if this beam reaches the interaction collision region it will not contribute to the electron transfer process.

The resulting beam is composed mainly of hyperthermal potassium atoms that cross the inter-chamber valve and enter the collision chamber, with a kinetic energy defined by the acceleration voltage applied between the ion source and the charge exchange oven.

The alkali beam enters the collision chamber where is monitored by an iridium surface ionisation detector of the Langmuir–Taylor type. This detector samples the beam intensity but does not interfere with the beam passing to the collision region. It operates in a temperature regime that only allows detection of the fast beam. These ions are accelerated to the surrounding collector through an electric potential applied between the filament and the collector. The ionic current is thus measured in a electrometer.

Meanwhile, also in the collision chamber, an effusive target beam is produced either from a solid or a liquid sample. For that, we make use of a reservoir (named as biomolecules' oven) where liquid and solid samples are admitted.

The solid sample is placed directly inside the oven container where is heated and vaporized. Both the solid and liquid sample molecules escape the oven through a capillary tip (~1 mm diameter), producing an effusive beam that enters the collision region through a collimation slit. The biomolecules' oven and the related heating components are assembled on an insulation ceramic piece connected to a xy motion stage allowing the alignment of the target beam with the projectile beam.

The hyperthermal neutral potassium and the biomolecular beams cross in the collision region, located between the extraction plates. The negative ions formed after the collision are then extracted and time-of-flight mass analyzed.

3.2 Projectile Beam

The following picture (Figure 3.3) depicts the experimental arrangement for the production of the neutral potassium beam.

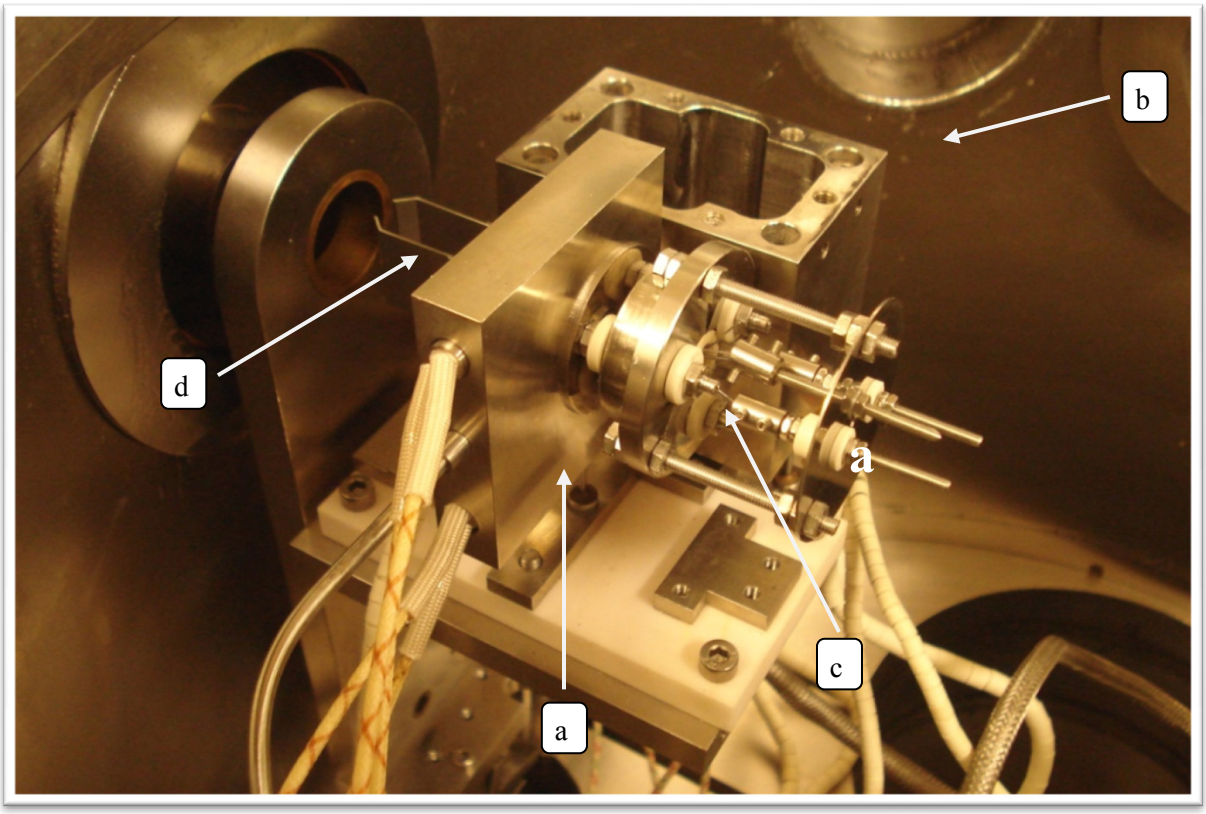

Figure 3.3 - Charge exchange source: a) Charge exchange oven; b) Potassium oven; c) K^+ Ion source; d) Deflecting plates

3.2.1 Potassium Oven/Charge Exchange Oven

The potassium oven and the charge exchange oven are stainless steel structures connected through a small cylinder. These structures are heated by two built-in 200 W cartridge heathers (Watlow firerod ref.0832K) each and measured by two PT100 resistors, individually fitted into the oven. The heating and temperature control of both ovens are run separately by PID units (Cal 3300 ref.331100000) computer controlled.

A solid piece of potassium to be heated on a stainless steel container is placed inside the oven by removing a top lid.

The charge exchange oven has front and rear 1.5 mm circular slits allowing to keep a reasonable high potassium vapour concentration inside it, much needed for the resonant charge exchange to occur.

To avoid alkali vapour condensation and possible blocking of the slits, the charge exchange oven is maintained at a temperature 20 ºC higher than the potassium oven. Therefore, during normal operation the potassium oven temperature is kept at 150 ºC, while the charge exchange oven at 170 ºC. In standby mode the temperatures are 60 ºC for the potassium oven and 90 ºC for charge exchange oven. By maintaining the oven at these standby temperatures it is easier and faster to shift into operation mode temperatures and achieve a stable and charge exchange suitable potassium vapour pressure.

3.2.2 Potassium Ion Source

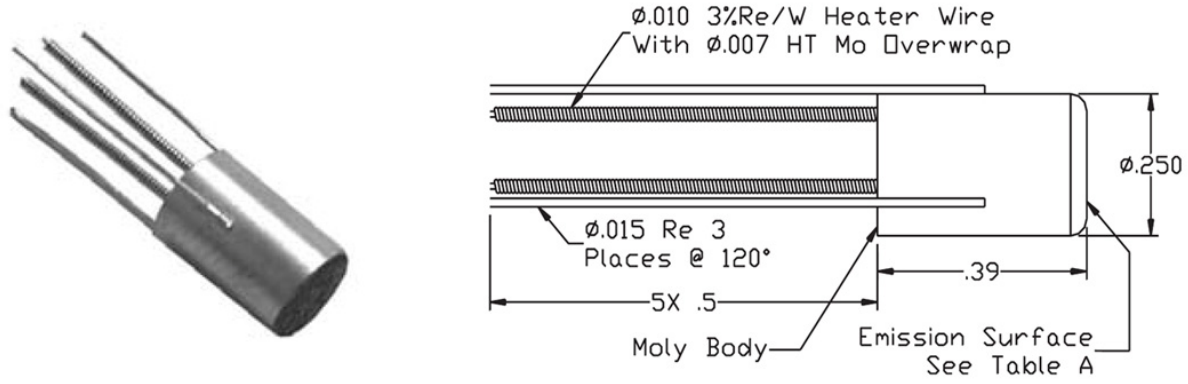

Figure 3.4 - K^+ Ion Source

The ion source was purchased from HeatWave Labs (model 101139) and is particularly suited to low energy experiments (below 100 eV) where ion beams with small energy spreads are essential. The potassium ion source (Figure 3.4) is composed by an indirectly heated, porous plug into which the emitter material has been fused. The molybdenum body holding the plug is machined with a solid partition for complete isolation between the emitter and the heater cavity. Three rhenium support struts are brazed at a 120 degree spacing yielding a mounting tripod. The heater is a non-inductively wound coil of molybdenum wire solidly potted into the body cavity with high purity Al_2O_3. The heater leads are overwrapped with molybdenum wire for major reliability. The emitter matrix is an extremely porous tungsten disc heliarc welded to the molybdenum heater body. The ion emitter material (K) is placed on the emitter face in controlled amounts and melted into the porous tungsten in a hydrogen atmosphere. The ion emitter material has the advantage that it does not react with the atmosphere. At high pulse voltages, the emitted ion current exhibits the Schottky effect, that is, increasing ion current with increasing extraction voltage. Mass analysis of beams from these ion emitters indicate that there are small amounts of impurities (alkali ions other than potassium) present when the emitter is heated

for the first time but the levels decrease rapidly within a few hours of operation leaving ion beams of very high purity. The impurity fraction of the ion beam decreases as the temperature of the ion emitter material increases. While the exact ratio of ions to neutral atoms emitted is not known, it appears that ions predominate by a very large factor. Negative ion and primary electron emission are not normally observed. Current densities of 1-10 mA/cm are achieved at operating temperatures between 950 ºC and 1100 ºC [22]. In order to achieve these working temperatures an electric current of approximately 2.05 A (BK Precision 1788 power supply) is provided to the heater. On the other hand, to accelerate the potassium ions a positive voltage in respect to ground is applied to the ion source´s body and is supplied by a DC power supply (Kingshill model 1500) or through a pulse generator (HP 214B pulse generator).

To assemble the ion source into the charge exchange oven a structure holder was developed. This structure should assure not only the alignment but also the required electric and temperature insulation. The holder was designed and machined at the Department of Physics' workshop facility (Universidade Nova de Lisboa), and is made out of a single stainless steel cylinder. The ion source was inserted in the centre of the holder and the electric feeds connected, through barrel connectors, to ceramic isolated M2 screws placed on a back plate. The ion source and the back plate (Figure 3.5) are assembled as a single piece to the charge exchange oven through insulating ceramic split bushes as observed in Figure 3.3. The external electric connections are made via the M2 screws avoiding the premature breakdown of the built-in ion source electric connections.

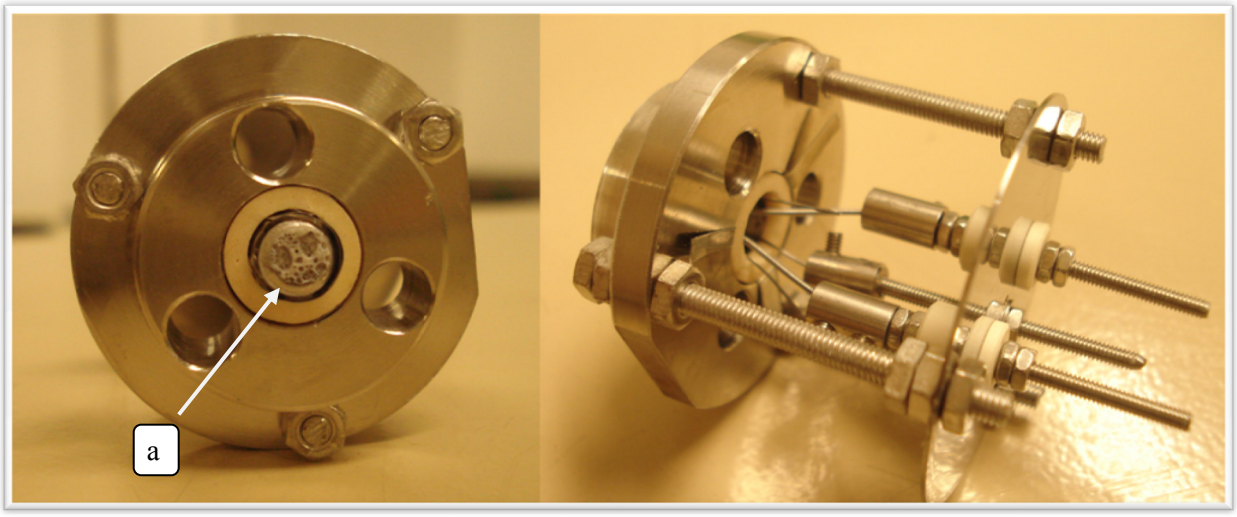

Figure 3.5 - Ion source support: a) Ion source

3.2.3 Deflecting Plates

The deflecting plates are composed of two parallel stainless steel plates (Figure 3.3d) placed after the charge exchange oven's exit slit. A repulsive positive voltage is applied (Delta Electronika E 300-0.1) to one of the plates and the deflected potassium ions are collected in the opposite plate. The resulting ionic current is measured by an electrometer (Keithley 6517A).

The electric potential, needed to maximize the ion extraction, shifts accordingly to the beam energy (Table 3.1). Therefore, a study was performed to retrieve the required potential values. For each beam energy, the deflection voltage was tuned until the highest collected current value was achieved.

Table 3.1 - Deflecting plates extraction voltage as a function of the potassium beam energy

Beam Energy (eV)	$V_{Def.Plates}$ (V)
20	40
30	50
40	65
50	80
60	100
70	100
80	125
90	125
100	125

3.2.4 Langmuir-Taylor Detector

This detector is essentially composed of a stainless steel cylindrical collector placed around a central high purity (>99%) 0.125 mm thick and 20 mm long iridium filament (Figure 3.6). Both collector and filament connectors are placed on a stainless steel plate and are electrically insulated through ceramic split bushes. The collector has two wide holes placed on opposing sides allowing the beam to pass through the detector while a small fraction of the potassium atoms are ionized.

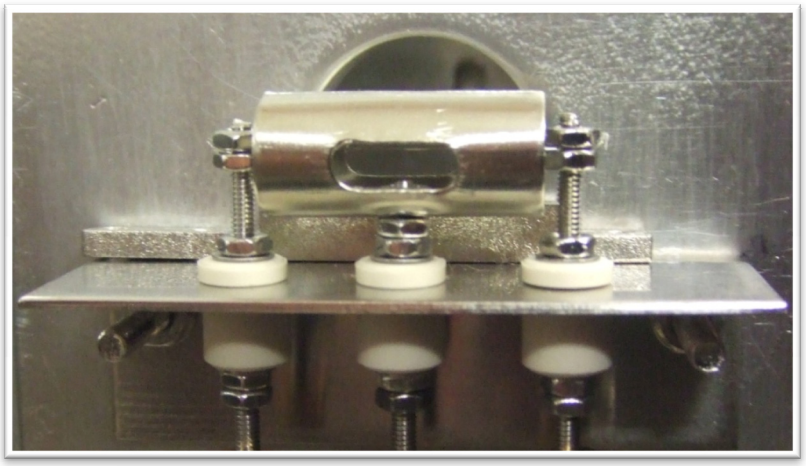

Figure 3.6 - Langmuir-Taylor detector

A typical current of 0.63 A is applied (Coutant LB-1000.2) to the iridium filament, which is enough to ionise the fast neutral potassium atoms. A positive potential of approximately +60 V is applied (Kingshill model 1500) to the filament to repel the potassium ions to the collector [21]. The resulting ionic current is measured by an electrometer (Keithley 6517A).

Since the hyperthermal neutral potassium beam reaching the detector has a small contribution of thermal potassium atoms, it is necessary to apply an experimental procedure to differentiate them. The method used involves turning off the ion source acceleration voltage, while making current measurements. Since no potassium ions will enter the charge exchange oven, the formation of the hyperthermal neutral beam will stop. Therefore, only the thermal potassium atoms emerging from the charge exchange oven can reach the detector. By pressing the REL button on the electrometer a new current referenced is set, based on the actual value of current being measured. The current displayed by the device is now defined as: $I_{Displayed} = I_{Measured} - I_{REL}$. Thus, when the ion source acceleration voltage is reactivated the electrical current displayed by the electrometer will concern only the hyperthermal potassium atoms.

It is also important to stress that the filament will only be able to ionise a small amount of atoms present in the potassium beam. Therefore, the number of ions that reach the collector is somehow proportional to the hyperthermal neutral potassium beam involved in the collision process.

3.2.5 K Collimation Slit

This collimation slit is a simple 47 × 30 × 1 mm stainless steel sheet with an aperture of 5 × 0.5 mm. It is mounted on the same structure that supports the TOF extraction system but is placed facing the charge exchange system.

3.2.6 Beam Characterization and Optimization

In order to characterise the potassium beam behaviour produced by the system, some studies were carried out. These studies indentified the system variables that are responsible for modifications on the beam properties. Parameters like the oven temperatures, the ion source temperature and the beam energy were investigated, bearing in mind not only the characterisation but also the intensity improvement of the hyperthermal neutral beam. Furthermore, the beam energy dispersion and the functional dependence between the applied acceleration voltage and the actual beam energy were also explored.

3.2.6.1 Ion Source Temperature

The ion source supplier guaranties a K^+ emission at operating temperatures between 900ºC and 1200ºC. The operating temperature of 1100ºC is achievable by supplying 2.05A to the source heater with a voltage drop of 7.20V, corresponding therefore to a resistance of about 3.5 Ω.

3.2.6.2 Potassium Oven Temperature

As mentioned before, the potassium atoms that are vaporized in the potassium oven play a fundamental role in the formation of the hyperthermal neutral potassium beam. In this study the oven temperature was progressively increased and K^0_{Hyper} monitored to better understand the efficiency of the charge exchange process as function of the temperature.

The plot presented below shows the evolution of the hyperthermal neutral beam with the potassium oven temperature. The results presented pertain to a beam of 70 eV, but similar behaviour was found in all the other beam energies investigated (20 eV < E < 300 eV).

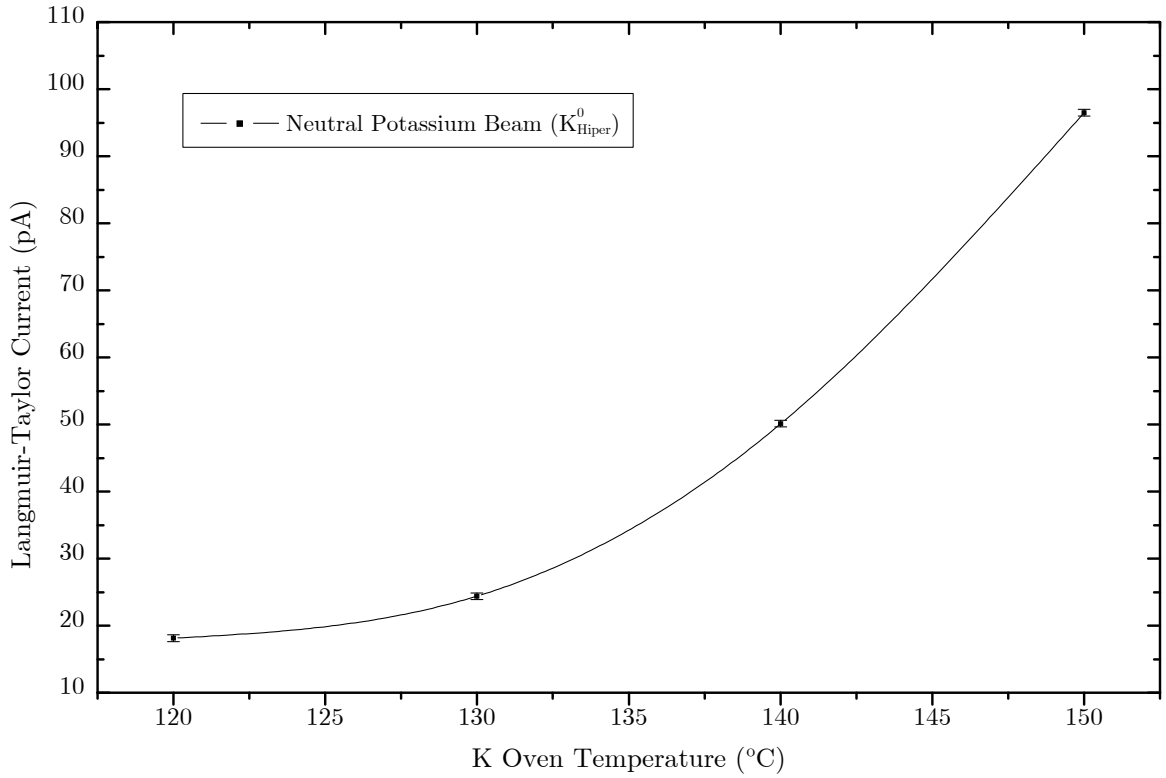

Figure 3.7 - Dependence of beam intensity as function of the potassium oven temperature

When the oven temperature is increased, the potassium vapour pressure in both potassium and charge exchange ovens will increase. This will make the charge exchange process more likely to happen, thus more positive ions can became neutral. Hence, as the temperature increases, the neutral beam is expected to increase (Figure 3.7) up to a limit where multiple collisions can happen leading to ionization processes, which in turn means decreasing the number of neutral species. The temperatures that simultaneously allowed a suitable continuous operation period (~1 month) and good beam intensity are 150ºC and 170ºC for the potassium and charge exchange oven, respectively.

3.2.6.3 Beam Energy

As shown in Figure 3.8 the beam intensity presents a direct dependence on the acceleration energy, following the Schottky behaviour (see chapter 3.2.2) which was also reported in other similar experimental set-ups [21]. Below 20 eV the neutral beam intensity becomes too weak, making it very difficult to be used as a projectile for electron transfer in collisions with a molecular target.

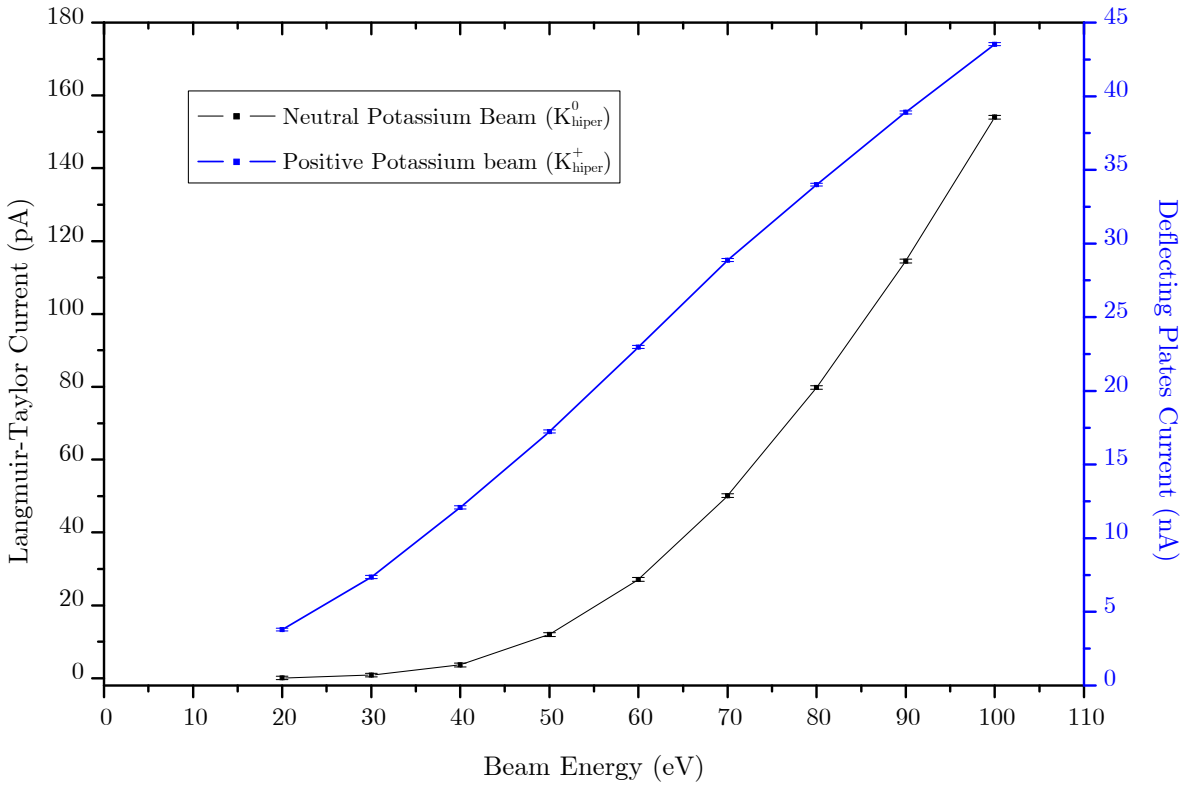

Figure 3.8 - Dependence of beam intensity with respective acceleration energy

3.2.6.4 Energy Spread and Functional Dependence

The energy spread can be defined as the full-width half-maximum (FWHM) value of the energy distribution and can be used to define the beam energy resolution ($\frac{E}{\Delta E}$).

The functional dependence, between the beam energy and the acceleration voltage applied to the ion source, is defined as the difference between the intended and the actual mean value of the beam energy distribution

In order to quantify both energy spread and functional dependence, SIMION^{TM} simulations were performed. The geometry used in this simulation was based on CAD technical drawing of the devices involved in the production and collimation of the neutral potassium beam (see Figure 3.9).

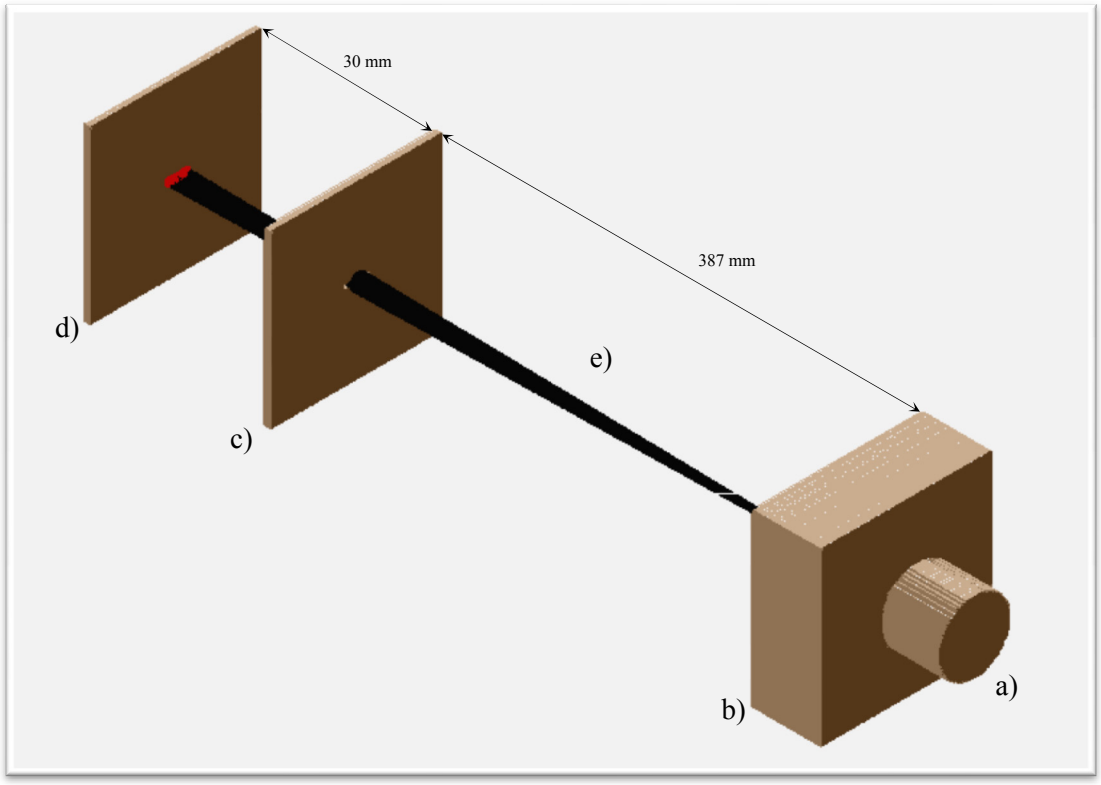

Figure 3.9 - SIMION simulation: a) Ion source; b) Charge exchange oven; c) Collimating slit; d) Collision plane; e) Potassium beam

In this simulation the ions were accelerated by applying a positive voltage between the ion source and the charge exchange oven. After passing through the charge exchange oven and the collimating slit, the ions reach the collision centre and their final energy is measured. Table 3.2 shows the simulation results as function of acceleration voltage energies:

Table 3.2 - SIMION results

Acceleration Voltage (V)	Effective Energy (eV)	Energy spread (eV)
10	8.897	0.001
30	26.691	0.002
50	44.485	0.003
70	62.279	0.004
100	88.970	0.006

From the results provided by the simulation it was possible to understand that both the beam mean energy and energy dispersion appear to have a linear dependence with the acceleration voltage, as follows

$$E_{effec} = 0{,}889\, V_k \tag{3.1}$$

and

$$\Delta E = (6{,}4 \times 10^{-5})\, V_k \tag{3.2}$$

where E_{effec} represents the beam effective energy, ΔE the energy spread and V_k the acceleration voltage.

3.3 Target Beam

In Figure 3.10 are shown the main components of the device responsible for the production of the biomolecular beam.

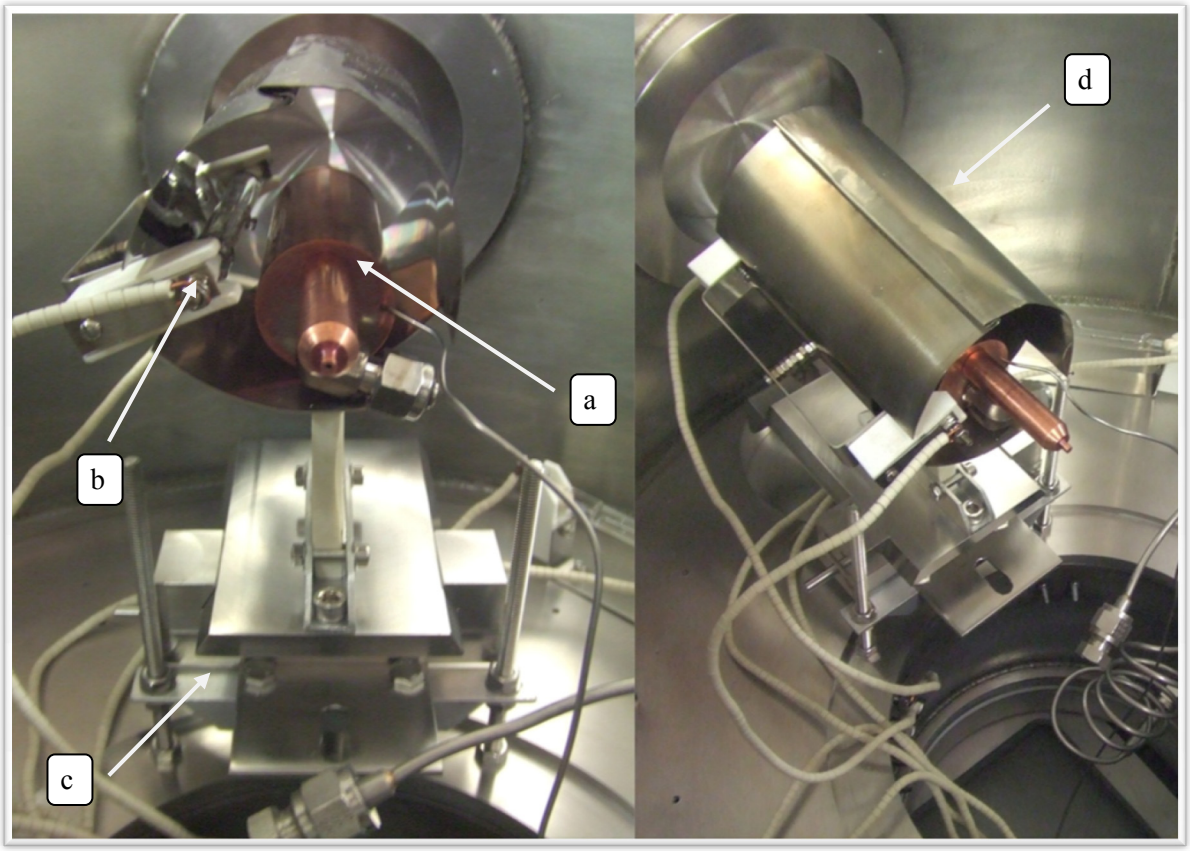

Figure 3.10 - Biomolecules' oven structure: a) Biomolecules' oven; b) Heating lamp; c) Platform; d) Radiation Reflector

3.3.1 Biomolecules Oven

The biomolecules' oven is composed of three different cylindrical shaped pieces: a copper outer body; a stainless steel container and a copper capillary tip. The container is fitted into the outer body through a back opening and is sealed using three M3 screws. The front side of the outer cylinder contains two openings, one that fits a 1 mm copper capillary tip and one that fits a gas inlet. A small hole was also drilled on the front side, in order to fit a thermocouple.

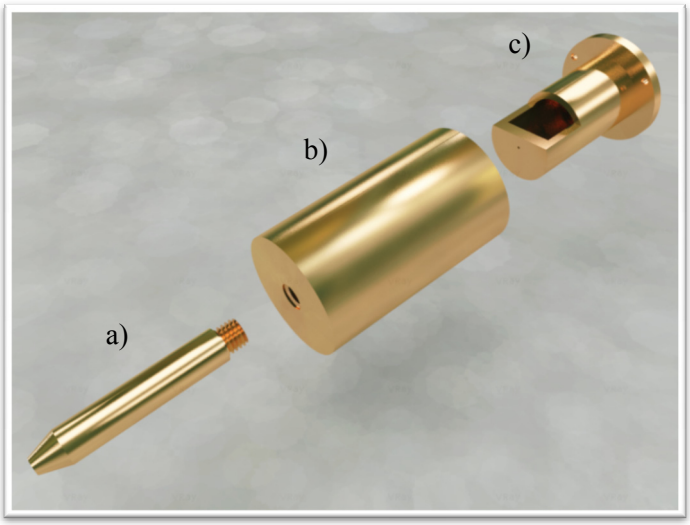

Figure 3.11 - Biomolecules' Oven: a) Capillary tip; b) Outer Body; c) Container

3.3.2 Heating system

The biomolecules' oven heating system (Figure 3.10 b and d) is composed of a halogen bulb (R7s/200Watts) and a cylindrical stainless steel reflector. The bulb holder is fixed to the reflector and placed inside it, right next to the oven. The reflector is used to increase the bulb's heating efficiency, by confining and redirecting all the dispersed radiation into the oven surface. The bulb's intensity is controlled by a variac, which is adjusted depending on the temperature required. Heating temperature is monitored in a K-type thermocouple.

3.3.3 Liquid Sample System

A sample holder for liquid samples admission was assembled outside the collision chamber and is differentially evacuated by a rotary pump (Leybold Trivac DB8) allowing the sample replacement without interfering with the vacuum conditions in the collision chamber.

The sample system is composed of three double-sided swagelok vacuum fittings (SS-4-UT-6) individually attached to quarter-turn valves (SS-4P4T-BK). The valves are all connected to a main line ¼" tubing connecting with the collision vacuum chamber after passing through a precision leak valve (Sapphire valve). The tube in the vacuum side is fitted to the Bio oven through a Swagelok Male Elbow (SS-400-2-4).

The liquid samples are introduced in a ¼" glass sample tube, which is fitted to the lower end of the swagelok vacuum fittings.

3.3.4 Biomolecular Beam Collimation Slit

This collimation slit is a 1 mm circular aperture placed 8 mm from the capillary tip (Figure 3.11) and is assembled on the same structure that holds the TOF extraction system

3.3.5 Baking System

A set of three halogens lamps (R7s/200watts) was assembled in the collision chamber in order to keep the components inside the chamber heated preventing the accumulation of the solid sample coming from the oven onto cold surfaces (especially on the collimation slit). The baking lamps are connected to a variac, adjusted to 70V, which maintains the chamber at a stable temperature of ~120ºC.

3.4 Time-of-Flight Mass Spectrometer

3.4.1 Introduction

The time-of-flight (TOF) mass spectrometer is based on the principle that ions, with different mass-to-charge ratios (m/z), accelerated with the same energy will take different flight times along a field-free region of known length.

The simplest version of a TOF mass spectrometer (Figure 3.12) comprises a short extraction region (S, usually of the order of a few millimetres), a drift region (D, from 0.5 to 4 meters length), and a detector.

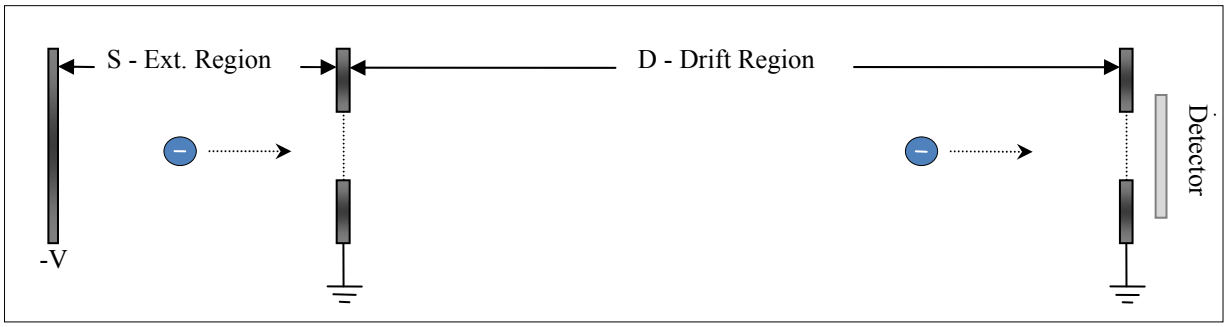

Figure 3.12 - Basic TOF configuration

In the extraction region, the ions are accelerated to a constant energy by means of an electric field, by setting a voltage to a repulsion plate. The drift region is field free and is limited by an extraction grid and a second grid placed just before the detector, both of which are generally at ground potential. The ions extracted cross this region with velocities that are inversely proportional to the square root of their masses. Thus, assuming that all ions are extracted at the same time or within a short time interval, lighter ions with higher velocities will arrive at the detector before the heavier, hence slower, ions. Ion flight times generally fall in the range of 10 to 200 µs, depending on the drift length and acceleration potential applied to the spectrometer [23].

The TOF devices present several advantages in comparison to other types of mass spectrometers: m/z range is in principle unlimited; from each ionising event a complete mass spectrum is obtained within several tens of microseconds; the transmission of a TOF analyser is usually greater than 90% [24], which implies high sensitivity; and the construction of a TOF is reasonable easy and at a low cost [24].

Within the scope of the research activities to carry out in our laboratory, a dual-stage linear time-of-flight (Wiley-McLaren based system [25]) was assembled.

3.4.2 Dual-Stage Linear Time-of-Flight

This TOF configuration was first suggested in 1955 by Wiley and McLaren and represented an enormous improvement in terms of mass resolution, especially in comparison with the then commonly used single-stage TOF.

The Dual-Stage Linear TOF main feature is the introduction of a second extraction region, which allowed the modification of the space-focusing distance. Consequently, it became possible to use longer field-free regions without losing the possibility of rectifying the flight time of identical ions created at different initial positions. Since flight length and space-focusing are two of the most significant parameters, regarding mass resolution, the new TOF spectrometers were capable of achieving considerable resolutions.

The TOF schematics in Figure 3.13 consists of an extraction region (S), an acceleration region (d), a field-free drift tube (D) and a detector. The ions, created in between the repeller plate and the first grid, are pushed to the next section by means of an electric field (E_a). As they reach the second region, they are accelerated toward the drift section due to a second electrostatic field (E_b). Once in the field-free region, ions with different masses will fly with particular velocities making them to arrive at the detector at different times. Ions reaching the detector are registered and the corresponding flight times recorded allowing to obtain a time-of-flight mass spectra.

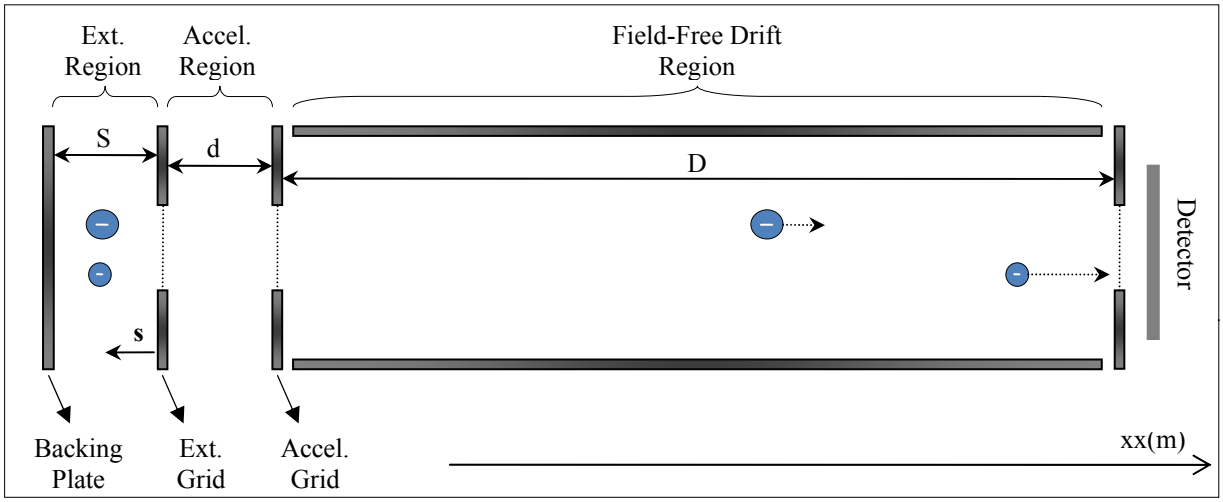

Figure 3.13 - Dual-Stage TOF mass spectrometer

3.4.2.1 Time-of-flight Equation

The total TOF is given by

$$t_{TOF} = t_a + t_b + t_D \ , \tag{3.3}$$

where t_a represents the flight time in the extraction zone, t_b the flight time in the acceleration zone and t_D the flight time in the field-free drift region. Similarly, the total energy of the ions, as they cross the drift section, can be described as

$$U = U_0 + U_a + U_b = U_0 + q.E_a.s + q.E_b.d \ , \tag{3.4}$$

in which U_0 expresses the ion initial kinetic energy, U_a the kinetic energy gained in the extraction region and U_b the kinetic energy achieved in the acceleration region.

The position equation that describes the motion of the charged particles in the extraction region is given by:

$$x = x_0 + v_0 t_a + \frac{1}{2} a_a {t_a}^2 \ . \tag{3.5}$$

where x_0 represents the ions initial position, v_0 the initial velocity and a_a the acceleration in the extraction region. Given that $x - x_o = s$, equation (3.5) can be rearranged and solved with respect to the time spent in this region as

$$\frac{1}{2} a_a {t_a}^2 + v_0 t_a - s = 0 \Leftrightarrow t_a = \frac{-v_0 \pm \sqrt{v_0^2 + 2a_a.s}}{a_a} \ . \tag{3.6}$$

The initial velocity (v_0) and the acceleration (a_a) present in equation (3.6) can also be described as

$$U_0 = \frac{1}{2} m v_0^2 \Leftrightarrow v_0^2 = \frac{2U_0}{m} \Leftrightarrow v_0 = \pm\sqrt{\frac{2U_0}{m}} \tag{3.7}$$

and

$$a_a = \frac{F}{m} = \frac{qE_a}{m} \ . \tag{3.8}$$

Therefore, by applying (3.7) and (3.8) to equation (3.6), is possible to express the ions' flight time, in this regions, as

$$t_a = \frac{\mp\sqrt{\frac{2U_0}{m}} \pm \sqrt{2}.\sqrt{\frac{U_0}{m} + \frac{qE_a}{m}s}}{\frac{qE_a}{m}} \Leftrightarrow t_a = \frac{(2m)^{1/2}}{qE_a}.\left[\mp U_0^{1/2} \pm (U_0 + qsE_a)^{1/2}\right], \tag{3.9}$$

in which four mathematical solutions are permitted, two positive and two negative. Since there is no physical meaning for solutions containing t <0, equation (3.9) becomes

$$t_a = \frac{(2m)^{1/2}}{qE_a}.\left[(U_0 + qsE_a)^{1/2} \mp U_0^{1/2}\right] . \tag{3.10}$$

This equation allows two solutions associated to the term $\mp U_0^{1/2}$. The solution associated with positive term ($+U_0^{1/2}$) is referring to ions created with initial velocities in the opposite direction of the extraction field. The solution associated with the negative term ($-U_0^{1/2}$) refers to ions created with initial velocities with the same direction of the extraction field.

In the second section, the acceleration region, the motion of the ions is described accordingly to the equation

$$x = x_b + v_b t_b + \frac{1}{2} a_b {t_b}^2 \ , \tag{3.11}$$

where x_b is related with the starting point of the second region, v_b the initial velocity of the ions as they enter the acceleration zone, a_b the acceleration gained by the particles in this zone and t_b represents the time spent by the ions in this region. Given that $x - x_b = d$, equation (3.11) can be rearranged and solved with respect to the time as

$$\frac{1}{2} a_b {t_b}^2 + v_b t_b - d = 0 \Leftrightarrow t_b = \frac{-v_b \pm \sqrt{v_b^2 + 2a_b.d}}{a_b} \ . \tag{3.12}$$

The initial velocity (v_b) and the acceleration (a_b) presented in equation (3.12) can also be described as

$$U_0 + U_a = \frac{1}{2} m v_b^2 \Leftrightarrow v_b^2 = \frac{2(U_0 + U_a)}{m} \Leftrightarrow v_b = \pm\sqrt{\frac{2(U_0 + U_a)}{m}} \tag{3.13}$$

and

$$a_b = \frac{F}{m} = \frac{qE_b}{m}. \tag{3.14}$$

Since the ions are coming from the extraction region, the velocity v_b will necessarily have the same direction of the field, therefore only the positive solution of (3.13) is possible.

If (3.13) and (3.14) are applied to equation (3.12) the flight time of the ions in the second region can be expressed as

$$\begin{aligned} t_b &= \frac{-\sqrt{\frac{2(U_0+U_a)}{m}} \pm \sqrt{2}.\sqrt{\frac{(U_0+U_a)}{m} + \frac{qE_b}{m}d}}{\frac{qE_b}{m}} \Leftrightarrow \\ \Leftrightarrow t_b &= \frac{(2m)^{1/2}}{qE_b}.\left[-(U_0+U_a)^{1/2} \pm \left(U_0+U_a+qdE_b\right)^{1/2}\right] \end{aligned} \tag{3.15}$$

Knowing that $t_b \geq 0$, $U_b = q.E_b.d$ and $U - U_b = U_o + U_a$, equation (3.15) can be rewritten as

$$t_b = \frac{(2m)^{1/2}}{qE_b}.\left[U^{1/2} - \left(U_0 + qsE_a\right)^{1/2}\right]. \tag{3.16}$$

The equation that determines the motion of the ions in the field free region is defined by

$$x = x_D + v_D.t_D \ , \tag{3.17}$$

where x_D represents the starting point of the drift zone, v_D the ions velocity as they enter the field free region and t_D the total flight time in this region.

Given that $x - x_D = D$, equation (3.17) can be expressed as

$$t_D = \frac{D}{v_D} \ . \tag{3.18}$$

The ions velocity can be defined in terms of the total energy (U) as

$$U = \frac{1}{2}mv_D^2 \Leftrightarrow v_D^2 = \frac{2U}{m} \Leftrightarrow v_D = \sqrt{\frac{2U}{m}}. \tag{3.19}$$

Therefore, if (3.19) is introduced in (3.18), the TOF equation in the drift region can be presented as

$$t_D = \frac{D}{\sqrt{2U/m}} \Leftrightarrow t_D = \frac{\sqrt{2m}D}{2\sqrt{U}}. \tag{3.20}$$

Finally, if t_a(3.10), t_b(3.16) and t_D(3.20) are replaced and rearranged in equation (3.3) , the general TOF equation can be defined as

$$t = \sqrt{\frac{m}{2}} \times \left[\frac{2\left(\sqrt{U_o + q.s.E_a} \pm \sqrt{U_o}\right)}{q.E_a} + \frac{2\left(\sqrt{U} - \sqrt{U_o + q.s.E_a}\right)}{qE_b} + \frac{D}{\sqrt{U_o + q.s.E_a + q.d.E_b}} \right] \tag{3.21}$$

If ions are considered to have no initial kinetic energy ($U_0 = 0$), equation (3.21) turns

$$t_{U_0=0} = \sqrt{\frac{m}{2.q.Ea}} \times \left[2\sqrt{s} + \frac{2d}{\sqrt{\sigma} + \sqrt{s}} + \frac{D}{\sqrt{\sigma}} \right], \tag{3.22}$$

where $\sigma = s + d\frac{E_b}{E_a}$.

3.4.2.2 Mass Resolution

The mass resolution $\frac{m}{\Delta m}$, is defined by the width of a peak at a specific fraction of the peak height [24], where Δm is measured as the full width at half maximum (FWHM) [23].

To find the resolution expression for a TOF system, equation (3.21) must be rearranged with respect to mass (m), as follows

$$m = \frac{2t^2}{z}, \tag{3.23}$$

where

$$z = \left[\frac{D}{\sqrt{U_o + q.s.E_a + q.d.E_b}} + \frac{2\left(\sqrt{U_o + q.s.E_a} \pm \sqrt{U_o}\right)}{q.E_a} + \frac{2\left(\sqrt{U} - \sqrt{U_o + q.s.E_a}\right)}{qE_b} \right]. \tag{3.24}$$

The derivative of (3.23) can be expressed as

$$\Delta m = \frac{4t}{z}\Delta t \ . \tag{3.25}$$

The general equation of mass resolution in a TOF device can be obtained by making use of (3.23) and (3.25), yielding

$$\frac{m}{\Delta m} = \frac{t}{2\Delta t} \ , \tag{3.26}$$

where t is the TOF of a given mass and Δt the full width at half maximum of the corresponding peak.

From (3.26) is possible to infer that the mass resolution depends on the time resolution and therefore on pulse widths, detector response times, recorder bandwidths and initial space and energy distributions.

3.4.2.3 Spatial distribution

Since, in real experiments, ions are not created in a single spot in space, but rather in a particular collision volume, there will be an initial spatial distribution of the ions that can cause considerable resolution limitations in TOF devices. The spectrometer's ability to resolve masses, despite the initial space distribution, is described as spatial resolution.

The ion initial space distribution can be considered as the deviation of the initial position (s_0) about its average (Δs_0), so that $s_{\max} = s_0 + \frac{1}{2}\Delta s$ and $s_{\min} = s_0 - \frac{1}{2}\Delta s$. As a result, ions created in different initial positions in the extraction region will be accelerated through different distances in the extracting field, resulting in a distribution of final kinetic energies. This distribution implies a broadening and tailing of the mass spectrum peaks, since ions with the same m/z ratio will take different time intervals to reach the detector. There is, however, a focal point, known as the space focus plane (Figure 3.14), where the faster ions formed close to the extraction plate will reach the slower ions formed far from the repeller plate. This point is mass independent and for a single-stage TOF system is placed at a distance of $2s_0$, where s_0 represents the distance from the extraction grid to the centre of the extraction region (normally $s_0 = \frac{S}{2}$).

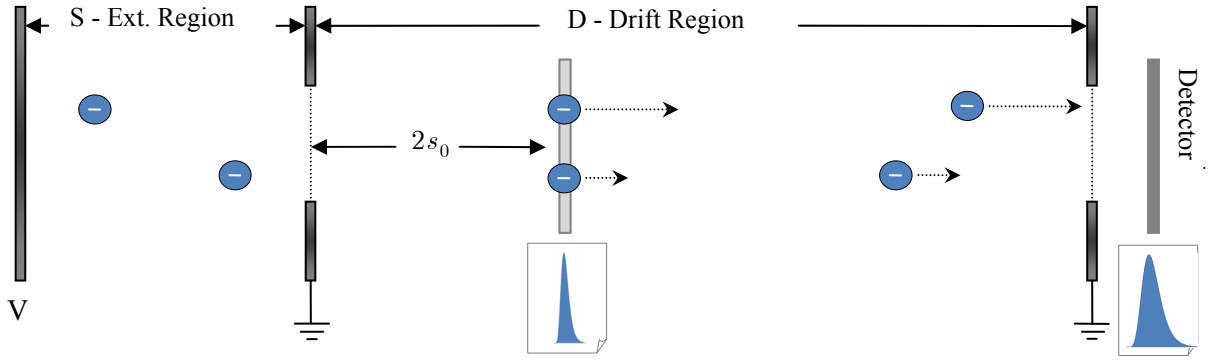

Figure 3.14 - Single-stage TOF focal plane

In the single-stage TOF, the focus plane is located at a small and fixed distance from the extraction grid making difficult a suitable mass dispersion, since there is no time for the ions with different m/z ratios to drift away from each other. To solve this, a second region (acceleration region – d) can be introduced, which allows the space-focus plane to be moved far away from the extraction region.

In Figure 3.15, the dual-stage TOF moves the focal plane to a more distant point in space, which is also used for placing the detector. The focal point location will be determined by the ratio $\frac{E_b}{E_a}$. Thus, longer focal distances will be achieved with higher ratios of extraction field/acceleration field.

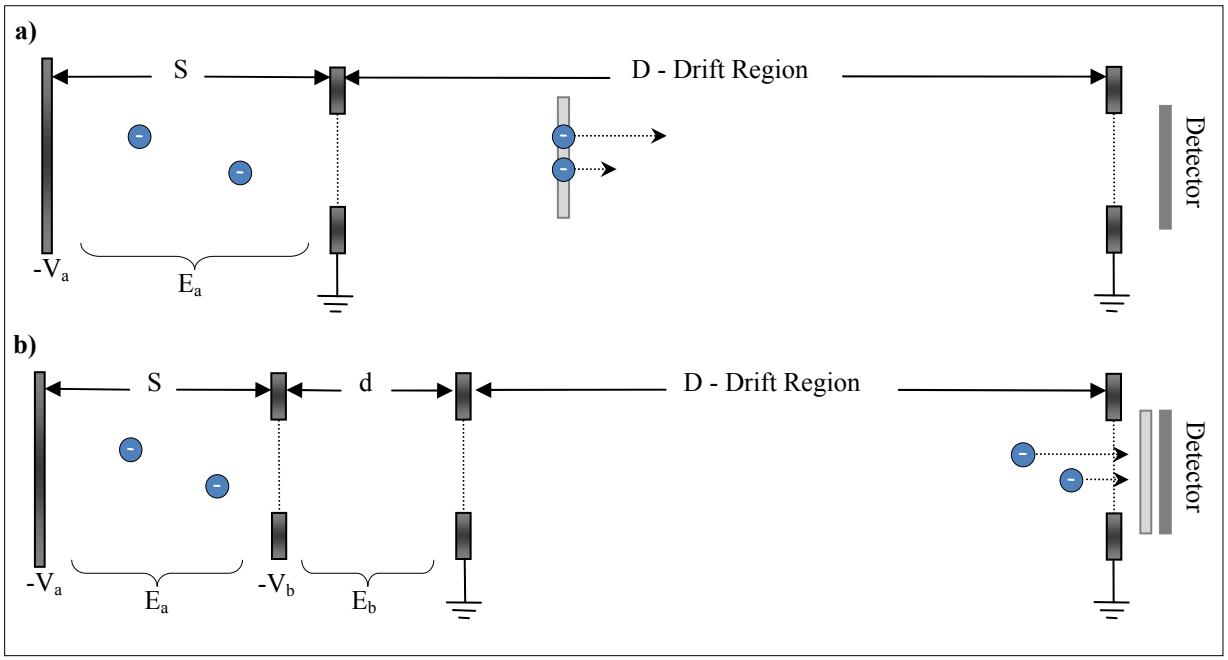

Figure 3.15 - Comparison of single-stage (a) and dual-stage (b) extraction

To find the location of the focal plane, is necessary to find the maximum, minimum or inflection points of the time-of-flight in equation (3.22). It is known that around these particular values, a small deviation in the ions initial positions (Δs) will make no significant changes in the ions flight times allowing the focal condition to be fulfilled.

The condition for which the TOF function reaches its maximum, minimum or inflection point, is determined using the derivative of the (3.22) expression, assuming that ions are created in the collision centre ($s = s_0$) with no initial kinetic energy ($U_0 = 0$), as follows

$$\frac{d\left(t_{(U_0=0,s=s_0)}\right)}{ds} = \sqrt{\frac{m}{2.q.Ea}}\left(\frac{1}{\sqrt{s_0}} - \frac{D}{2(\sigma_0)^{3/2}} - \frac{d}{s_0\sqrt{\sigma_0} + \sqrt{s_0}\sigma_0}\right) = 0 , \tag{3.27}$$

where $\sigma_0 = s_0 + d\frac{E_b}{E_a}$.

The length of the drift region (D), where the TOF system will satisfy the space-focus condition, can be determined by solving equation (3.27) in respect to D, as

$$D = 2(\sigma_0)^{3/2}\left(\frac{1}{\sqrt{s_0}} - \frac{d}{s\sqrt{\sigma_0} + \sqrt{s}\sigma_0}\right) . \tag{3.28}$$

Furthermore, through the analysis of equation (3.28), space focusing process is mass independent and is possible to control the length of the necessary drift region by changing the ratio of the applied electric fields (since $\sigma_0 = s_0 + d\frac{E_b}{E_a}$).

Another important issue is related to the determination of the mass resolution limitation inflicted by the ions initial spatial distribution. Therefore, the maximum resolvable mass ($M_{Spatial}$) can be calculated using the general resolution equation (3.26) and the TOF equation (3.22), as follows

$$\frac{m}{\Delta m} = \frac{t}{2\Delta t} \Leftrightarrow M_{Spatial} = \frac{t_{U_0=0}(s = s_0)}{2\Delta t_{\Delta s}} \tag{3.29}$$

where $\Delta m = 1$, defining that the last separable consecutives masses will possess peaks with a full width at half maximum of one mass unit. It is also important to note that if $t_{U_0=0}(s = s_0)$ is a maximum or a minimum of the total TOF function, then $\Delta t_{\Delta s} = t(s_0) - t(s_0 + \frac{1}{2}\Delta s)$.

3.4.2.4 Kinetic Energy Distributions

Ions may be created with some initial kinetic energy, not only with different velocity intensities but also with an isotropic velocity distribution. This kinetic energy distribution implies a broadening and tailing of the mass spectrum peaks, since ions with the same m/z ratio will take different time intervals to reach the detector. The ability of the spectrometer to resolve masses in spite of the initial kinetic energy distribution is known as kinetic energy resolution.

To investigate the effects of initial velocities on the ions' flight time, it is of interest to choose the circumstances where the ions that takes longer and shorter time intervals to reach the detector. Therefore, it is convenient to consider two ions formed in the same initial position $s_0 = \frac{S}{2}$, with equal, but oppositely directed velocities (as seen in Figure 3.16).

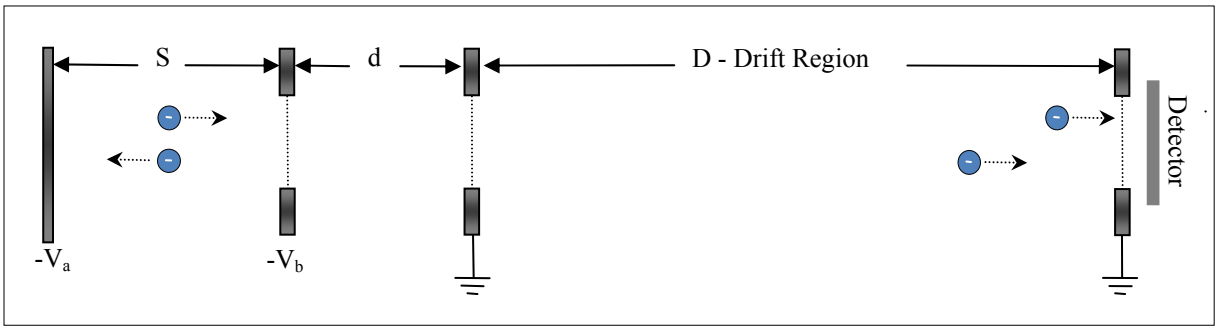

Figure 3.16 - Two ions with different initial kinetic energies

One of the ions moves away from the detector, decelerating due to the extraction field until it stops. It is then accelerated, returning to s_0 with its original speed. Therefore, and since the extraction field presents conservative characteristics, both of the ions leave the extraction region with the same energy, separated only by the "turn-around" time.

When taking a look at the general TOF equation (3.21), it is possible to realize that ions created at the same initial position and with the same initial energy U_0 can only carry a time difference if they are formed with opposite velocities. The velocity direction related information can only be introduced in equation (3.10) through the term $\mp U_0$. Therefore is possible to say that the total TOF difference between these two ions (i.e. the "turn-around" time) can be evaluated using (only) the TOF equation (3.10), regarding the extraction region.

To determine the mass resolution limitation associated with the initial kinetic energy, two particles with the same mass formed in the same initial position (s_0) but with velocities with opposite directions are considered. The TOF spent in the extraction region by each particle can be found using equation (3.10), as follows

$$\begin{cases} t_{a1} = \dfrac{(2m)^{1/2}}{qE_a}\left[(U_0 + qs_0E_a)^{1/2} - (U_0)^{1/2}\right] \\ t_{a2} = \dfrac{(2m)^{1/2}}{qE_a}\left[(U_0 + qs_0E_a)^{1/2} + (U_0)^{1/2}\right] \end{cases}, \tag{3.30}$$

and the time difference between then can be defined as

$$\Delta t_{\Delta U} = t_{a1} - t_{a2} \Leftrightarrow \Delta t_{\Delta U} = \frac{2.(2mU_0)^{1/2}}{qE_a} \quad . \tag{3.31}$$

The maximum resolvable mass associated with the initial kinetic energy ($M_{Kinetic}$) can be calculated with the resolution equation (3.26) when $\Delta m = 1$, as

$$\frac{m}{\Delta m} = \frac{t}{2\Delta t} \Leftrightarrow M_{Kinetic} = \frac{t_{U_0=0}(s_0)}{2.\Delta t_{\Delta U}} \tag{3.32}$$

where $t_{U_0=0}(s_0)$ is evaluated using the equation (3.22) and $\Delta t_{\Delta U}$ through the equation (3.31)

3.4.2.5 Temporal Distributions

These distributions are related with several factors including the time of ion formation as well as limitations of the ion detectors and the time-recording devices [23]. In instruments where ions are created in the gas phase by pulsed beams of electrons or atoms, with pulse widths of a few microseconds (1 to 5 μs), there is an obviously time distribution associated with the ion formation time. In this case, temporal uncertainty can be reduced by creating the ions in a field free region and then extracting them with a draw out pulse with fast rise times.

Ion detectors are also important elements when speaking about temporal distributions. For example, when low rise time (15 ns) detectors such as channeltrons are used, significant timing limitations can be established. Such limitations can be related not only to the fact that the detector takes too long to recover from an ion arrival (~25 ns in the case of rise times of 15 ns) leaving subsequent ions undetected, but also because it will cause the ion detection to occur with a significant time shift from its actual arrival. Another time limitation related with the use of channeltrons is its conical shape, which can cause similar ions to be detected with different time of flights, depending on the depth at which they reach the detector. To prevent these temporal limitations, high performance plane detectors such as channelplates (0.5 ns rise times) are used.

Time-recording devices with a suitable time resolution (bellow 2 ns) are also important, allowing ions with a very small time difference to be differentiated, which can lead to better resolved mass spectrum.

3.4.2.6 Overall Resolution

Due to the difficulty of quantifying the contribution of the temporal distributions to the resolution limitations, the TOF overall resolution will be estimated combining, only, the contribution of the spatial (equation (3.29)) and the kinetic energy (equation(3.32)) distributions, as follows

$$\frac{1}{M_{Total}} = \frac{1}{M_{Spacial}} + \frac{1}{M_{Kinetic}} \tag{3.33}$$

where M_{total} represents the last resolvable mass due to both spatial and kinetic energy effects.

3.4.3 Implemented TOF

This device is based on a dual-stage TOF (Wiley-McLaren) geometry, presented in detail in section 3.4.2 , and is composed of an ion extraction system, a drift tube and a detector (Figure 3.17).

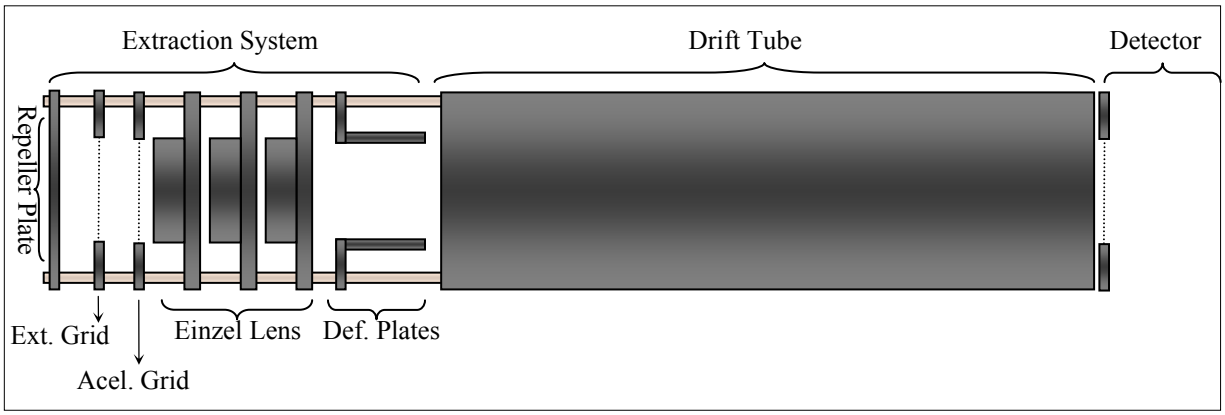

Figure 3.17 - Schematics of the implemented TOF spectrometer

3.4.3.1 Extraction System

This system is composed of a repeller plate, an extraction grid, an acceleration grid, an einzel lens and a pair of deflecting plates (Figure 3.18).

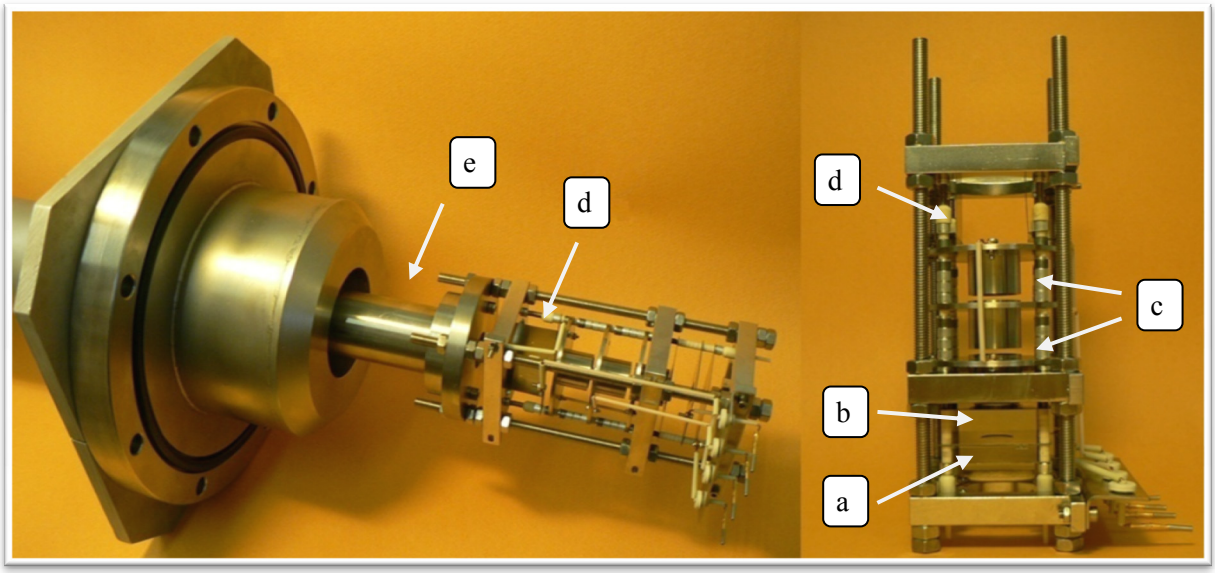

Figure 3.18 - Extraction system: a) Extraction region; b) Acceleration region; c) Einzel lens; d) Deflecting plates; e) Flight tube

Three stainless steel structures hold the ceramic alumina rods that support and align all the elements, kept in place through alumina spacers. The repeller plate is a simple 40 × 40 × 0.5 mm stainless steel sheet. The extraction and acceleration grids are also 40 × 40 × 0.5 mm stainless steel sheets, but with a centred 15 mm diameter hole, where a stainless steel grid (of 91% transparency) was welded. The einzel lens is composed of three similar stainless steel cylinders, 18 mm long with an inner diameter of 16 mm, separated 2 mm from each other. Finally, the deflector plates are two 30×28 mm parallel stainless steel plates, placed after the einzel lens.

The extraction region is defined by the repeller plate and the extraction grid 12mm apart. The collision centre, where the neutral potassium beam and the target beam cross, is placed in the mutual distance of this region. A negative DC potential of -3500 V is constantly applied to both the repeller plate and the extraction grid, through an ORTEC 659 5kV power supply. An extra -400 V fast rise time (15 ns) pulse is added to the repeller plate potential through the Jordan D-1040 Pulser, causing the negative ions to leave this region into the acceleration region. The pulse duration is typically one microsecond, but can vary according to the fragments' mass rating.

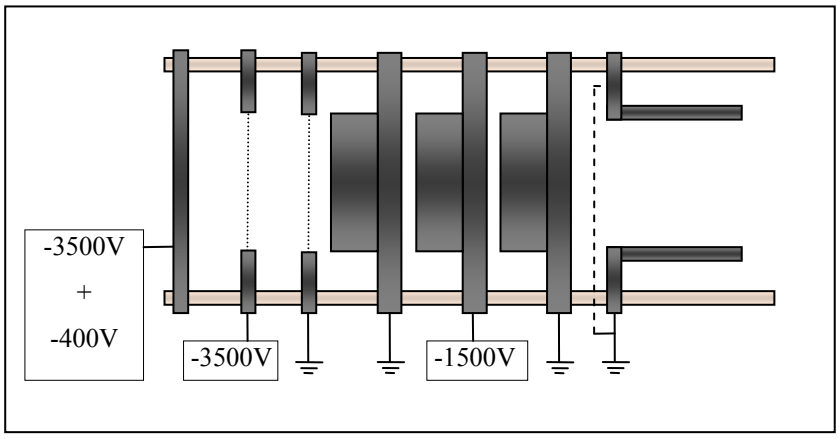

Figure 3.19 - TOF extraction system electrical connections

The acceleration region is also 12 mm wide and is defined by the extraction and acceleration grids. Ions entering this region will suffer an acceleration due to the -3500 V, constantly applied to the extraction grid with respect to the grounded acceleration grid, causing the ions to leave this region and enter the einzel lens zone.

The einzel lens works like a typical optical lens system, making the ions converge to a focal point. The location of this point is controlled by the electric potential applied to the middle element, while the outer cylinders are kept grounded in order to guarantee that the ions total kinetic energy is kept unchanged. The voltage applied to the central cylinder was -1500 V (Leybold 52170), setting the focal point near the detector, increasing therefore the efficiency of collected ions.

After leaving the lens system, ions enter the deflecting plates that are kept at a ground potential, since no significant improvement in the detection efficiency has been noticed. After that, ions enter the drift tube also known as free field region.

3.4.3.2 Drift Tube

The drift tube is one meter long stainless steel CF63 straight connector kept at ground potential. One side of the tube is attached to the extraction system, while the other is connected to a four way cross where the detector, a turbo pump, responsible for the differential pumping, and a penning gauge are placed.

3.4.3.3 Channeltron Detector

The detector employed in this system was a channeltron (Burle 7010), operating in pulse counting mode. The detector is composed of a spiralled tube structure with a 10 mm conical shaped entrance. An electric potential of +2000 V is applied (Heizinger HNC 6000-10) to the detector according to Figure 3.20. The cascade of electrons, triggered from only one initial particle, is collected by the metal anode placed at the rear end of the detector due to a voltage drop. As a result, for each ion impact, the channeltron generates a negative voltage pulse with 20 ns duration and an amplitude of typically 20 mV. This signal is amplified through the ORTEC VT-120 pre-amplifier and enters the FastComtec P7888 multiscale.

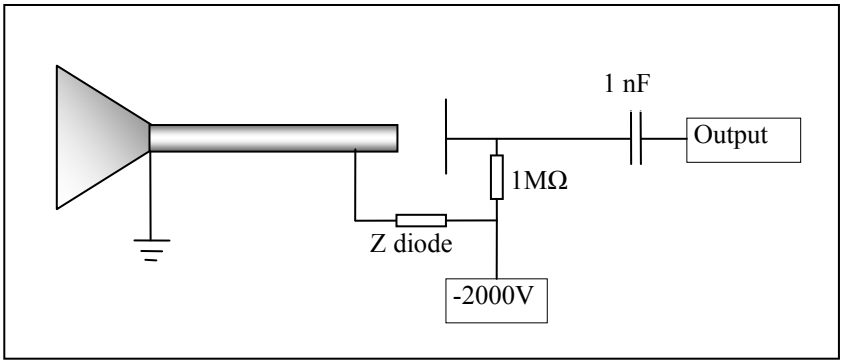

Figure 3.20 - Schematics of channeltron pulsed mode electrical connections for negative ion detection

3.4.4 System Characterization and Optimization

3.4.4.1 TOF Characterization

In order to facilitate a quick analysis of the system characteristics dependence on the geometric parameters of the TOF, a mathematical routine was developed in Wolfram´s software Mathematica. This algorithm is based in the mathematical analysis presented in chapter 3.4.2 , and allows to pre-define the TOF geometric parameters, the extraction region voltage (V_a), the deviation in the ions initial positions (Δs) and the kinetic energy release (ΔU). The result allows determining the spatial resolution, the kinetic energy resolution, the acceleration voltage and the TOF of a chosen mass. As a result, the parameters presented below were all obtained using the algorithm mentioned above.

- **Acceleration Voltage (V_b)**

Using the condition given by equation (3.27) and the geometric parameters of the implemented TOF (S=12 mm; d=12 mm and D=1447 mm), the ratio $\frac{E_b}{E_a}$ was obtained. This ratio can be used to specify the acceleration voltage in terms of the voltage applied to the extraction region, as follows

$$\frac{E_b}{E_a} = 12.266 \Leftrightarrow \frac{\frac{V_b}{d}}{\frac{V_a}{S}} = 12.266 \Leftrightarrow V_b = \frac{12.266 \times V_a \times d}{S} \ . \tag{3.34}$$

Thus, using (3.34) and assuming a pulse applied to the extraction region of $V_a = -400$ V , is possible to compute the acceleration voltage that allows this system to fulfil the space focusing condition i.e. $V_b = -4907$ V .

- **Mass Resolution (M_{Total})**

To estimate the overall resolution was necessary to calculate the spatial and kinetic energy resolutions separately. In both cases the geometric parameters considered were S=12 mm, d=12 mm and D=1447 mm, as well as the applied voltages presented before $V_a = -400\ \mathrm{V}$ and $V_b = -4906\ \mathrm{V}$.

Since the kinetic energy release will vary depending on the fragment anion, the kinetic energy resolution ($M_{Kinetic}$) was calculated using (3.32), considering the energy interval $\Delta U = [0.1\,,\,2]\,\mathrm{eV}$ (Figure 3.21). This interval was chosen based on scientific publications regarding negative ions formation [26], where the majority of the dissociated fragments have been reported to have kinetic energy release within the selected range.

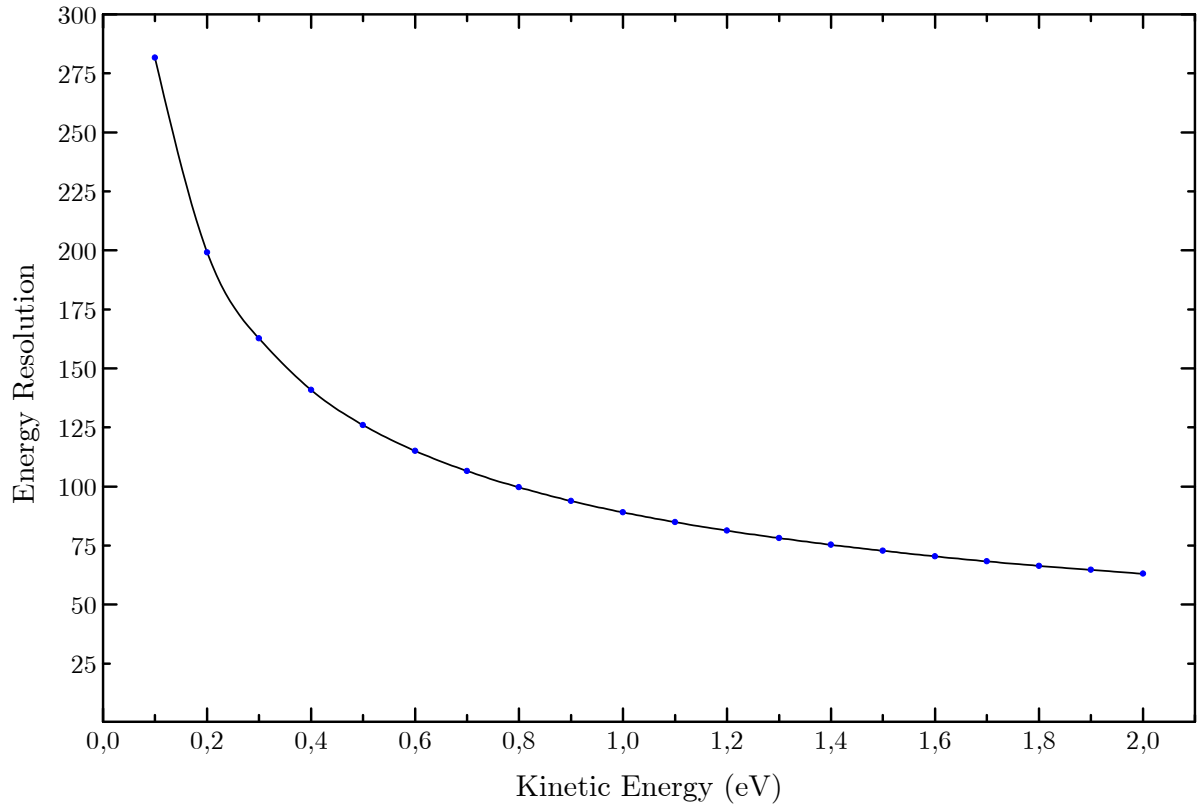

Figure 3.21 - Energy resolution dependence with the ion kinetic energy release

The theoretical spatial resolution was calculated by making use of equation (3.29), where a deviation in the ions' initial positions of $\Delta s = 2mm$ was assumed,

$$M_{Spatial} = \frac{t_{U_0=0}}{2\Delta t_{\Delta s=0.2mm}} \Leftrightarrow M_{Spatial} = 4899 \tag{3.35}$$

Considering that the total resolution depends greatly on parameters that are difficult to determine with accuracy (such as kinetic energy release, deviation in the ions initial positions and temporal distributions) the calculated overall resolution represents only an approximation of the actual TOF mass resolution.

Using the calculated spatial resolution $M_{Spatial} = 4899$, the energy resolution $M_{kinetic} = 125$ (calculated considering a kinetic energy release of 0.5 eV) and equation (3.33), was possible to estimate the overall resolution to be $M_{Total} = 122$

3.4.4.2 Experimental Acceleration Voltage

In order to achieve an extracting field density with the same order of magnitude as reported in similar TOF systems [25], a –400V pulse was applied to the extraction region. In order to experimentally determine the acceleration voltage that fulfils the space focus condition when $V_a = -400\mathrm{V}$, a set of measurements were performed using nitromethane (CH_3NO_2) as a calibrating molecule. Several spectra were obtained where different voltages have been applied to the acceleration region. They started with a wide voltage interval (–3000V to –5000V) measured in large voltage steps (–500V), and ended with a shorter voltage interval (–3200 to –4000) measured in smaller voltage steps (–100V). In Figure 3.22, three TOF spectra of CH_3NO_2 at different acceleration voltages are shown, around the region of the most intense negative fragment (NO_2^-).

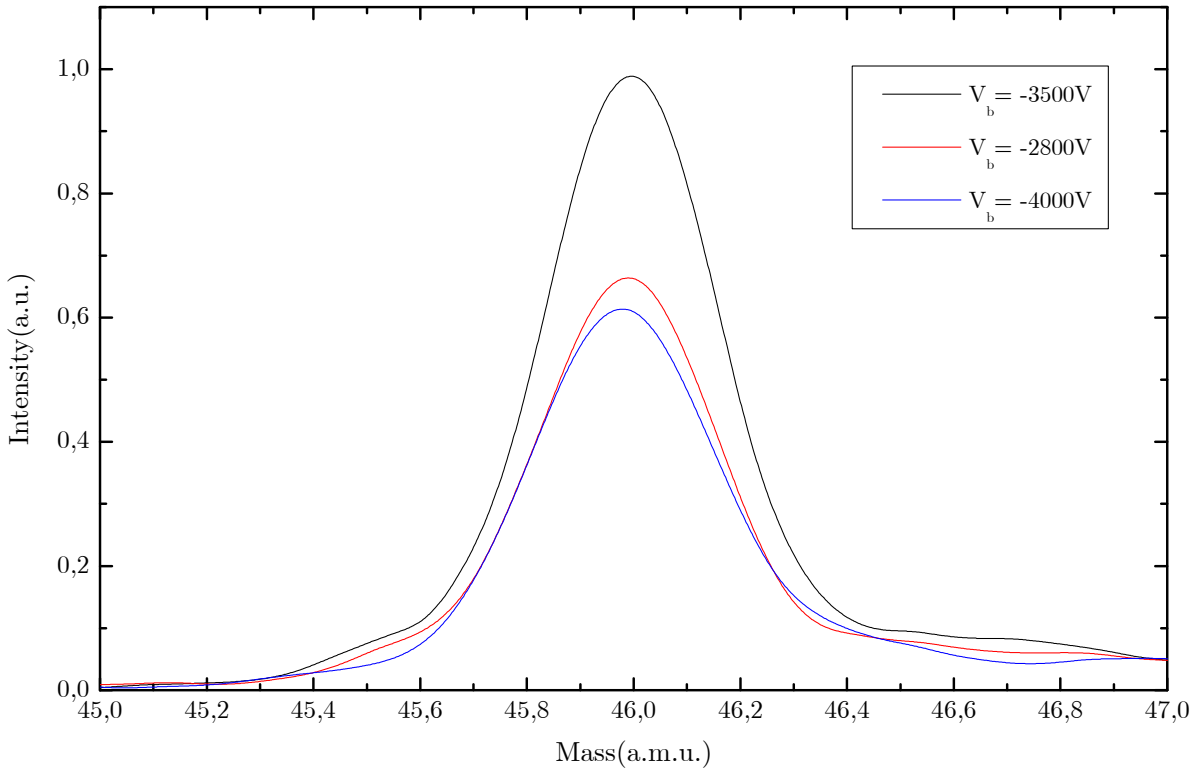

Figure 3.22 - NO_2^- peak of nitromethane mass spectrum at different acceleration voltages

From the analysis of the plot shown above (Figure 3.22), the intensity, FWHM and mass resolution associated with the 46 m/z were determined. This information was organized as presented in Table 3.3, from which is possible to realize that the best resolved and more intense peak is associated with an acceleration voltage V_b= –3500V.

Table 3.3 - NO_2^- peak characteristics at different acceleration voltages

V_b(V)	Mass(a.m.u)	Intensity(a.u.)	FWHM(a.u.)	m/Δm
–3500V	46	1	0.38	121
–2800V	46	0.67	0.40	115
–4000V	46	0.62	0.41	112

Only the NO_2^- peak, at three different acceleration voltages, was shown here. However, this study was repeated for the most relevant peaks of the nitromethane spectrum at several acceleration voltages. The overall outcome of this experimental study dictated the most suitable acceleration voltage to be $V_b = -3500V$, which is significantly different from the calculated value of

$V_b = -4907V$. Although these values differ quite significantly, this difference can be due to effects related with the non-uniformity of the applied electric fields, the effective voltage pulse being lower than $-400V$ and the non-flat entrance shape of detector (channeltron). Another noteworthy fact is the small deviation in terms of resolution (see Table 3.3), around the space focusing acceleration voltage, where it was expected to dramatically increase the resolution. This clearly suggests that another contribution rather than the spatial focusing is limiting the TOF performance (probably related to the kinetic energy release of the fragments).

3.4.4.3 Experimental Einzel Lenses Voltage

The main purpose of the einzel lens system is to increase the number of ions that reach the detector, by focusing the diverging ion beam into the channeltron entrance. An experimental study was conducted to determine the most appropriate voltage to be applied in the middle element of the einzel system. A set of nitromethane TOF measurements was performed, using several einzel voltages ranging from –1000V to –2000V with voltage steps of –100V. Three of those spectra are presented in Figure 3.23, where is possible to conclude that the most intense spectrum is associated with $V_{einzel} = -1500V$.

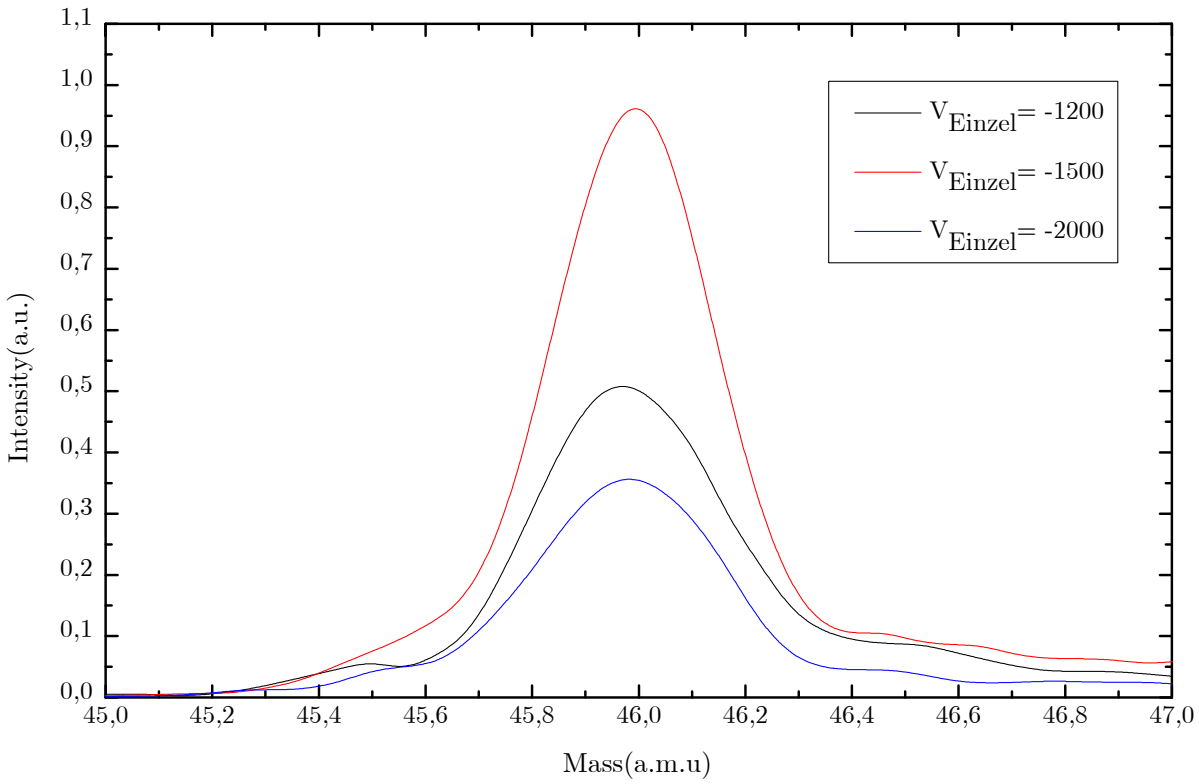

Figure 3.23 - NO_2^- peak of the nitromethane mass spectrum at different einzel lens voltages

3.4.4.4 Mass Calibration

As mentioned before, the TOF spectrometer is capable of separating ions depending on their mass-to-charge ratio (m/z). However, the spectrum itself is originally recorded as a function of time-of-flight versus number of events (counts). To be able to identify the mass of the ions present in a spectrum is necessary to make the conversion of the time into a mass scale. For that, a calibration must be performed, in which a molecule with a well known fragmentation pattern is measured, allowing to establish a correlation between the flight times of the ions and the respective masses. Knowing that for any given TOF spectrometer, the mass scale follows a square root law and using the flight times of known masses, it is possible to calibrate the mass spectra by determining the constant *a* and *b* in the next equation

$$t = a\sqrt{m} + b \ , \tag{3.36}$$

where b takes into account any time offsets introduced by the acquisition system.

In this particular case we made use of nitromethane, which negative ion formation has been studied in the past [27]. The calibration process was performed iteratively (see Table 3.4), starting with a preliminary calibration using only three well known negative fragments, and subsequently increasing the number of fragments used, throughout the application of the previous calibration function to the nitromethane TOF spectrum. Thus, from each new calibration it became possible to unequivocally identify new fragments. These fragments are then included in the subsequent calibration iteration, allowing a more accurate determination of the mass calibration.

Table 3.4 - Mass Calibration Iterations

Iteration	Fragments	Mass(a.m.u)	Channel – 8ns	*a*	*b*
1st	H^-	1	290	223.61	67.42
	O^-	16	962		
	NO_2^-	46	1584		
2nd	H^-	1	290	223.64	67.27
	O^-	16	962		
	NO_2^-	46	1584		
	$CH_3NO_2^-$	61	1814		

3rd	H^-	1	290	224.07	64.50
	O^-	16	962		
	OH^-	17	990		
	CN^-	26	1208		
	NO^-	30	1292		
	NCO^-	42	1516		
	NO_2^-	45	1584		
	$CH_2NO_2^-$	60	1799		
	$CH_3NO_2^-$	61	1814		
	$(ClU–H)^-$	145	2763		

To produce a precise calibration within a more comprehensive mass range, it was necessary to include a high mass negative ion in the calibration process. For that, in the last performed iteration, the fragment $ClU–H^-$ (dehydrogenated 5-chlorouracil) retrieved from a 5-chlorouracil TOF spectrum was introduced.

In Figure 3.24 for a matter of practical convenience the vertical axis was used for the fragments mass and the horizontal axis for the respective TOF channels. The data regarding the selected fragments was plotted and a fitting performed using equation (3.36) rearranged as follows

$$m = \left(\frac{t-b}{a}\right)^2. \tag{3.37}$$

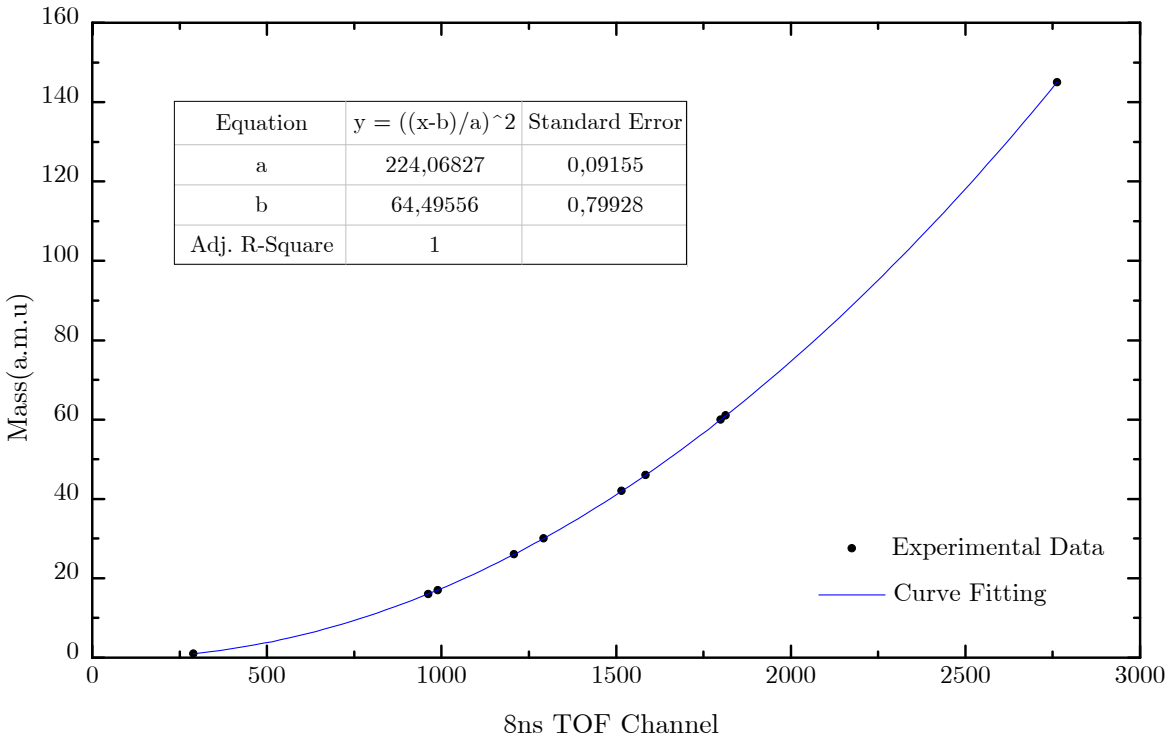

Figure 3.24 - TOF calibration curve (3º Iteration)

With this calibration process was possible to determine that for particular TOF system settings (S=12mm; d=12mm; D=1447mm; V_a= – 400V; V_b= – 3500V; V_{einzel}= – 1500V) the relation between the ions mass and their flight time (recorded in 8 ns time channels) is given by:

$$m = \left(\frac{t - 64.50}{224.07} \right)^2 \tag{3.38}$$

The mass calibrated nitromethane spectrum shown below (Figure 3.25), as well as all the subsequent mass spectra displayed in this thesis are always presented with a mass scale calculated using the calibration equation (3.38).

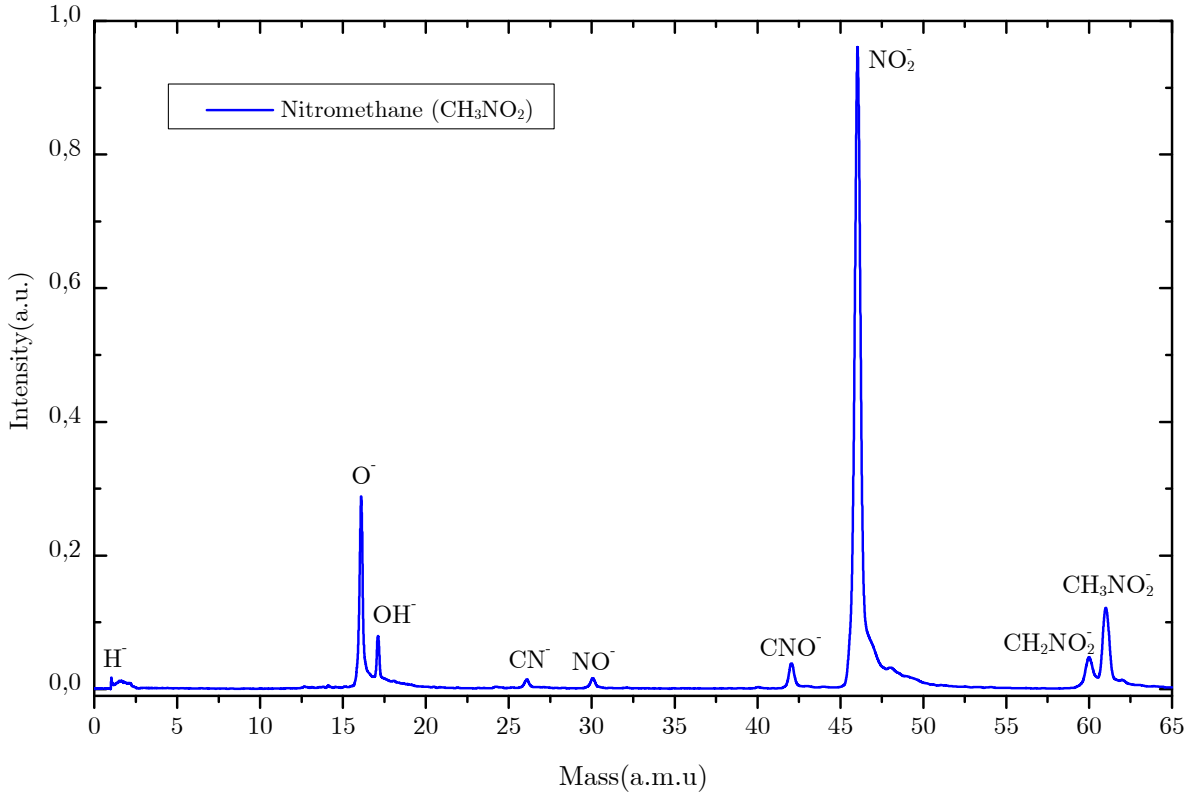

Figure 3.25 - Nitromethane anions TOF mass spectrum assignment from the collision of an effusive nitromethane beam and a 100eV neutral potassium beam.

3.5 Acquisition System

In the previous chapters we described the processes which allow the production of the projectile and target beams as well as a description of the collision fragments detection mechanism. Here we describe the acquisition system, which is responsible for making the collision process synchronous with the extraction and detection of the resulting fragments.

3.5.1 HP Pulse generator

The pulse generator HP 214B connected to the K^+ ion source is responsible for defining the kinetic energy of the K^+ ions and establishing the kinetic energy of the neutral potassium beam.

This device is a high power pulse generator delivering pulses up to 100V (into 50 Ω) at frequencies of 4 MHz with rising times of approximately 25 ns. Adjustable pulse repetition frequency, delay/advance, width and amplitude are user selected (see Table 3.5). Additional features include double pulse, external trigger, manual single pulse, and gate modes.

The pulse width used throughout the experiments was fixed to 2μs, but the amplitude and repetition frequency were selected depending on the mass of the heavier anion to detect and collision energies being used.

Table 3.5 - HP 214B Specifications

Pulse Repetition Rate	10 Hz to 10 MHz in 6 ranges. In 30V to 100V amplitude range, maximum rep. rate is 4 MHz
Pulse delay/advance	10 ns to 10 ms (± fixed delay of 45 ns)
Pulse Width	25 ns to 10 ms in 6 decade ranges
Pulse Amplitude	0.3V to 100V in 5 ranges
Pulse Polarity	Positive or negative

3.5.2 Jordan Pulse Generator

The Jordan D-1040 Pulser is used to deliver a voltage pulse to the extraction region of the TOF spectrometer. It provides voltage steps of 0 to 400V with rising and falling times of 10 nanoseconds, with variable duration and period. It can be biased up to +5000V DC and the maximum repetition rate is 30 kHz. The power supply can be adjusted to either positive or negative pulses and working with a positive or a negative bias voltage.

In this particular experimental setup a –400V voltage pulse was used with a –3500 V bias. The pulse duration and repetition rate were adjusted depending on the molecule, since larger fragments require longer pulse durations to be fully extracted and longer periods of time to be detected.

3.5.3 Ortec Pre-Amplifier

The pre-amplifier is a small device used to amplify the voltage pulses provided by the detector. It is usually placed near the detector to prevent any noise contamination, since this pulsed signal is normally very small (typically 2 mV).

The pre-amplifier used in the experiment was an Ortec VT120 that performs an inverting amplification with a voltage gain of ×200 and is capable of detecting signals with rise times below 1 ns. This device is also used to perform the electric insulation between the acquisition board and the actual detector, preventing any damages caused by the failure of the high voltage decoupling capacitor used in the channeltron polarization circuit (Figure 3.20).

3.5.4 FastComtec Acquisition Board

The acquisition board is responsible for recording the ions flight time as they arrive in the detector. The FastComtec P7888 PCI multiscaler which is one of the fastest commercially available multiple-event time digitizers, with its most relevant specifications presented in Table 3.6. Several acquisition parameters (bin width, sweep time, acquisition time, input discriminator, etc.) are user defined through a computer interface software named MCDWIN (Figure 3.26), provided by the board supplier.

Table 3.6 - FastComtec P7888 Specifications

Max. Count rate (burst)	1 GHz
Time resolution	1ns
Start/Stop input Discriminator	±3V (30mv steps)
Sweep time	32 ns to 68.7s programmable range
Operating modes	Continuous (wrap around), stop-after- sweep and sequential

In this experimental setup, the board initiates each scan from the time instant the voltage pulse is applied to the extraction region repeller plate (start pulse). Then events detected at the stop inputs

(channeltron pulses) are recorded, each in a specific time bin corresponding to the time of arrival relative to the start pulse. Each scan ends after a certain sweep time, leaving the device ready to initiate a new scan as soon as another start pulse arrives (stop-after-sweep mode). By the end of the acquisition interval a cumulative spectra is displayed by the MCDWIN software.

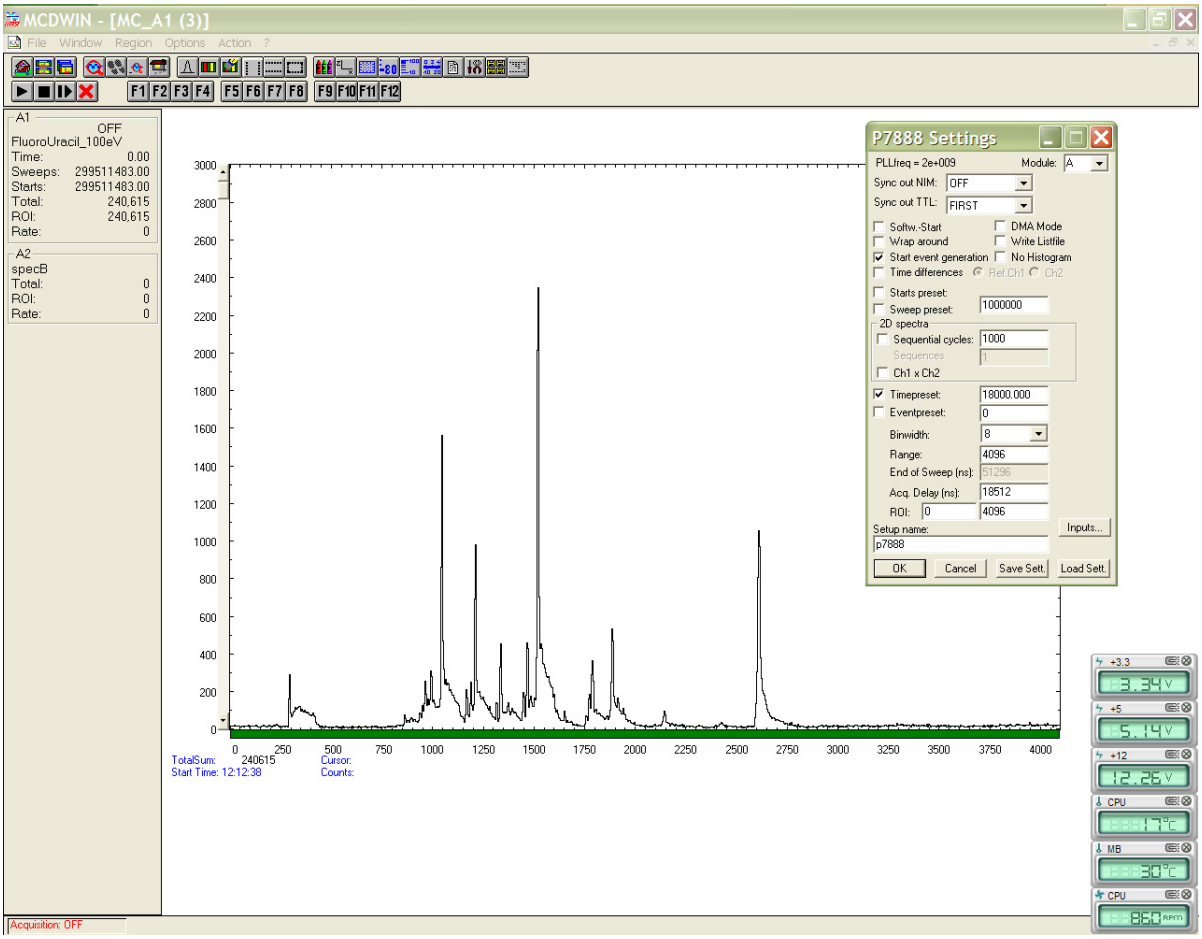

Figure 3.26 - MCDWIN Software

The minimum bin width provided by this board is 1ns. However, when using bin widths below 8 ns, the acquisition of a satisfactory spectrum was taking excessively long periods of time with no additional improvements in the spectra. As a result, the time bin width selected to perform the spectra acquisitions was typically 8 ns. The sweep and acquisition times were selected according to the molecule and collision energies.

3.5.5 LabView program

A LabView based computer program was specifically developed to manage the vacuum security system and to register the experimental conditions related to the beams' production, collision and fragment detection (see Figure 3.27).

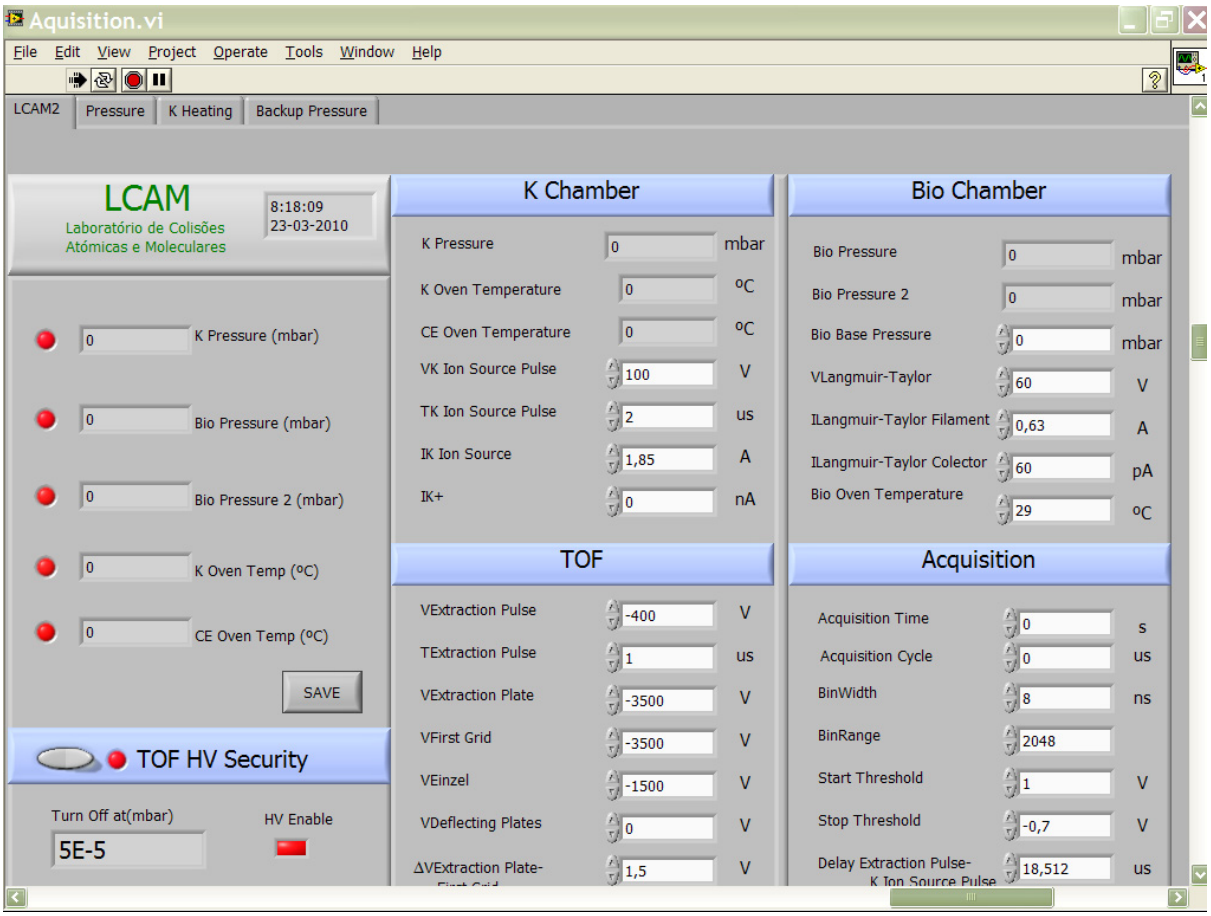

Figure 3.27 - Labview program control layout

3.5.6 Operation Mode

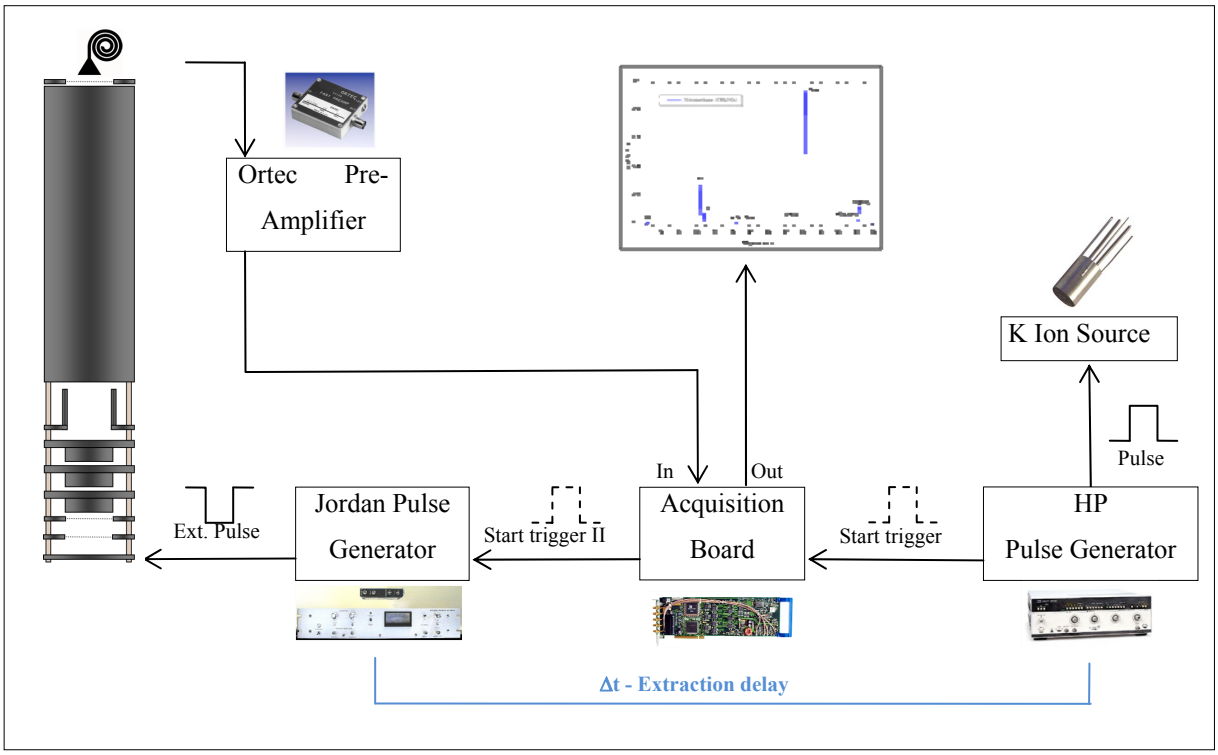

Figure 3.28 - Acquisition Layout

The acquisition process, presented in Figure 3.28, starts when a 2µs pulse is applied by the HP 214B to the K^+ ion source allowing the production of the neutral potassium beam (pulsed mode operation). At the same time a trigger signal is sent to the FastComtec acquisition board that waits a pre-defined time (extraction delay) for the packet of neutral potassium atoms to arrive at the collision centre, located in the middle point of extraction region of the TOF spectrometer. Though, the acquisition board sends a start trigger to the Jordan generator, which applies a –400V pulse to the extraction region. The ions are then extracted and after a certain time interval arrive at the channeltron detector. For each ion reaching the detector, a negative voltage pulse is produced. This signal is amplified by the Ortec VT120 and sent to the stop input of the acquisition board that records its flight time in the respective time bin. After a certain time interval, all the ions have arrived at the detector and the acquisition sweep ends. The acquisition board goes into a standby mode and waits for the HP 214B to send the next trigger signal that will initiate a new acquisition cycle. This process is repeated until we obtain a reasonable TOF mass spectrum with good signal-to-noise ratio.

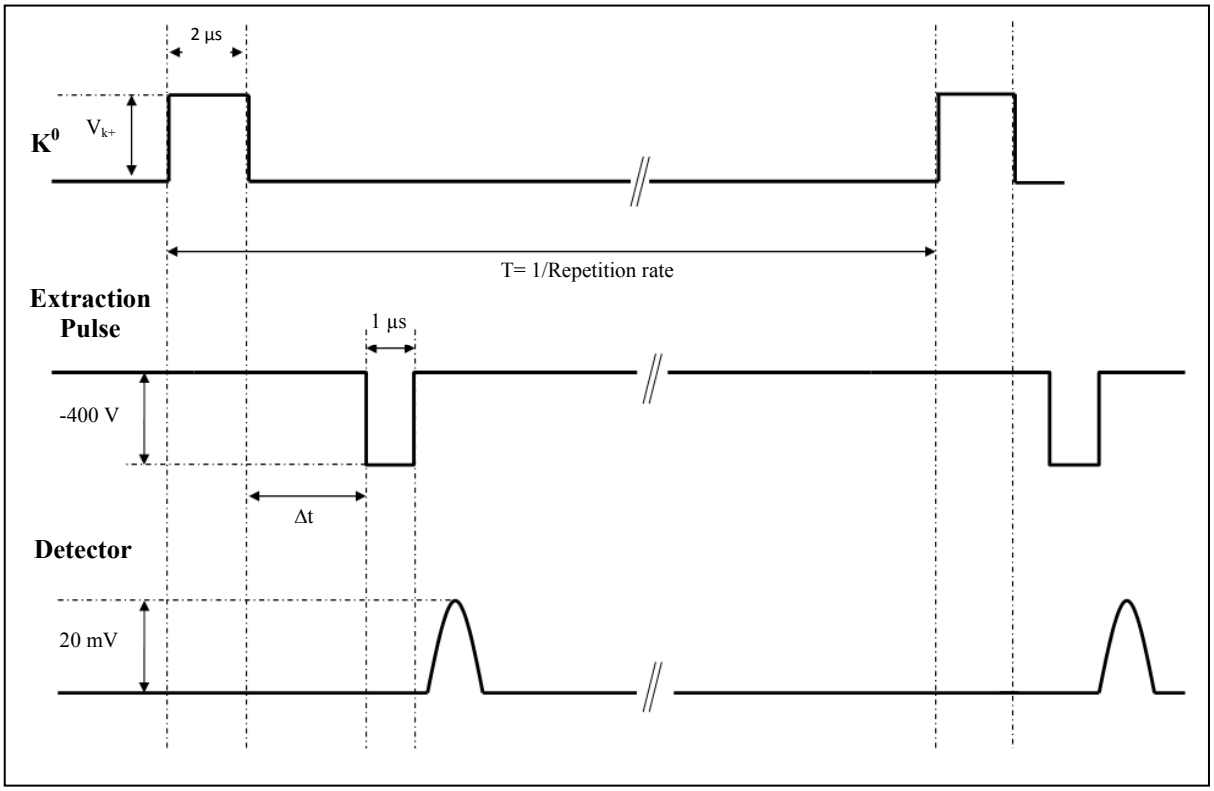

Figure 3.29 - Acquisition system time diagram

3.5.6.1 Pulsed operation

The pulsed operation mode as described previously consists in using not only a pulsed TOF spectrometer but also using a pulsed neutral potassium beam. If the potassium beam was set to be continuously produced, the peaks in the mass spectra would appear with a notorious shoulder to the right (especially the low masses), due to the contribution of the ions that are being created during the extraction process. This occurrence makes it difficult to set a proper TOF start instant and will consequently affect the mass resolution of the spectra obtained. To reduce this effect, a pulse was also applied to the neutral potassium beam, being the TOF extraction performed after all the neutrals have reached the collision centre. In Figure 3.30 we plot a spectra obtained using the pulsed mode operation over the continuous mode operation.

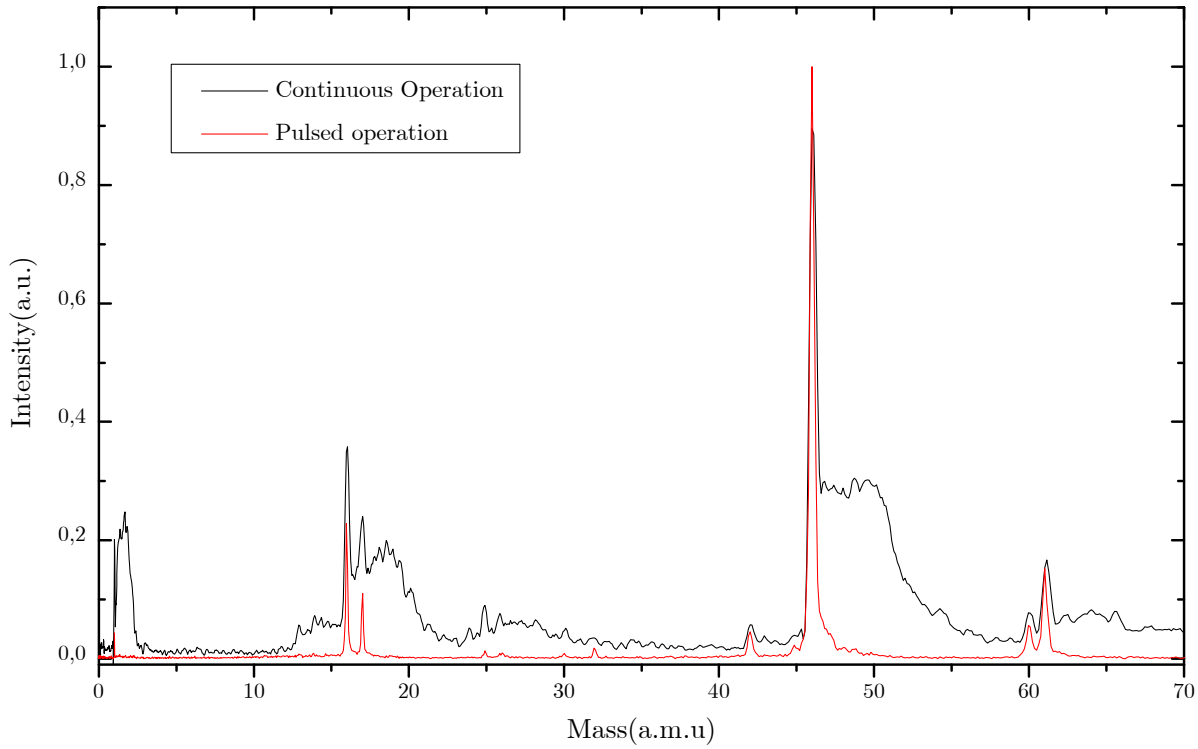

Figure 3.30 - Nitromethane TOF mass spectra in pulsed and continuous operation modes

3.5.6.2 Extraction Delay

In order to operate the system in the pulsed mode at any given collision energy, it was necessary to experimentally determine the correct delays between the neutral beam formation and the fragments extraction (Table 3.7).

Table 3.7 - Extraction delays

Collision Energy (μs)	Delay (μs)
30	35.3
70	22.6
100	18.5

The method used to determine the best delays was to acquire nitromethane spectra at different collision delays for several collision energies. The obtained spectra are then compared and the delay that leads to the best TOF spectrum is determined.

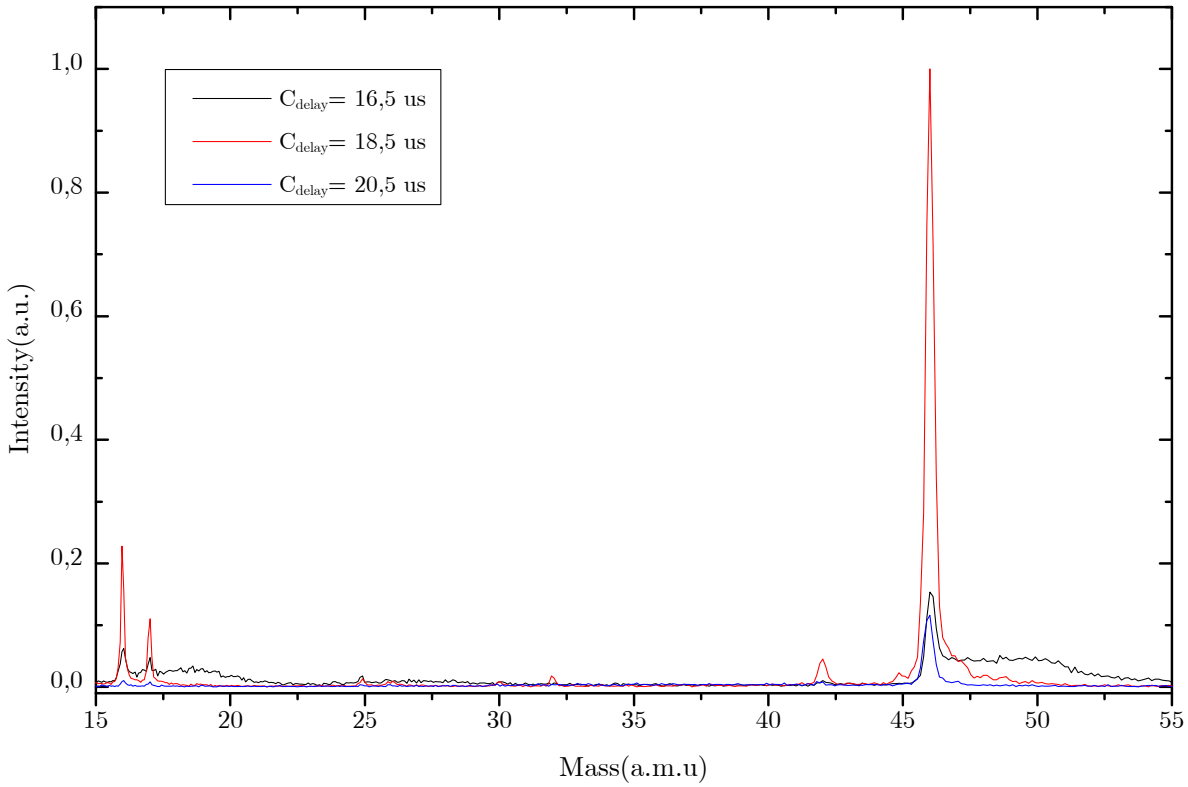

Figure 3.31 - Nitromethane partial spectra with different collision delays for a collision energy of 100 eV

From Figure 3.31 is possible to conclude that for a delay of 16.5µs the anions' extraction occurs too early. The small shoulder appearing to the right of the peaks, suggests that the extraction is taking place during the arrival of the neutral potassium atoms.

When looking at the spectrum with a extraction delay of 20.5µs, is possible to infer that the extraction is occurring too late and the peaks' intensity has already started to decreased (when compared with the previous spectrum taken with a delay of 18.5µs). This suggests that some the fragments have already left the collision region, probably because of their kinetic energy release distributions.

For a delay of 18.5µs the peaks in the spectrum seem to have no shoulders and the peak intensity has reached its maximum value. As a result, is possible to confirm that the correct delay for an energy collision of 100 eV is 18.5µs.

3.6 Vacuum System

The schematics of the vacuum system associated with this experimental setup is presented in Figure 3.32 and essentially comprises two chambers, a set of vacuum pumps and vacuum gauges and control units.

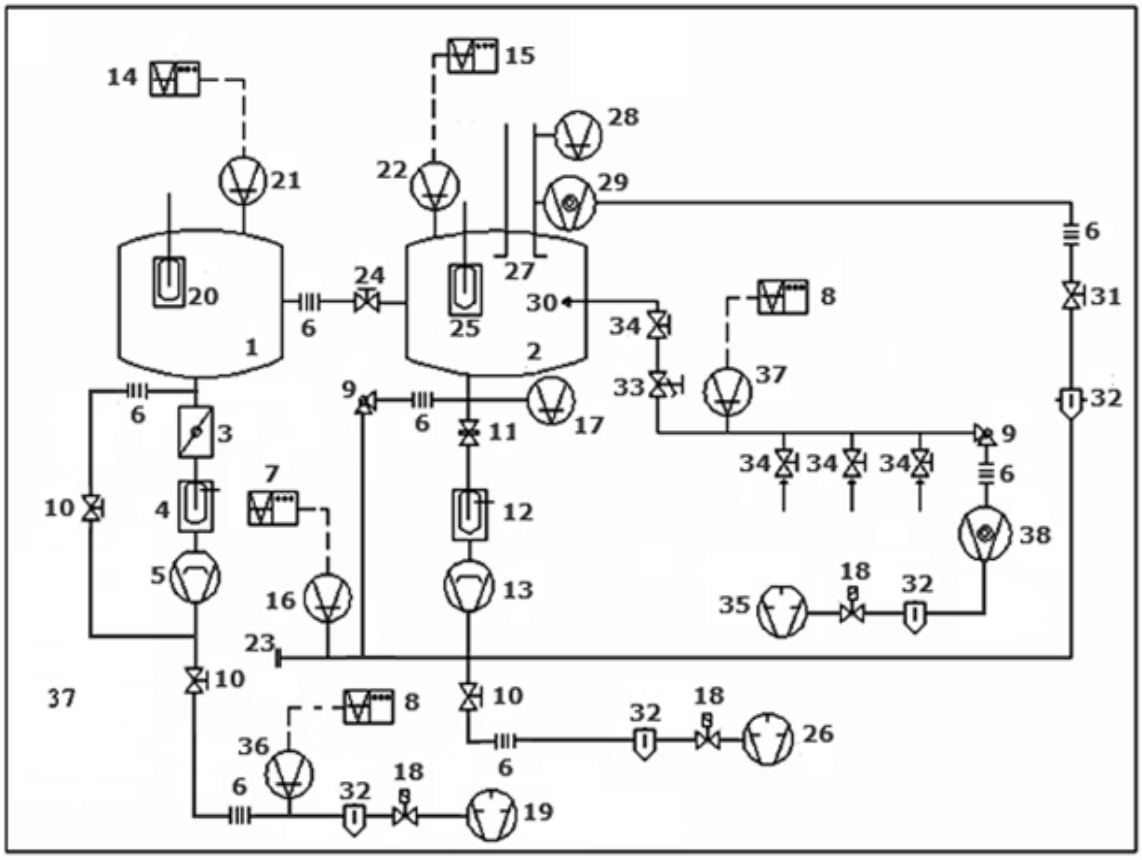

Figure 3.32 - Vacuum system schematics

1. Potassium chamber
2. Collision chamber
3. Butterfly valve
4. Liquid *nitrogen trap*
5. Edwards E06 diffusion pump
6. Bellow
7. Boc Edwards TIC instrument controller
8. Combivac-CM-31 instrument controller
9. 90º Vacuum alve
10. Speedivac Edwards manual valve
11. Gate valve Airco Temescal R-3
12. Liquid nitrogen trap
13. Varian NRC 0184 diffusion pump
14. Edwards Penning 505 instrument controller
15. Edwards Penning 505 instrument controller
16. Pirani Boc Edwards APG-NW-16 vacuum gauge
17. Penning Balzers IKR250 vacuum gauge
18. Edwards Speedivac solenoid valve
19. Two-stage E2M18 Edwards rotary pump

20. Liquid nitrogen trap
21. Penning Edwards CP-25-EK vacuum gauge
22. Penning Edwards CP-25-EK vacuum gaguge
23. Blank connecting flange
24. Inter-chambers manual gate valve
25. Liquid nitrogen trap
26. Two-stage E2M18 Edwards rotary pump.
27. TOF Mass spectrometer
28. Penning Balzers IKR20 vacuum gauge
29. Varian turbo-V60 high-vacuum pump
30. Swagelok Male Elbow
31. Leybold AG manual valve
32. Molecular sieve trap
33. Precision leak valve – sapphire valve.
34. Swagelock manual valves
35. Two-stage D8B Leybold rotary pump
36. Pirani Leybold TR211 vacuum gauge
37. Pirani Leybold TR211 vacuum gauge
38. Leybold turbovac 150 high-vacuum pump

The Potassium chamber (1) contains the potassium oven, the charge exchange oven, the ion source and a pair of deflecting plates (described in detail in chapter 3.2). The vacuum conditions are guaranteed by a diffusion pump (5), with a pumping speed of 1300 l/s with an ultimate pressure of 5×10^{-7}mbar, and two liquid nitrogen traps, one placed between the pump and the chamber and the other placed inside the chamber itself. The diffusion pump backup is guaranteed by a two-stage rotary pump (19), with a pumping speed of 6 l/s and an ultimate pressure around 1×10^{-2} mbar. A molecular sieve trap is placed between the rotary and the diffusion pumps to prevent the chamber contamination with rotary oil vapours.

Inside the collision chamber (2) are assembled a Langmuir-Taylor detector, both potassium and biomolecules beam collimation slits, the baking system, the biomolecules' oven and the TOF spectrometer (described in chapters 3.3 and 3.4). The vacuum is guaranteed by a diffusion pump (13), with a pumping speed of 1550 l/s and an ultimate pressure of 5×10^{-7}mbar, and two liquid nitrogen traps, one placed between the pump and the chamber and the other placed inside the chamber itself. The TOF system is pumped differentially by a turbomolecular pump placed near the channeltron detector. Both the diffusion and turbo pumps are backed by a two-stage rotary pump (26), with a pumping speed of 6 l/s and an ultimate pressure of 1×10^{-2} mbar. A molecular sieve trap is placed after the rotary pump to prevent the chamber and TOF spectrometer contamination with rotary oil vapours.

The chambers 1 and 2, the potassium and the collision chamber, respectively, are connected through a gate valve (24) that allows an independent chamber operation. Hence, it is possible to operate one of them at atmospheric pressures and keep the other in high-vacuum conditions. This is especially important when is necessary to proceed with the replacement of the potassium or when a chamber cleaning is needed.

The liquid sample system is pumped differentially by a two-stage rotary pump (35), with a pumping speed of 2.8 l/s. A molecular sieve trap is placed immediately after this rotary pump to prevent the sample contamination with rotary oil vapours.

The whole system is protected against electric and water failures through a security system.

Chapter 4 Nitromethane

4.1 Introduction

Nitromethane, CH_3NO_2 (Figure 4.1), has been experimentally [27-38] and theoretically [39-42] extensively studied mainly because it can be regarded as (1) an atmospheric relevant compound in the chemistry of the earth's troposphere and stratosphere, (2) an nitro-organic molecule with a significant industrial use for explosives and propellants, (3) a prototypical molecule to be used as a benchmark system as far as its energetics and structural properties for high-level computational treatments are concerned, and (4) as a polar molecule with a considerable static dipole moment allowing dipole-bound anion states [36] by capture of an extra electron.

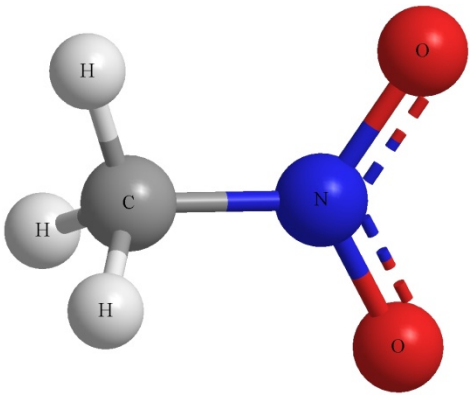

Figure 4.1 - Three-dimensional schematic representation of nitromethane molecule

Stockdale *et al*. [36] have investigated by electron impact and collisions with Ar and Kr atoms in excited Rydberg states (see more recently Suess *et al*. [37]), the production of negative ions from nitromethane; parent ion formation through charge transfer reactions of Rydberg states was realized to happen by the acceptor molecule only due to the stabilization effect induced by the presence of the cation, formed upon the transfer of a 'bound' electron. Compton and co-workers [31] have studied the collisional ionisation mechanism between alkali atoms (Na, K, Cs) and some methane derivatives (including CH_3NO_2), from threshold up to ~ 40 eV. Electron affinity values for stable negative ions were obtained from the energy threshold for the ion-pair production reactions.

The spectroscopy and dynamics of nitromethane and its anionic states have been investigated by optical and electron scattering methods by Walker and Palmer [38]. Modeli and Venuti [34] have obtained the resonance energies of CH_3NO_2 by means of electron transmission spectroscopy and dissociative electron attachment in an electron energy range from 0 – 6 eV. Dissociative electron

attachment (DEA) to nitromethane has been investigated in the electron energy range 0 – 10 eV by high energy resolution (140 meV) [35], with 7 fragment anions reported. Recently, Alizadeh *et al*. [28] have revisited the DEA measurements by making use of a high mass-resolution sector field instrument. Anion efficiency curves for 16 negatively charged fragments were obtained in the electron energy range from 0 to 16 eV, with an energy resolution of ~ 1 eV.

Dipole- and valence-bound anion states have been reported using negative ion photoelectron spectroscopy (see also ref. [32] for photoelectron imaging), Rydberg charge exchange and field detachment techniques [30] of the bare and argon-solvated anions [33]; these studies have shown that dipole-bound and valence forms of nitromethane are interconnected with no appreciable potential barrier (~ 12 meV) relative to the zero-point vibrational motion. Adamowicz [39] has performed *ab initio* coupled cluster studies to dipole-bound anionic states of nitromethane and obtained an electron affinity of ~ 3 meV, too low in respect to the experimental value of Compton *et al*. [30]. Liu *et al*. [43] have addressed dipole-bound anions into long-lived valence-bound character by charge transfer in collisions between dipole-bound CH_3CN^- and CH_3NO_2 in Penning ion trap experiments.

Ion-pair formation in collisions of potassium atoms with nitromethane molecules have been reported including double-differential cross sections, obtained as a function of the scattered angle and the post-collision energy [27]. Moreover, the time-of-flight relative total partial cross sections measurements were capable of detecting three negative ions, O^-, NO_2^- and $CH_3NO_2^-$ only. Steric asymmetry studies in electron transfer from potassium atoms to oriented nitromethane molecules have been performed by Brooks and co-workers [29], showing no steric evidence for methyl-end attack, which suggests no participation of a dipole-bound state in the formation of $CH_3NO_2^-$ near threshold.

4.2 Experimental Conditions

The nitromethane negative ion formation, arising from the collision with neutral potassium atoms, was probed with a TOF mass spectrometer (described in section 3.4.3) at three collision energies defined within a laboratory framework: 30, 70 and 100 eV. It is however important to point out that, in view of momentum conservation, the energies expressed in the laboratory framework are not entirely "available" to the charge exchange process. As such, when dealing with a binary collision, where the target molecule is assumed to be motionless, the "available" energy is equivalent to the collision energy in the centre-of-mass framework, which can be obtained from the Lab collision energies as follows

$$E_{CM} = \frac{m_t}{m_t + m_p} E_{Lab(effective)} \ , \tag{4.1}$$

where m_t is the mass of the target molecule and m_p of the projectile.

The collision energy in the laboratory framework (E_{Lab}) is defined as the voltage applied to the potassium ion source V_k. However there is a shift between the nominal voltage applied to the ion source and the actual energy ($E_{Lab(effective)}$) acquired by potassium atoms, as estimated in section 3.2.6.4 , which is given by:

$$E_{Lab(effetcive)} = 0.889 \times E_{Lab} \tag{4.2}$$

Considering equations (4.1) and (4.2) is possible to estimate that the "available" energy for the charge exchange process in the collision $K + CH_3NO_2$ is 16.3±0.5 eV for E_{lab}=30 eV , 38.0±0.5 eV for E_{lab}=70 eV and 54.2±0.5 eV for E_{lab}=100 eV.

The experimental parameters used in the collection of the nitromethane spectra, for each collision energy defined in the Lab framework, are resumed in the following table:

Table 4.1 - Experimental acquisitions parameters

Experimental Parameters	30 eV	70 eV	100 eV
K pressure (mbar)	5.58×10^{-7}	5.82×10^{-7}	7.47×10^{-7}
K oven temperature (K)	423	423	423
CE oven temperature (K)	443	443	443
Ion source current (A)	2.05	2.05	2.05
Ion source pulse width (μs)	2	2	2
Neutral Potassium beam (pA)	3.48	34.75	87.00
Collision chamber base pressure (mbar)	1.48×10^{-7}	1.48×10^{-7}	1.52×10^{-7}
Collision chamber work pressure (mbar)	1.21×10^{-5}	1.67×10^{-5}	1.45×10^{-5}
Biomolecules Oven temperature (K)	302	302	302
TOF Extracting voltage (V)	–300	–300	–300
TOF Acceleration voltage (V)	–3500	–3500	–3500
TOF Einzel Lens Voltage (V)	–1500	–1500	–1500
TOF Extracting Pulse width (μs)	1	1	1
Total Acquisition time (s)	16965	10701	6168
Acquisition delay (μs)	35.25	22.6	18.5
Acquisition bin width (ns)	8	8	8
Acquisition bin range (channels)	2048	2048	2048
Acquisition repetition rate (Hz)	11.11	11.11	22.22

After each TOF mass spectra collection, ion counts are normalized according to the following expression:

$$\frac{C}{t.f.P.I} \tag{4.3}$$

where C is defined as the ion count (per channel), t the total acquisition time, f the acquisition rate, P the acquisition pressure and I the neutral potassium beam intensity (typically in pA). This calibration will allow the comparison between spectra acquired at different collision energies.

4.3 Results and Discussion

In the present experiment we re-investigated the negative ion formation in potassium-nitromethane collisions at different collision energies and made use of deuterated nitromethane to conclude that the previous m/q=17 assignment to O^- delayed fragment is unambiguously due to OH^- formation [44].

Figure 4.3 shows the TOF mass spectra, at three collision energies, for the anions formed in the collision of K + CH_3NO_2. In contrast with previous work performed in a similar experimental set-up [27] where three anions were identified (Figure 4.2), we were able to identify nine. The relative cross section of the fragments was obtained by integrating the respective mass spectrum at each collision energy (Table 4.2).

The negative ions resulting from the electron transfer in the collision of potassium atoms with nitromethane molecules yield mainly the parent ion $CH_3NO_2^-$, the dehydrogenated parent anion $CH_2NO_2^-$, NO_2^-, NCO^-, OH^-, O^-, H^- and other minor species. The spectra captured at 30, 70 and 100 eV, always show that the most intense fragment is NO_2^-, and the anions 17, 26, 30, 42 and 60 a.m.u have less than 20% of its yield. While NO_2^- and O^- may result from single bond cleavage in the unimolecular decomposition of the transient negative ion, formation of NCO^-, OH^- and CN^- may result from more complex reactions involving multi-bond cleavage and internal energy rearrangement.

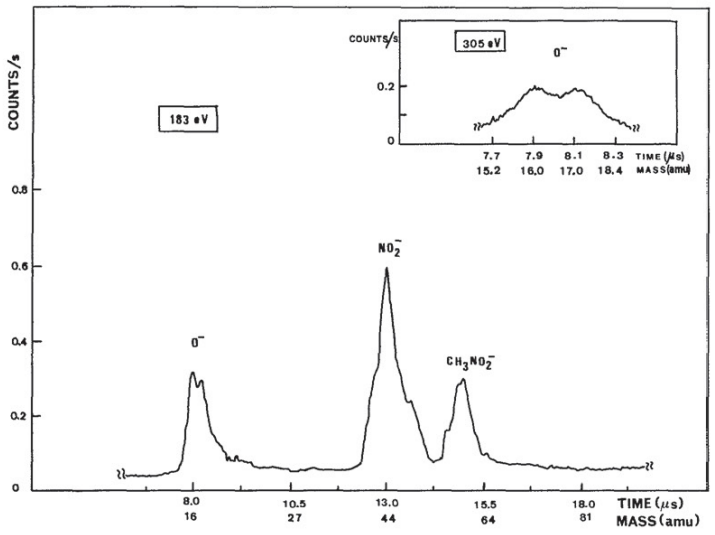

Figure 4.2 - Nitromethane TOF anion spectrum at a collision energy of 183 eV [27].

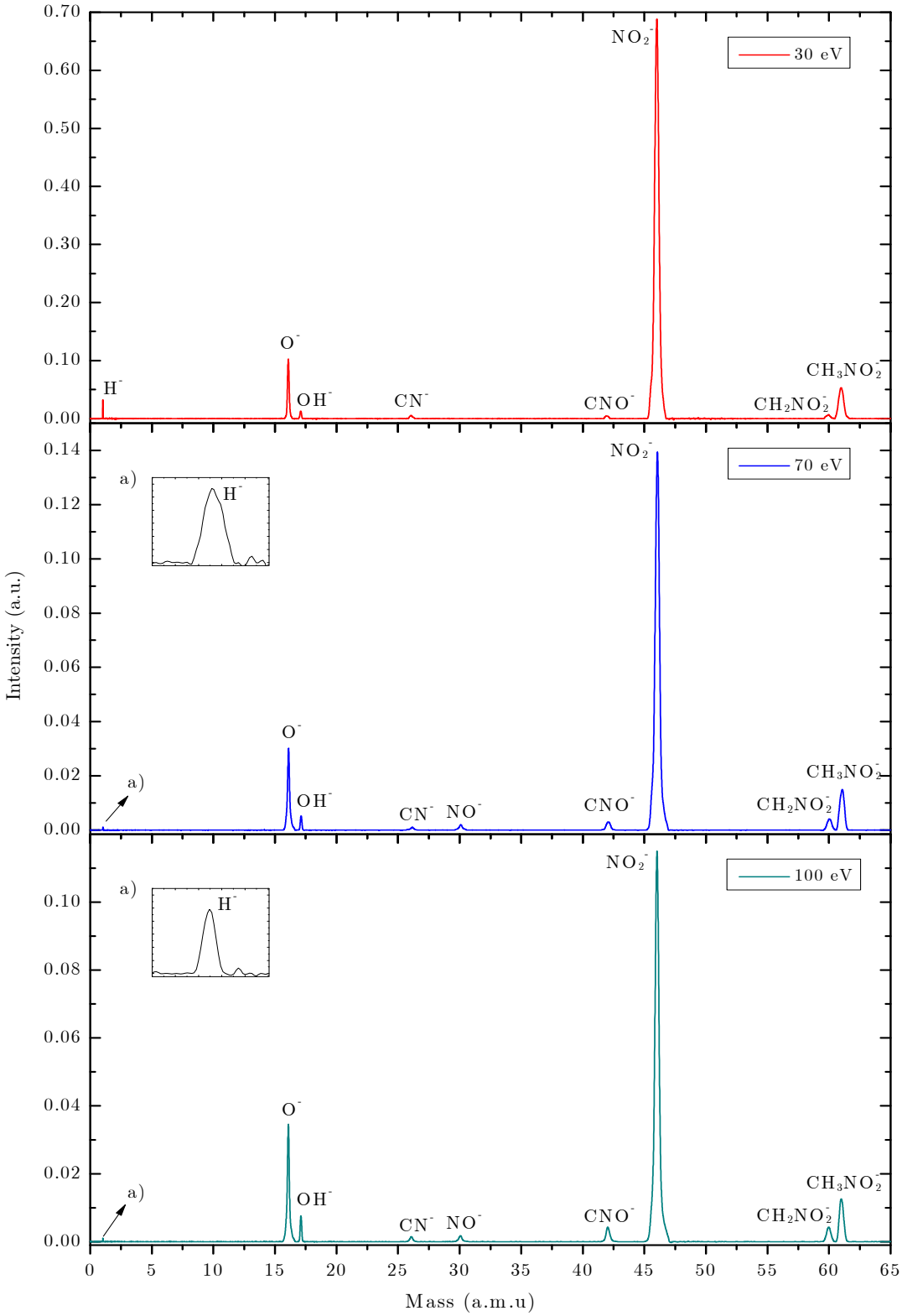

Figure 4.3 - Nitromethane TOF anion spectra at three collision energies

Table 4.2 - Nitromethane negative ions assignment and respective relative partial cross sections at several collision energies

		30 eV	70 eV	100 eV
Anion	Mass (a.m.u)	Partial Cross Section (a.u.)	Partial Cross Section (a.u.)	Partial Cross Section (a.u.)
H^-	1	0.11	0.0061	0.0034
O^-	16	0.5	0.198	0.227
OH^-	17	0.06	0.0226	0.0311
CN^-	26	0.036	0.0083	0.0099
NO^-	30	0	0.0150	0.0130
NCO^-	42	0.026	0.0228	0.0279
NO_2^-	46	5	1.06	0.84
$CH_2NO_2^-$	60	0.038	0.0265	0.0264
$CH_3NO_2^-$	61	0.39	0.099	0.0769

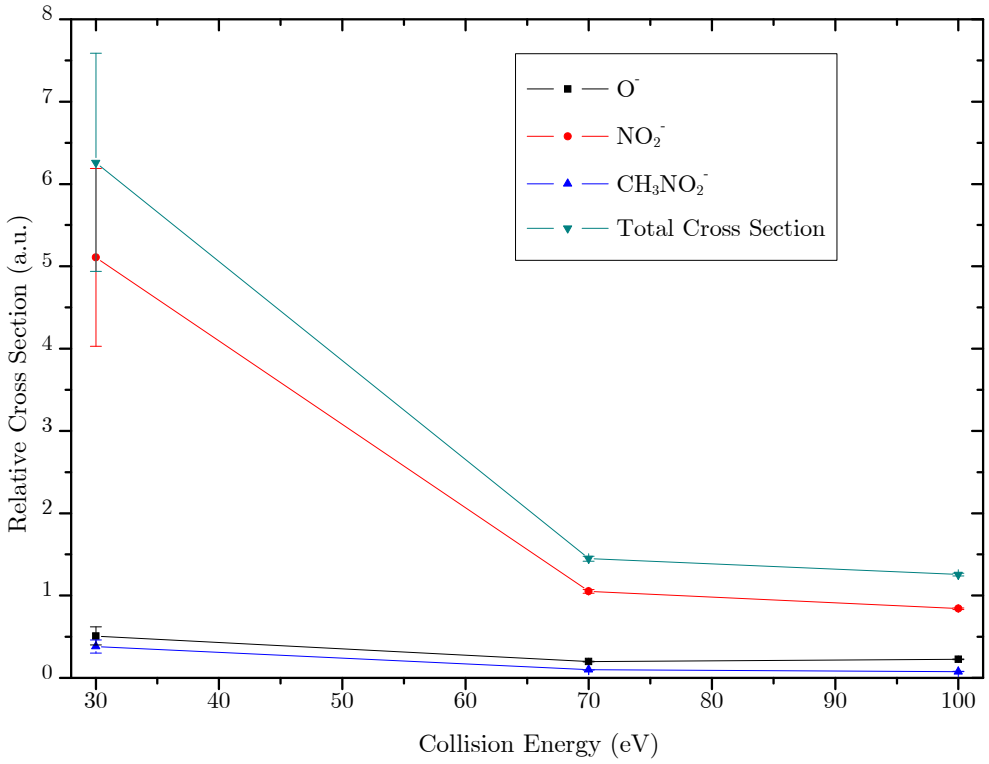

Figure 4.4 - Nitromethane Partial Cross Section

From both Table 4.2 and Figure 4.4 is possible to infer that the majority of the fragmentation channels appear to have little changes in their cross sectional values when comparing results taken at collision energies of 100 and 70 eV. Nevertheless, when the collision occurs at lower energies (30 eV) the relative cross section of the negative ions tends to increase, especially for NO_2^-, showing a rising of a factor of 6. On the other hand, the OH^- and NCO^- cross sections intensities are unchanged for the three collision energies. It is also important to note the unique behaviour shown by the NO^- anion that is absent when the collision energy is decreased to 30 eV. At this collision energy, in the CM we are left with an available energy of ~ 9 eV. This is closely related to the cross section value obtained in DEA experiments [28] showing one of the lowest values (1.5×10^{-25} m^2) at this energy. We should point out that the absence of such anion in our experiments may also result from the fact that due to its low ionic yield it may be however, hidden in the background signal, making its detection difficult. Furthermore, when comparing this partial cross section results with those from *Lobo et al*. [27], it is possible to perceive that a similar behaviour exists, i.e. when the collision is reduced from 100 eV to 30 eV the production of the negative ions NO_2^- ,$CH_3NO_2^-$ and O^- increases considerably.

In atom-molecule collisions leading to ion-pair formation, the target molecule (electron acceptor) is expected to react easily if it has anionic states that match the instantaneous kinetic energy of the incoming 'bound' electron. The nitromethane anionic states have been found through electron impact to lie at 0.72, 2.4, 4.0, 5.6, 6.1 and 8.7 eV, which, with the exception of the 2.4 eV, have shown to be dissociative in character. The spectroscopy of such states is normally discussed in the C_{2v} symmetry due to the fact that the electron density is concentrated at the NO_2 end. As such, from electron impact studies and from previous work performed in potassium/nitromethane collisions, it was possible to identify that the most relevant low lying ionic states are a repulsive σ^* state of $^2A_1$ symmetry and two π^* bound states of $^2B_1$ character.

→ $CH_3NO_2^-$

The parent ion detection has been already reported in collisions of nitromethane with highly excited Rydberg atoms. It has been suggested [36] that upon electron transfer, the nitromethane molecule goes from the neutral ground state to a vibrational excited configuration of the $^2B_1$ anionic state. Once in this state, if the anion is allowed to relax into a vibrational state below the ground state of the neutral, a long lived parent ion is created. The stabilization of the nitromethane anion is induced by the positive core formed after the electron transfer in the Rydberg experiments. On the other hand, if no stabilization agent is present, as is the case of electron attachment experiments, two competitive processes can occur from the excited configuration of the $^2B_1$ anionic state. The first is autodetachment, which could occur if the molecule is kept in an anionic vibrational excited state above

the ground state of the neutral. The second is dissociation, which can happen if a curve crossing occurs between the $^2B_1$ state and a dissociative state (which has been suggested by *Walker et al*. [38] to be a $^2A_1(\sigma^*)$ state), as observed in Figure 4.5.

In the current experiments the parent anion was also observed, which is in good agreement with the fact that after the charge exchange there is a positive potassium core that can allow the relaxation of $CH_3NO_2^{\#-}$ into a geometry where autodettachment and dissociative channels may be blocked. However, it is important to note that the collision kinetic energy can have some relevance in the efficiency of the stabilization performed by the potassium cation. From the relative cross section results, presented above, is possible to perceive that the negative parent ion formation decreases for higher collision energies. This can suggest that the potassium spends less time near the negative nitromethane molecule, therefore it has less capability of inducing the relaxation needed for the nitromethane anion to reach a more stable configuration.

Another important property of the nitromethane molecule is its high dipole-moment (3.46 D), which allows supporting a stable dipole-bound state (DBS). As such, when the covalent PES cross the ionic PES, a weakly bound electron (e.g. in a Rydberg state) can be transferred to form a dipole-bound anion that may serve as a "doorway" to valence states [30]. In fact, recent calculations for electron attachment to nitromethane [42] have shown that, on a mass spectrometric timescale, the dipole serves as an efficient doorway to a valence state, which is quickly populated and may be stabilized by collisions with a third body partner.

However, studies made on the steric asymmetry in electron transfer between potassium atoms and oriented nitromethane molecules [29] have shown that there is no relevant increase in the production of $CH_3NO_2^-$ at threshold when the potassium "attacks" the molecule at the methyl end. This means, that even though the nitromethane molecule has the capability to form a dipole-bound anion, in collisions with potassium atoms the dipole-bound states do not play a relevant role in the formation of the parent anion.

→ NO_2^-

This is the dominant fragment for all of the collision energies probed. The appearance energy for this fragmentation channel is 0.37 eV, calculated from the bond dissociation energy and the electron affinity ($D(CH_3\text{-}NO_2)$ = 2.64 eV, $EA(NO_2)$ = 2.27 eV) [28, 35]. Thus, from the energetic point of view, the formation of this fragment is allowed for all the collision energies studied in this thesis. However, there is a significant increase in the NO_2^- yield at lower collision energies (see Figure 4.4). To better understand the processes involved in this fragmentation, one can assume that when the $K+CH_3NO_2$ potential energy surfaces of the ionic and covalent states cross and an electron jump occurs, a Franck-Condon transition happens from the neutral to the anionic states of the target

molecule (Figure 4.5). The analysis of such transitions can be useful to qualitatively account for the fragmentation cross section evolution with the collision energy. In Figure 4.5 the reaction coordinate is the C-N distance that includes different anion geometries at small distances. Dashed portions of the anion curves indicate regions where the anion is unstable with respect to the neutral molecule plus an electron.

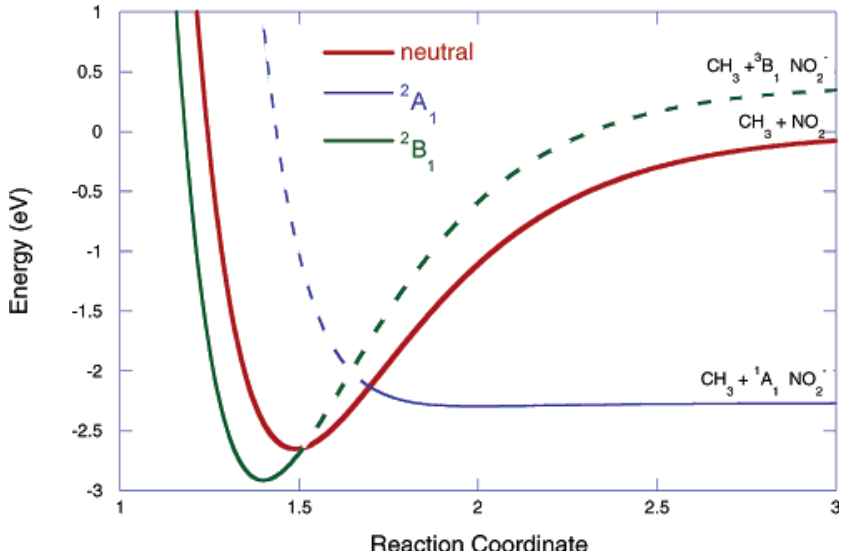

Figure 4.5 - Schematic potential energy curves taken from [45] for neutral ground-state CH_3NO_2 and the two lowest-lying anion states, $^2B_1(\pi^*)$, and $^2A_1(\sigma^*)$.

In DEA experiments, NO_2^- is formed by the accommodation of the extra (free) electron into the LUMO of $\pi^*(b_1)$ character of the nitro group, correlating with the $^2B_1$ state of $CH_3NO_2^-$. A dissociative process can occur following the curve crossing of this $^2B_1(\pi^*)$ state with the anionic state $^2A_1(\sigma^*)$, leading to NO_2^- fragment formation. As mentioned above regarding the $CH_3NO_2^-$ formation, the transition from the neutral to the anionic state $^2B_1(\pi^*)$ can originate both the parent ion and the dissociation into the NO_2^- fragment. It is interesting to note that the proportion between the formation of NO_2^- and $CH_3NO_2^-$ is ~11 for both 100 eV and 70 eV collisions. This may suggest, in fact, that both of the fragmentation channels are originated at these energies from the same anionic state. However, for collisions at 30 eV the proportion between these fragments is ~13, which could be in principle associated with the considerable increase in the relative cross section of the NO_2^- fragment.

Walker et al. [38] have observed, in electron impact experiments, that no fragmentation results from the direct transition from the neutral state to this anionic state $^2A_1(\sigma^*)$. It seems that, in free electron experiments, the dominant process following the transition to this state is autodetachment, which happens when the anionic state is within the electronic continuum of the neutral configuration.

However, from energy loss measurements in potassium-nitromethane collisions *Lobo et al.* [27] observed that the production of NO_2^- fragment was mainly due to the direct transition from the neutral to the anionic state $^2A_1(\sigma^*)$ with a vertical electron affinity of -2.16 ± 0.17 eV. Moreover, the results reported in [27] regarding NO_2^- relative cross section are in close agreement with our results. In both experiments is possible to observe that NO_2^- is always the most abundant fragment and that its cross section increases substantially for lower collision energies (30 eV). It has been suggested [27] that this cross section increase can be justified by the molecular behaviour of the nitromethane during the collision. As mentioned in Chapter 2 , in alkali-molecule collisions the system is allowed to change between the ionic and covalent states at specific internuclear projectile-target distances, the crossing radius R_c. In the two particle approximation R_c is passed twice, one when the particles approach and another when they go apart. As such, for low collision velocities, an early crossing (ionic path) with a repulsive ionic surface leads to bond stretching (C-N) resulting in an increase of the electron affinity and consequently to an increased probability of passing the second crossing adiabatically, meaning that the system is more likely to remain along an ionic surface [27]. Furthermore, *Lobo et al.* have proposed that, at lower collision velocities, the C-N bond stretching along the "ionic" path will not only be responsible for an increase negative ion formation but also a rise in the dissociative channel yielding preferentially NO_2^-. In this case the C-N bond stretch is such that the neutral state is no longer available and therefore autodetachment ceases. On the other hand, if the electron jump occurs only at the second crossing ("covalent" path), the anion $CH_3NO_2^{\#-}$ is formed in the electronic continuum of the neutral which facilitates a rapid autodetachment [27]. Though, electronic transitions at lower velocities to the repulsive anionic state $^2A_1(\sigma^*)$ along the "ionic" trajectory will be the solo responsible for the production of NO_2^-. The same transitions along the "covalent" path will be responsible for the production of free electrons (not detected in this experiment) [27]. At higher collision velocities there is not enough collision time for bond-stretching along the "ionic" path and as consequence autodetachment becomes dominant. This picture is coherent with the decrease of the relative cross section of NO_2^- formation for higher collisions energies as observed in Figure 4.4.

→ **O^- and OH^-**

Earlier time-of-flight alkali beam experiments have reported two signals assigned to O^-, 16 and 17 a.m.u, the latter attributed to a delayed O^- relative to the former and attributed to internal isomerisation of the $CH_3NO_2^-$ to CH_3ONO^- prior to fragmentation [27]. Recently, Arenas *et al*. [40] have performed multiconfigurational second-order perturbation studies on the decomposition of the nitromethane radical anion and have shown no evidence of an isomerisation channel leading to the initial formation of the methylnitrite anion, CH_3ONO^-. We have therefore re-investigated fragment

anions 16 and 17 a.m.u by deuterating nitromethane. Figure 4.6 shows the negative ion TOF mass spectra of potassium with nitromethane–d_3 at 100 eV collision energy, where fragmentation patterns resulting from the deuterium substitution can be observed. There is clearly evidence of $D^-$and OD^- formation as well as the parent anion and its dehydrogenated (deuterated) anions, allowing us to conclude that the fragment anion at 17 a.m.u in K + CH_3NO_2 collisions is due to OH^- formation.

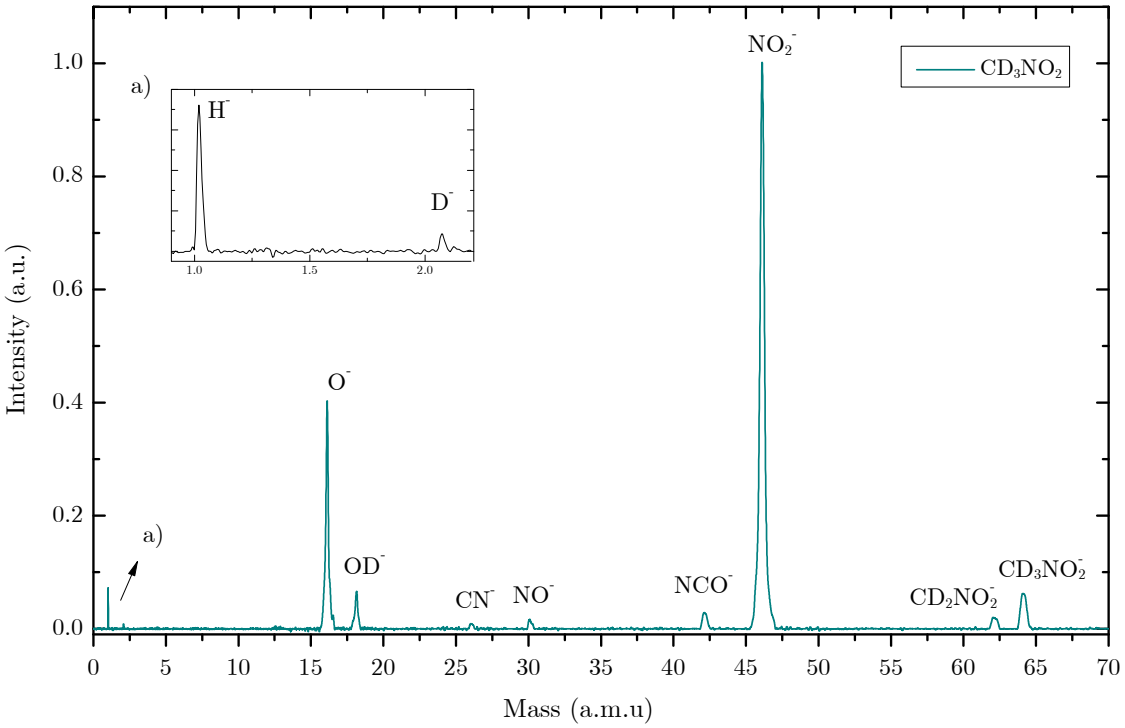

Figure 4.6 - Negative ion TOF mass spectrum of K + CD_3NO_2 at 100 eV collision energy

O^- has been reported as the major ionic product at higher incident electron energies, 5.6 and 6.1 eV [38], the former thermal and the latter energetic with ~ 1 eV translational energy. However, Walker and Fluendy were not able to distinguish whether the different O^- ions were originally or not from different exit channels on a single surface or from two different surfaces. They could only conclude that O^- formation results from an excited anion or anions states.

Dissociative electron attachment to nitromethane reported O^- formation via two possible reaction channels [35]:

$$e + CH_3NO_2 \rightarrow (CH_3NO_2)^{\#-} \rightarrow CH_3NO + O^- \quad (4.4)$$

$$e + CH_3NO_2 \rightarrow CH_3 + NO + O^- \quad (4.5)$$

where at threshold reaction (4.4) is operative at 2.71 eV (against a measured appearance energy of 3.3±0.2 eV) and reaction (4.5) having a calculated threshold (using EA(O)=1.461 eV, $\Delta_f H_g^o(CH_3NO_2)$= –81.0±0.1 kJ/mol, $\Delta_f H_g^o(CH_3)$=146±1 kJ/mol, $\Delta_f H_g^o$(O)=249.0±0.1 kJ/mol) at 4.41 eV [35].

The recent DEA experiments of Alizadeh *et al*. [28], reported a O^- strong signal at 6 eV and other high energy resonances at 9 and 10.5 eV, which have been explained in terms of core-excited resonances and/or Rydberg excitation, respectively. Therefore, the K^+ energy loss profiles of *Lobo et al.* [27] show above 61 eV collision energy broad features at ~ 6.5 and 8.5 eV and extending up to ~ 13 eV for higher collision energies (183 eV). This may be indicative of the resonant character of the accessible channel leading to O^- formation.

OH^- formation is shown at a resonant electron energy of ~ 4.0 eV and was explained to happen upon electron capture which distorts the molecular anion about the HCNO dihedral angle narrowing the OH distance [38]. A tentative assignment was proposed for the initial population of $^2B_1$ state as the precursor. However, Sailer *et al*. [35] have shown that OH^- formation also occurs via two low electron energy resonances at ~ 0 and 1.7 eV. They have argued, based on the gas pressure in the reaction chamber and absence of contaminants considerations that the lowest resonance (~ 0 eV) is due to DEA to vibrationally excited (hot bands) nitromethane molecules.

→ $CH_2NO_2^-$

The dehydrogenated closed shell anion $CH_2NO_2^-$ has been proposed to be formed via the following endothermic reaction in dissociative electron attachment experiments [28]:

$$e + CH_3NO_2 \rightarrow (CH_3NO_2)^{\#-} \rightarrow CH_2NO_2^- + H \qquad (4.6)$$

with a threshold at 1.95 eV, obtained through the bond energy D(CH_2NO_2–H)=4.40 eV and the electron affinity EA(CH_2NO_2)=2.45 eV. Alizadeh *et al*. [28] reported the lowest resonant feature for $CH_2NO_2^-$ formation at ~ 0.5 eV, which means that the nitromethane dehydrogenated closed shell anion is energetically not allowed at this energy. The electron attachment can only proceed through vibrationally excited states (hot bands) even though the number density of those modest hot molecules may be low electron attachment cross sections for excited states are often orders of magnitude higher than those in the ground state.

Formation of $CH_2NO_2^-$ and $CH_3NO_2^-$ ions is observed in the proportion of ~1:10, ~1:4 and ~1:3 for the three collision energies studied, 30, 70 and 100 eV, respectively. This behaviour at different energies can be justified considering that the parent anion and the dehydrogenated closed

shell anion $CH_2NO_2^-$ rise from different anionic states. On the other hand, if both species are formed through the same anionic state, the formation probability for each individual species is collision energy dependent. One can suggest that for low collision energies the stabilization effect in the C-H coordinate provided by the K^+ is more effective, enhancing the formation of the parent ion.

The dehydrogenated parent anion formation can also be seen from an interesting point of view regarding the strong coupling between the dipole bound state and the temporary anion state related to the occupation of valence orbitals, that can actually play a significant role in electron capture by nitromethane molecules [29, 44-45].

→ H^-

The spectra in Figure 4.3 show the recorded H^- signal obtained by subtracting the background signal (with a pressure of 4×10^{-5} Pa) from the sample signal (at a working pressure of 10^{-4} Pa). The relative partial cross section for H^- formation increases around two orders of magnitude, when going from a collision energy of 100 eV to 30 eV.

The DEA reaction leading to H^- formation has been identified as [28]:

$$e + CH_3NO_2 \rightarrow (CH_3NO_2)^{\#-} \rightarrow CH_2NO_2 + H^- \quad (4.7)$$

which can be complementary to (4.6), with a threshold at 3.65 eV ($D(CH_2NO_2–H)$=4.40 eV and the electron affinity EA(H)=0.75 eV (Table 3)), below the reported experimental threshold at ~4.5 eV [28]. DEA to nitromethane producing H^- shows two broad resonant structures peaking at 7.5 and 9.0 eV which have been identified as signatures of core-excited resonances initiated via ($\sigma \rightarrow \pi^*$) or ($\pi \rightarrow \pi^*$) electronic transitions [28, 38]. This seems to be consistent with the energy loss spectra of K^+ ions formed in the forward direction at several collision energies [27]. Although these earlier TOF mass experiments were not able to detect H^-, the energy loss profiles, especially above 61 eV collision energy, show a broad structure peaking at 8 eV and extending to ~ 13 eV, which is particularly visible in the 183 eV incident K^0 beam profile.

It is also important to refer that deuterated nitromethane results show the formation of the anion D^-, confirming indeed the formation of the hydride anion in nitromethane. However, in the same spectrum (Figure 4.6) the H^- anion also appears which is quit intriguing considering that the molecule is deuterated. This could be explained by the presence of “regular” nitromethane in the deuterated nitromethane sample or, alternatively, through the underestimation of the background spectra which would implicate the contamination of the deuterated nitromethane results with background contributions. Further measurements would be required in order to clarify this matter.

4.4 Conclusion

The present electron transfer studies to nitromethane constitute a more extensive study than earlier work employing a higher mass resolution time-of-flight mass spectrometer. In addition to the three anions observed in previous studies, production of $CH_3NO_2^-$, $CH_2NO_2^-$, NCO^-, NO^-, CN^-, OH^-, and H^- have been observed. It was also possible, using deuterated nitromethane, to unequivocally show that fragment anion 17 a.m.u is in fact due to the production of OH^-.

Although rather complex the collision dynamics seems to be non-statistical, which was also reported in the spectroscopy and dynamics studies of negative ions of Walker and Fluendy [38] . This assumption is justified, within our experiment, by the fact that the branching ratio (relative to the total fragmentation) of the NO_2^- fragment is always greater than 65%, reaching ~80% for collision energies of 30 eV.

The anionic state associated with the formation of $CH_3NO_2^-$ has been referred to be a vibrationally excited $^2B_1(\pi * NO)$ state, which is subsequently stabilized by the potassium positive core into a long lived anion. The NO_2^- formation was associated with a repulsive $^2A_1(\sigma * CN)$, that competes with a rapid autodetachment. At low collision energies the bond stretching along the coordinate C-N precludes the autodetachment and favours both the increase of charge transfer and dissociation into NO_2^-. Formation of $CH_2NO_2^-$, NO_2^- and OH^-, through low energy resonances may be explained in terms of dissociative electron attachment to highly vibrationally excited molecules—hot bands.

As mentioned above, in atom-molecule collisions, the K^+ ion can strongly interact with the transient molecular anion, and if bond stretching is allowed in the target molecule during the electron transfer, strong vibronic coupling may occur. The lowest laboratory collision energy, 30 eV (18 eV in CM), is not only above the threshold for potassium ionisation (4.39 eV) but also above the energy formation thresholds and resonances, measured in DEA, for the formation of the reported fragments. This means that all nitromethane negative fragments are, from an energetic point of view, equally accessible at 30, 70 and 100 eV. Nevertheless, different relative cross section values are observed for each collision energy. This behaviour is in principle associated not only with the available energy itself but with the effect that the collision energy has in the collision time scale. As observed in the NO_2^- case, the collision time scale enhances bond-stretching effects responsible for the changes in formation probability of that particular fragment.

Chapter 5 Thymine and Uracil

5.1 Introduction

The role of ionising radiation as a source of damage to living cells has been recognised as a key issue regarding the cellular DNA integrity and, ultimately mutagenesis. It is now well established that ionising radiation, comprised mainly of α, β, X- and γ-rays, will interact with the cell components along its track, not only damaging them but also (and most importantly) creating secondary products, which in turn will also induce cellular damage. The DNA molecule is known to be particularly susceptible to this kind of damage [46], normally through Single and Double Strand Breaks (SSB and DSB's), which can result in a wide array of mutation-originated diseases. However, the specific mechanisms and entities that bring about this damage are still a subject of debate, as far as the real biological environment is concerned.

Experiments performed by Boudaiffa *et al.* [6] have shown the capability of secondary electrons to cause SSB's and DSB's in the DNA structure, through mechanisms of dissociative electron attachment (DEA) to the molecular constituents of the DNA molecule. These electrons with an energy distribution of 0-20 eV are indeed the most abundant secondary species produced along the radiation tracks and estimated to be created at a rate of 10^4 per MeV of incident energy [47]. This breakthrough has since then opened up a big interest in the study of the various DNA constituents in the gas-phase, namely the DNA basis and particularly thymine (T) and its RNA analogue uracil (U) (Figure 5.1).

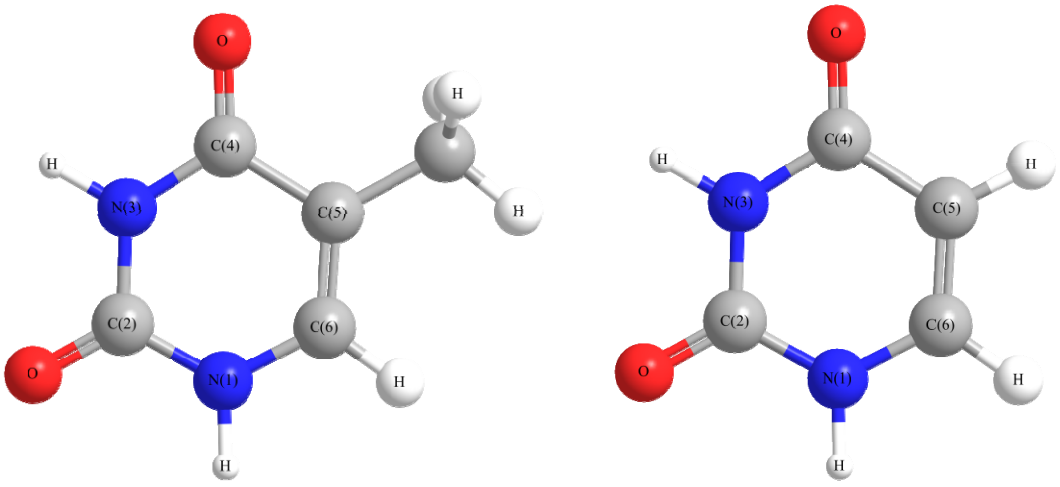

Figure 5.1 - Schematic representation of a) Thymine and b) Uracil.

From an experimental point of view, dissociative electron attachment with low energy (0-16 eV) electrons to gas-phase thymine [10, 48-50] and uracil [50-52] have been extensively studied. In these studies, a description of the various fragmentation channels is presented, and quantum chemical calculations have been performed to obtain electron affinities. Furthermore, additional studies using deuterated and methylated thymine (and uracil) in various ring positions have also been performed, showing site and bond selectivity upon low-energy electron interactions in both of these molecules [53-57]. As far as complementary experimental techniques are concerned, similar studies with charge exchange collisions with Rydberg atoms [58-59], Electron Transmission Spectroscopy (ETS) [60-62] and negative ion photoelectron spectroscopy [63-64] have also been reported. From theoretical studies, electron affinities (adiabatic and vertical) were calculated and the main σ* and π* LUMO orbitals for U were obtained [59-62, 65-66]. Most of the subsequent theoretical studies were performed mainly along the hydrogen abstraction reaction channel at the N_1 site, yielding the dominant fragments $(U\text{-}H)^-$ and $(T\text{-}H)^-$ [10, 48]. More recently, however, theoretical calculations on the low-energy resonant states of the transient negative ion (TNI) [67-70] provided key information on some of the more complex fragmentation pathways.

A significant attention was also given to the fact that both thymine and uracil, which have high dipole moments, $\mu \sim 4.5$ D, are able to sustain a dipole-bound anion states. In this anion states, the electron is temporarily captured in a dipole-induced orbital quite far from the molecular framework (8-10 Å [71]). This is in contrast with the valence-bound anion, where the extra electron will occupy a given LUMO of the molecule at typical distances of a few Å. However, in the case of uracil, ETS data and associated calculations propose that the dipole bound-state has a hybrid nature, i.e. has both a dipole potential-induced component as well as a valence state component [59, 64].

While a comparison between our data and DEA is attempted in this study regarding the accessible resonant states, the dynamics surrounding atom-molecule collisions are quite different from an electron-molecule collision. From the study of e^- + U/T, only electrons with an appropriate energy (resonance) can attach to the molecule for a time interval typically of the order of 10^{-16} s. This corresponds to the electron populating a given discrete state of the molecule, with the energy of the electron having the corresponding negative value of the Molecular Orbital (MO). In neutral atom-molecule collisions and subsequent ion-pair formation however, the electron is merely transferred from the neutral atom to the molecule when the wave functions corresponding to the covalent K + U/T and to the ionic interactions $K^+ + (U/T)^-$ become coupled, which only occurs at particular points of the reaction coordinates, known as the crossing radius. The required energy in these processes is given by the endoergicity for the electron transfer process to occur, which is provided by:

$$\Delta E = IE(K) - EA(Molecule) \tag{5.1}$$

Where *IE(K)* is the ionisation energy of the potassium atom and *EA*(Molecule) is the electron affinity of the molecule. As such, the allowed energies for the electron transfer cannot be chosen and the electron will be transferred to a given MO of the molecule with the corresponding energy being provided by the system.

In the present work, we have investigated for the first time the anionic fragments resulting from collisions of gas-phase uracil and thymine molecules with hyperthermal potassium atoms at three different collision energies (100, 70 and 30 eV), similar to recent published studies on the nitromethane molecule [72]. In this experiment, the electron transfer during the K + U/T collision can result in an ion-pair formation $K^+ + (U/T)^{\#-}$, where $(U/T)^{\#-}$ is the TNI, which in turn can decay either by autodetachment or dissociation through several different fragmentation channels.

5.2 Experimental conditions

Thymine and uracil negative ion formation, arising from the collisions with neutral potassium atoms, was probed by a TOF mass spectrometer at three collisions energies (30, 70 and 100 eV) within the laboratory framework. From equations (4.1) and (4.2) it was possible to determine the "available" energy in the CM framework, as show in Table 5.1.

Table 5.1 - CM framework collision energy conversion

E_{LAB}(eV)	E_{CM} Thymine(eV)	E_{CM} Uracil(eV)
30	20.4±0.7	19.8±0.7
70	47.5±0.7	46.1±0.7
100	67.9±0.7	65.9±0.7

The experimental parameters used in the collection spectra for both molecules, are shown below:

- **Thymine**

Table 5.2 - Experimental acquisition parameters used to measure Thymine

Experimental Parameters	30 eV	70 eV	100 eV
K chamber pressure (mbar)	6.80×10^{-7}	5.75×10^{-7}	6.03×10^{-7}
K oven temperature (K)	423	423	423
CE oven temperature (K)	443	443	443
Ion source current (A)	2.05	2.05	2.05
Ion source pulse width (μs)	2	2	2
Neutral Potassium beam (pA)	5.3	62.55	77.50
Collision chamber base pressure (mbar)	2.74×10^{-7}	2.07×10^{-7}	2.47×10^{-7}
Collision chamber work pressure (mbar)	2.74×10^{-5}	2.07×10^{-5}	2.47×10^{-5}
Biomolecules Oven temperature (K)	469	468	468
TOF Extracting voltage (V)	–300	–300	–300
TOF Acceleration voltage (V)	–3500	–3500	–3500
TOF Einzel Lens Voltage (V)	–1500	–1500	–1500
TOF Extracting Pulse width (μs)	1	1	1
Total Acquisition time (s)	32400	10800	10800
Acquisition delay (μs)	35.25	22.6	18.5
Acquisition bin width (ns)	8	8	8
Acquisition bin range (channel)	4096	4096	4096
Acquisition repetition rate (Hz)	14.28	16.12	16.66

- **Uracil**

Table 5.3 - Experimental acquisition parameters used to measure Uracil

Experimental Parameters	30 eV	70 eV	100 eV
K chamber pressure (mbar)	6.80×10^{-7}	5.75×10^{-7}	6.03×10^{-7}
K oven temperature (K)	423	423	423
CE oven temperature (K)	443	443	443
Ion source current (A)	2.05	2.05	2.05
Ion source pulse width (μs)	2	2	2
Neutral Potassium beam (pA)	5.75	64.09	164.50
Collision chamber base pressure (mbar)	2.74×10^{-7}	2.07×10^{-7}	2.47×10^{-7}
Collision chamber work pressure (mbar)	2.74×10^{-5}	2.07×10^{-5}	2.47×10^{-5}

Biomolecules Oven temperature (K)	465	465	463
TOF Extracting voltage (V)	–300	–300	–300
TOF Acceleration voltage (V)	–3500	–3500	–3500
TOF Einzel Lens Voltage (V)	–1500	–1500	–1500
TOF Extracting Pulse width (μs)	1	1	1
Total Acquisition time (s)	72000	18000	18000
Acquisition delay (μs)	35.25	22.6	18.5
Acquisition bin width (ns)	8	8	8
Acquisition bin range (channel)	4096	4096	4096
Acquisition repetition rate (Hz)	13.33	16.16	16.16

The collected TOF mass spectra, for both thymine and uracil (Figure 5.2 and Figure 5.3), were mass calibrated (equation (3.38)) and normalized (equation (5.2)). Finally, the background spectra obtained at the corresponding collision energy, were subtracted from the molecule spectra.

$$\frac{C}{t.f.I} \tag{5.2}$$

Here C is defined as the ion count (per channel), t the total acquisition time, f the acquisition rate and I the neutral potassium beam intensity (typically in pA).

5.3 Results and Discussion

As mentioned above, in this experiment we investigate the negative ion formation in K + Thymine(T) and K + Uracil(U) collisions. The TOF spectra obtained for these collisions are presented in Figure 5.2 and Figure 5.3, respectively.

The fragmentation observed for both molecules is quite similar, which given the molecular structure similarity between them is not entirely surprising. The fragmentation of these molecules is mainly composed of the dehydrogenated closed-shell parent anion $(T\text{-}H)^-/(U\text{-}H)^-$, the doubly dehydrogenated anion $(T–2H)^-/(U–2H)^-$, NCO^- and some other minor species (for thymine and uracil complete fragmentation see Table 5.4 and Table 5.5, respectively). While the formation of $(T–H)^-/(U–H)^-$, $(T–2H)^-/(U–2H)^-$, O^- and H^- can result from a simple bond cleavage, most of the other species are the result of a more complex molecular processes. These processes normally involve multiple bond cleavage of the ring and internal energy redistribution through the available degrees of freedom.

For comparison purposes, a list of the obtained fragments in potassium-uracil/thymine collisions, along with the most recent DEA results, is presented in Table 5.6. The negative ion formation results arising from both experiments show several similarities. It is however interesting to note that, between these two experiments, there is an inversion of the relative ion formation of two of the most intense anions. The most abundant negative ion in DEA experiments is $(T–H)^-/(U–H)^-$ followed by NCO^-, whereas in potassium-uracil/thymine collisions we observe the opposite behaviour. This is an interesting result and can suggest that, in collisions involving an electron donor (K), ring cleavage is enhanced which may have considerable biological relevance (we shall come back to this issue further below).

Given the molecular structure resemblance of both molecules, thymine and uracil neutral states are very similar. In fact, *Burrow et al.*[66] have performed quantum chemical calculations and obtained the three π* LUMO's at 0.29, 1.56 and 3.88 eV for uracil and 0.29, 1.71 and 4.05 eV for thymine. Furthermore, uracil has two lowest σ* valence orbitals whereas thymine has three. It is interesting to note that both σ* orbitals in uracil have very similar equivalent orbitals in thymine and that the extra third σ* orbital in thymine is mainly due to the hydrogen atoms of the methyl group. In this study, *Burrow et al.*[66] have also pointed out the strong overlap between one of the thymine/uracil σ* orbitals and the dipole-bound state. This opens the possibility of an intramolecular electron transfer mechanism from the dipole-bound state to the σ* valence orbitals, which will probably lead to bond cleavage. Both thymine and uracil have high dipole moments (μ>2.5D) which, as in the case of nitromethane, allow dipole-bond states to be formed. The presence of such states was probed for uracil through Rydberg electron transfer (RET) [58-59] and Photon Electron Spectroscopy experiments [63-64]. Furthermore, RET results show not only the presence of dipole-bond states but also suggests that the formation of valence anions via the former.

In ion-pair formation reaction, in potassium-uracil/thymine collisions, a transient negative ion (TNI) $T^{\#-}/U^{\#-}$ is formed. The dynamics of the TNI will be a critical element in the mechanisms, dissociative or otherwise, that follow the reaction. As far as general dissociation mechanisms are concerned, several theoretical studies now point out to the fact that bond breaks are primarily due to populating σ^* states, and that populating π^* states does not lead to dissociation or bond breaking *per se,* but rather through coupling mechanisms between the π^* and σ^* states [66, 69].

A major difference between the DEA experiments and both the present studies and RET studies is the presence of a third body, that acts as a stabilizing agent of the metastable $(T/U)^{\#-}$ ion. As such, the presence of the potassium cation (after electron transfer and in the vicinity of the TNI) can be responsible not only for reducing autodetachment but for dictating the other intramolecular processes that lead to dissociative channels (through bond-stretching effects).

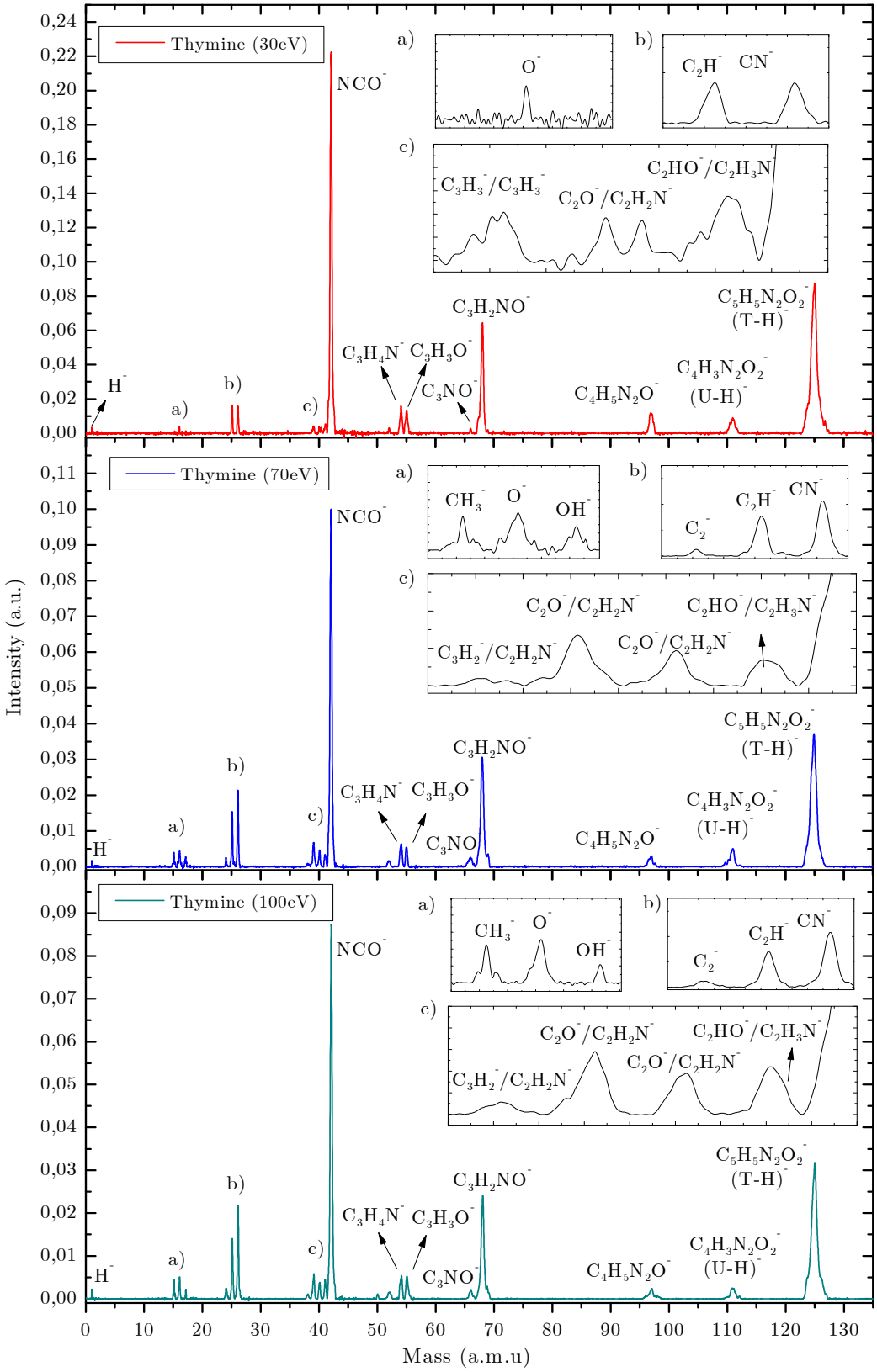

Figure 5.2 - Thymine TOF anion mass spectra at 30, 70 100 eV collision energies

Table 5.4 - Thymine negative ions assignment and related relative partial cross sections at several collision energies

		30 eV	70 eV	100 eV
Anion assignment	Mass (a.m.u)	Partial Relative Cross Section (a.u.)	Partial Relative Cross Section (a.u.)	Partial Relative Cross Section (a.u.)
H^-	1	0.011	0.00909	0.01251
NH^-/CH_3^-	15	0	0.0255	0.0244
O^-	16	0.011	0.0404	0.0340
OH^-	17	0	0.0182	0.00761
C_2^-	24	0	0.01186	0.0180
C_2H^-	25	0.078	0.0883	0.0822
CN^-	26	0.082	0.1150	0.1334
$C_3H_2^-/C_2N^-$	38	0	0.00705	0.00787
$C_3H_3^-/C_2HN^-$	39	0.023	0.0459	0.0363
$C_2O^-/C_2H_2N^-$	40	0	0.0267	0.0218
$C_2H_3N^-/C_2OH^-$	41	0.035	0.0208	0.0253
NCO^-	42	1.5	0.713	0.638
C_3N^-	50	0	0	0.00470
$C_3H_2N^-/C_3O^-$	52	0.0090	0.0137	0.0155
$C_3H_4N^-/C_2NO^-$	54	0.101	0.0455	0.0378
$C_3H_3O^-/C_2HNO^-$	55	0.091	0.0317	0.0374
C_3NO^-	66	0.0083	0.0305	0.0178
$C_3H_2NO^-$	68	0.50	0.308	0.221
$C_4H_5N_2O^-$	97	0.11	0.0319	0.0278
$C_4H_3N_2O_2^-$	111	0.098	0.0570	0.0301
$C_5H_5N_2O_2^-$	125	1.2	0.483	0.406

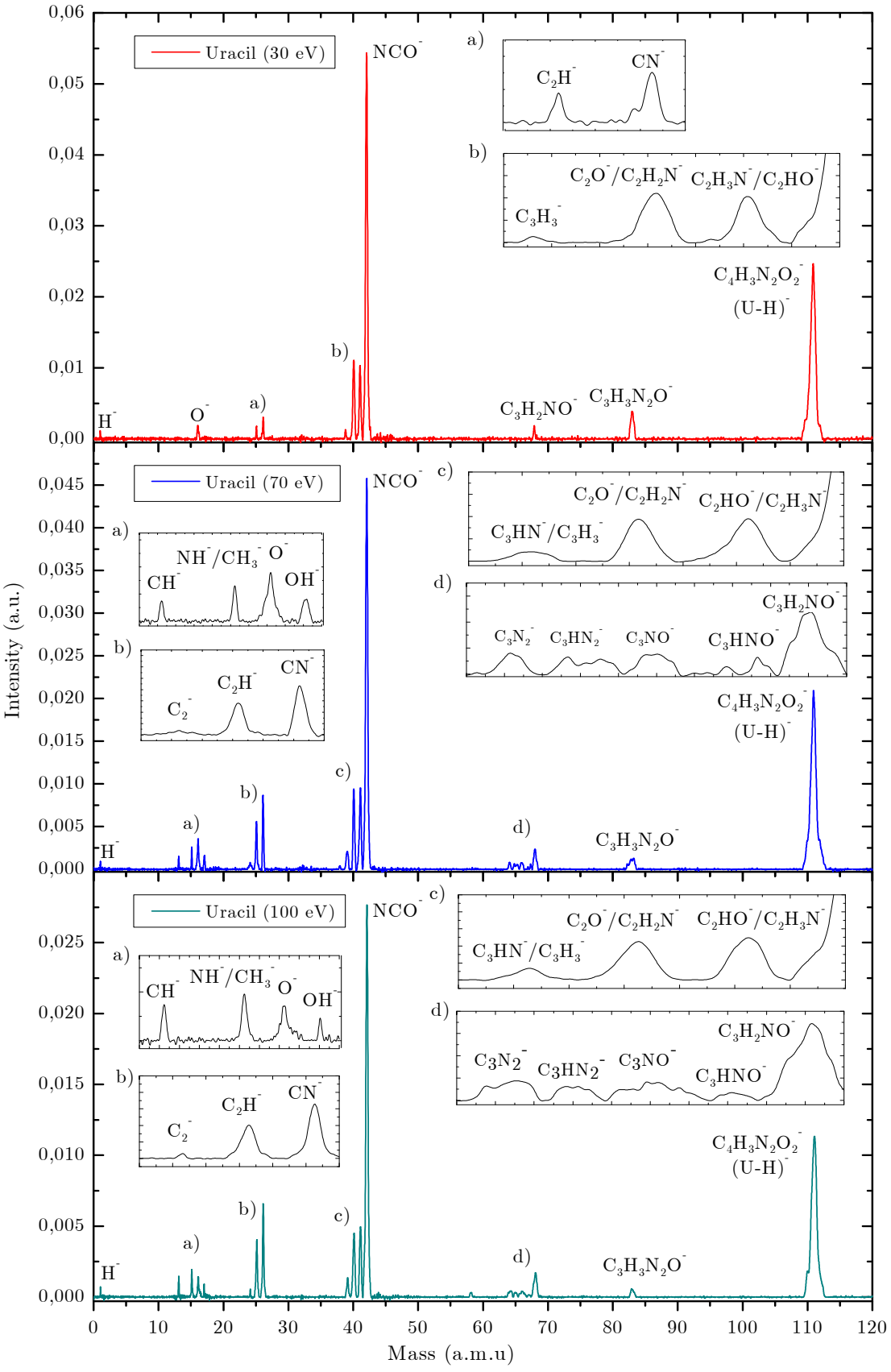

Figure 5.3 - Uracil TOF anion mass spectra at 30, 70 100 eV collision energies

Table 5.5 - Uracil negative ions assignment and respective relative partial cross sections at several collision energies

		30 eV	70 eV	100 eV
Anion assignment	Mass (a.m.u)	Partial Relative Cross Section (a.u.)	Partial Relative Cross Section (a.u.)	Partial Relative Cross Section (a.u.)
H^-	1	0.0037	0.00429	0.00373
CH^-	13	0	0.00547	0.00583
NH^-/CH_3^-	15	0	0.00962	0.00924
O^-	16	0.014	0.0261	0.01012
OH^-	17	0	0.00935	0.00213
C_2^-	24	0	0.00551	0.00139
C_2H^-	25	0.0048	0.0329	0.02458
CN^-	26	0.013	0.0406	0.0360
$C_2HN^-/C_3H_3^-$	39	0.0042	0.0146	0.00756
$C_2O^-/C_2H_2N^-$	40	0.067	0.0509	0.02901
$C_2H_3N^-/C_2HO^-$	41	0.057	0.0579	0.02968
NCO^-	42	0.36	0.318	0.1945
$CH_2N_2O^-$	58	0	0	0.00147
$C_3N_2^-$	64	0	0.00364	0.00356
$C_3HN_2^-$	65	0	0.00522	0.00194
C_3NO^-	66	0	0.00461	0.00386
C_3HNO^-	67	0	0.00146	3.07066E-4
$C_3H_2NO^-$	68	0.0061	0.0151	0.01279
$C_3H_3N_2O^-$	83	0.0286	0.0147	0.00405
$C_4H_3N_2O_2^-$	110	0.0113	0.0137	0.00758
$C_4H_4N_2O_2^-$	111	0.27	0.239	0.1330

Table 5.6 - Comparative tables on the DEA and electron transfer to thymine (left) uracil(right).

Anion	M (a.m.u)	[10, 62]	This work
H^-	1	×	✓
NH^-/CH_3^-	15	×	✓
O^-	16	✓	✓
OH^-	17	×	✓
C_2^-	24	×	✓
C_2H^-	25	×	✓
CN^-	26	✓	✓
$C_3H_2^-/ C_2N^-$	38	×	✓
$C_2HN^-/C_3H_3^-$	39	×	✓
$C_2H_2N^-/C_2O^-$	40	×	✓
$C_2H_3N^-/C_2HO^-$	41	×	✓
CNO^-	42	✓	✓
C_3N^-	50	×	✓
$C_3H_2N^-/ C_3O^-$	52	×	✓
$C_2NO^-/C_3H_4N^-$	54	✓	✓
$C_2HNO^-/C_3H_3O^-$	55	×	✓
C_3NO^-	66	×	✓
$C_3H_2NO^-$	68	✓	✓
$C_4H_5N_2O^-$	97	✓	✓
$C_4H_3N_2O_2^-$	111	×	✓
$C_5H_4N_2O_2^-$	124	✓	×
$C_5H_5N_2O_2^-$	125	✓	✓

Anion	M (a.m.u)	[51, 62]	This work
H^-	1	✓	✓
CH^-	13	×	✓
NH^-/CH_3^-	14	×	✓
O^-	16	✓	✓
OH^-	17	×	✓
C_2^-	24	×	✓
C_2H^-	25	×	✓
CN^-	26	✓	✓
$C_2HN^-/C_3H_3^-$	39	×	✓
$C_2H_2N^-/C_2O^-$	40	✓	✓
$C_2H_3N^-/C_2HO^-$	41	✓	✓
CNO^-	42	✓	✓
C_3N^-	50	✓	×
$CH_2N_2O^-$	58	×	✓
$C_3N_2^-$	64	×	✓
$C_3HN_2^-$	65	✓	✓
C_3NO^-	66	✓	✓
C_3HNO^-	67	✓	✓
$C_3H_2O^-$	68	✓	✓
$C_3H_3N_2O^-$	83	✓	✓
$C_4H_3N_2O_2^-$	110	✓	✓
$C_4H_4N_2O_2^-$	111	✓	✓

→ **$C_4H_3N_2O_2^-$ [(U-H)$^-$] / $C_5H_5N_2O_2^-$ [(T-H)$^-$]**

In DEA experiments, the dehydrogenated closed shell anions $C_4H_3N_2O_2^-$ [50-51] and $C_5H_5N_2O_2^-$ [10, 48-49] have been proposed to be formed via the following endothermic reactions:

$$e + C_4H_4N_2O_2^- \rightarrow C_4H_4N_2O_2^{\#-} \rightarrow C_4H_3N_2O_2^- + H \quad (5.3)$$

$$e + C_5H_6N_2O_2^- \rightarrow C_5H_6N_2O_2^{\#-} \rightarrow C_5H_5N_2O_2^- + H \quad (5.4)$$

The parent anion (T-H)$^-$/(U-H)$^-$ has been proven to have two different isomeric fragments, each corresponding to the abstraction of a hydrogen from the N_1 and N_3 sites [54, 57]. This fragment has already been reported in gas-phase with several experimental techniques in the case of uracil [50-52, 58-62] and thymine [10, 48-50]. In all cases, (T–H)$^-$/(U–H)$^-$ is the dominant fragment. This is not in agreement with our measurements, where the dominant fragment is CNO^-, which will be discussed further below.

In DEA experiments, several resonances for the formation of these fragments have been identified, all of them at subexcitation energies (i.e. E_{e^-} < 3 eV) [52]. These resonances were later identified to be a particular isomeric form. The lowest resonance at 1.01 eV was shown to correspond to the abstraction of the hydrogen at the N_1 site, while the second lying at ~1.8 eV results from the cleavage of the N_3-H bond. In RET [58-59] and negative ion Photon Electron Spectroscopy [63-64] experiments, the presence of (U–H)$^-$ was previously attributed to be an indicative of valence-bound U$^-$ formation. However, later was determined to be undoubtedly (U–H)$^-$. ETS studies in gas phase uracil, together with quantum chemical calculations, report the formation of (U–H)$^-$ through vibrational Feshbach resonances (VFR) from the neutral to vibrational excited states of the dipole-bound anion. These VRFs were found to be above the asymptotic limit of the σ_1* state, allowing the electronic wave function to tunnel through the barrier created by the avoided crossing between the DBS and the σ_1* in the N_1-H bond length coordinate [60], resulting in the hydrogen atom abstraction. Attempting a similar reasoning for the N_3-H would require a coupling between the DBS and the σ_2* [66], which is highly anti-bonding along this coordinate. This does not seem to be the case, which is supported by comparing the resonance structure of the dehydrogenated parent anion of thymine methylated in the N_1 (1-MeT) position and uracil methylated in the N_3 position (3-MeU) [66]. This study also suggests that the nature of the processes surrounding the abstraction of the hydrogen from the N_1 and N_3 sites may be of a quite different nature. The electron is attached through a shape resonance to the π_2* LUMO, that may couple with the σ_2* state resulting in the cleavage of the N_3-H bond [66]. One can suggest that the formation of (U–H)$^-$ from the cleavage of N_1-H can more easily be traced to the initial creation of a dipole-bound anion, while the formation of (U–H)$^-$ through N_3-H bond breaking pertains to the initial formation of a valence-bound anion state by populating the π_2* orbital.

In the present experiment, the dehydrogenated parent anion of both molecules is the second most abundant fragment at all three collision energies (100, 70 and 30 eV) probed. The relative cross sections were found to be of 0.13, 0.24 and 0.27 a.u. for $(T–H)^-$ and 0.41, 0.48 and 1.18 a.u. for $(U–H)^-$, with a branching ratio that rises from approximately 25% to 32.5% of the total anion yield with decreasing energy. In both cases there is a significant increase in the relative cross section with decreasing collision energy, which can suggest that there is a stabilization effect achieved by the presence of the potassium cation. It is, however, important to note that in the case of uracil, the main increase in the total anionic yield happens when going from 100 to 70 eV, while in thymine the main increase is between 70 and 30 eV.

The assessment of the relative cross section values of $(T–H)^-$ and $(U–H)^-$ and the corresponding values for NCO^- formation, can suggest that these fragmentation channels arise from populating the same initial anionic state, since although the cross sections are not the same, their behaviour for different energies appears similar (see Figure 5.4). However, DEA results are not consistent with this, since the resonance profiles for the formation of $(T–H)^-$/$(U–H)^-$ are all below 3 eV and for NCO^- appear, generally speaking, entirely above 4 eV.

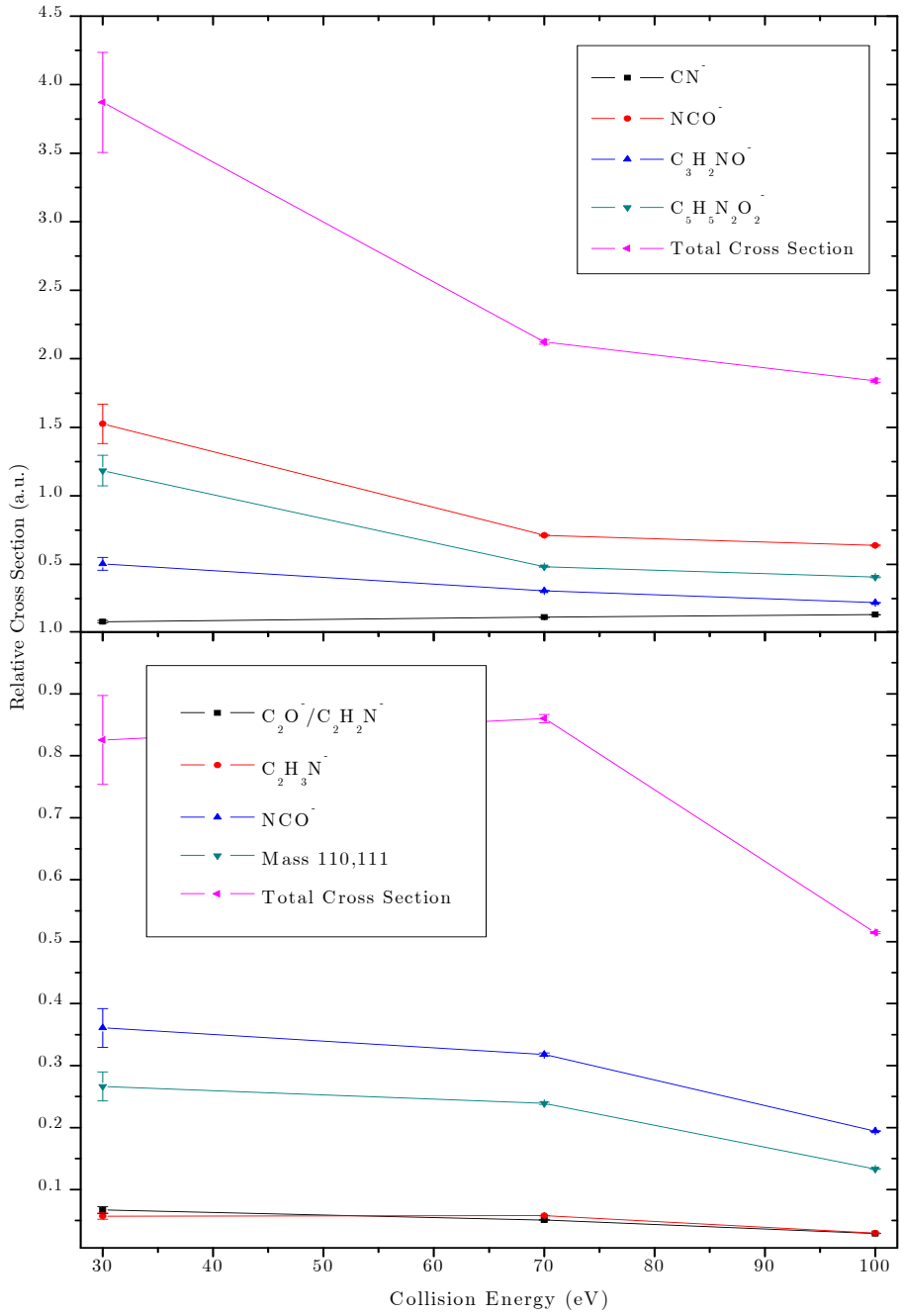

Figure 5.4 – Thymine (upper figure) and uracil (lower figure) partial cross sections (in arbitrary units)

→ NCO^-

In contrast to the dehydrogenated parent anion formation, NCO^- requires the cleavage of several bonds. NCO^- is the dominant fragment in our experiments at all collision energies, against the results obtained through DEA experiments [10, 48-51]. In the latter, NCO^- shows three resonances centred at approximately 5 eV, ~6.8 eV and ~10 eV, where 6.8 eV shows the highest cross section. This fragment can be formed through different fragmentation channels, all revolving around the abstraction of an hydrogen from the N_1 or N_3 sites, which is in agreement with the possibility that the dehydrogenated parent anion is in fact an intermediate. This is not surprising considering the energy spectra obtained in recent DEA studies with thymine embedded in helium droplets [73], which is further sustained in our studies by the parallel behaviour of the NCO^- and $(T–H)^-/(U–H)^-$ cross sections. By looking at the resonance of both CNO^- and other similar, yet less abundant fragments (e.g. CN^-, $C_2H_3N^-$, C_3N^-, $C_3HN_2^-$), one can see that some of the resonances are shared between them, particularly the resonances at ~6.8 eV and ~10 eV, which can indicate that the precursor state of these fragments is the same. Moreover, a quite interesting fact is the presence of the $C_3H_2NO^-$ fragment, which happens to be the complementary fragment of NCO^- (together with an hydrogen abstraction) in uracil. Indeed, by looking at the resonances of these fragments with free electrons at ~5 eV, ~6.8 eV and ~10 eV, one can also suggest that both of these fragments are formed through the same anionic states. As such, the reaction channels

$$e^- + C_4H_4N_2O_2 \rightarrow (C_4H_4N_2O_2)^{\#-} \rightarrow H + C_3H_2NO + NCO^- \quad (5.5)$$

$$e^- + C_4H_4N_2O_2 \rightarrow (C_4H_4N_2O_2)^{\#-} \rightarrow H + C_3H_2NO^- + NCO \quad (5.6)$$

may be viewed as stemming from the same bond cleavages. The explanation for the higher NCO^- cross section resides on the fact that this neutral fragment is a pseudo-halogen and therefore known for its quite high electron affinity (3.8 eV). A similar explanation may be found for the C_3HNO^- and C_3NO^- fragments, which can arise from the same bond cleavages as $C_3H_2NO^-$ but requiring the breaking of additional hydrogen bonds. However, this reasoning does not hold true for thymine which would require the formation of $C_4H_4NO^-$.

In our experiment $(T–H)^-/(U–H)^-$ branching ratios for NCO^- show an increase from 37.5% to 44% of the total anion yield with decreasing energy. In recent DEA experiments with thymine embedded in helium nanodroplets, was demonstrated that the dehydrogenated parent anion $(U–H)^-$ is indeed a precursor in the formation of the fragments that require bond cleavages in the ring, namely NCO^- [73]. In this study, the ion yield of the dehydrogenated parent anion embedded in He nanodroplets presents two resonances centred around approximately 1.25 and ~6.5 eV, respectively. The lowest resonance is also observed for the bare nucleobase, whereas other high energy (> 3 eV)

features are absent. However, when the total anion yield of the remaining fragmentation is obtained for the nanodroplets, a similar shape appears located at the same high energy region (see Figure 5.5).

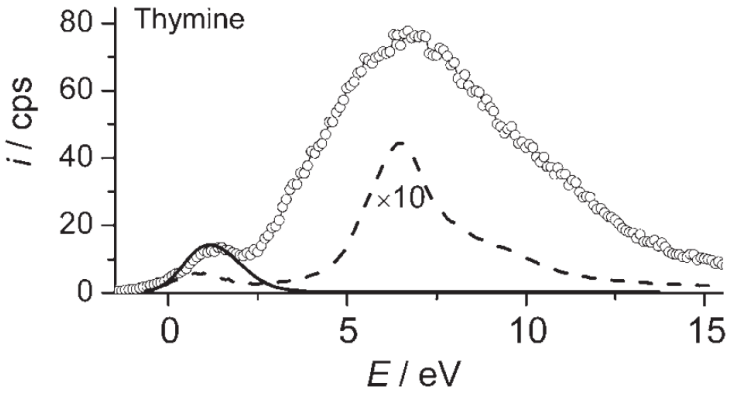

Figure 5.5 - The line drawn with circles (o) represents the ion yield as a function of the electron energy of $[T\text{-}H]^-$ upon DEA to the NB embedded in He droplets at 0.37 K. The solid line (—) shows the anion efficiency curves of $[T\text{-}H]^-$ while the dashed line (----) represents the sum of all other observed product anions, upon DEA to the corresponding bare nucleobase molecules. (Adapted from [73])

This suggests that the formation of a dehydrogenated parent anion is an intermediate step in the formation of all other fragments. Furthermore, and perhaps most importantly, there is a significant decrease in intensity between the anion yield of this second higher energy resonance and the obtained total anion yield mentioned above. A reason for this discrepancy is the greatly enhanced possibility of autodetachment competing with dissociation in the case of the bare nucleobase, when compared with the same molecule embedded in He droplets. This can be explained due to the presence of the He droplets may partially preclude the possibility of autodetachment. Therefore, one can argue that in the case of DEA, the dominant fragment will be the dehydrogenated parent anion, formed at subexcitation energies only [54], and that ring breaking fragments are only obtained at higher energies.

According to DEA studies [10, 49-52], the main resonance in the formation of NCO^- (as well as in many other fragments) is around 6.8 eV which we can tentatively attribute to the initial occupation of π_3^*. A recent theoretical study using S-matrix electron scattering calculations [69] studied the dynamics associated with the adiabatic extension of two given ring bonds and how it relates to the calculated σ^* and π^* orbitals involved (Figure 5.6). The study has shown that the anti-bonding character when the bond is stretched stems almost exclusively from σ^* orbitals, while the π^* orbitals appear largely unaffected. This leads to the suggestion that bond breaking is due to population of σ^* orbitals and that access to π^* orbitals does not directly lead to dissociation but may serve as a doorway to access the σ^* orbitals.

In the present atom-molecule studies, if one assumes that the presence of the potassium cation is somehow suppressing the possibility of autodetachment, the electron that is initially populating a

π_3* at 6.5 eV is allowed more time to, through the non-adiabatic coupling to the ring σ* orbitals [69], inducing bond breaks in the ring and depositing a significant amounts of energy (as much as 4 eV, which can be distributed along the internal degrees of freedom) in the molecular frame (Figure 5.6).

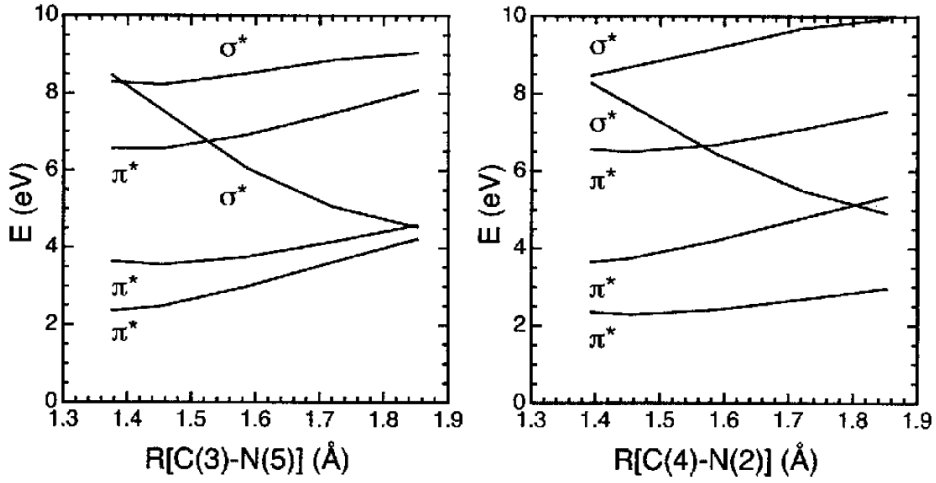

Figure 5.6 - Computed real parts of the A´ and A´´ resonance energies as a function of ring-breaking deformations in uracil. The left panel deals with the C_3-N_5 stretch while the right panel is for the C_4-N_2 stretch [69].

Indeed, the resonance width of the π*(6.5 eV) is 1.13 eV [69], which corresponds to an autodetachment lifetime of 0.59 fs. This is approximately three times smaller than the lifetimes for the other calculated π* LUMO's (2.75 fs for π_1* and 1.74 fs for π_2*). It is possible to assume that the fragmentation channels that involve this π*(6.5 eV) orbital are somewhat suppressed in regular DEA experiments due to the very low autodetachment lifetimes. In our case, however, the potassium cation may stabilize the molecular complex allowing the electron more time to be transferred to other overlapping orbitals.

A similar reasoning can also be made for the calculated σ* lifetimes. In terms of the C_4-N_2 bond, the σ*(8.49 eV) lifetime will be approximately 0.29 fs [69][67][39] and is relatively unchanged during bond stretching. However, the σ*(8.29 eV) orbital in the equilibrium position has an autodetachment lifetime of 0.37 fs but as the bond is stretched, the lifetime significantly increases up to 1.46 fs. In the C_3-N_5 bond, the lifetime of the σ*(8.29 eV) will remain relatively constant around 0.37 fs and σ*(8.49 eV) will increase from the equilibrium value of 0.29 fs to 0.75 fs [69]. This suggests that, from a free electron attachment point-of-view, the initial occupation of one of these σ* is virtually a dead end, since the electron will very easily autodetach. On the other hand, if the electron initially occupies the already mentioned π_3*(6.5 eV), it can then hop to one of the σ* orbitals, which at higher bond lengths has a significantly higher lifetime, hence allowing time for the dissociation to occur.

A closer analysis of these σ* orbitals also shows a quite significant anti-bonding character in the N-H bonds [69]. Despite this, these σ* orbitals show quite small autodetachment lifetimes in the equilibrium (initial) geometry, greatly decreasing the efficiency of these fragmentation channels in DEA experiments, which is in agreement with the dehydrogenated parent anion being the dominant fragment. This is not clearly the case in our study and therefore one is then tempted to attribute the greatly enhanced anion yield of ring-breaking fragments in our experiments to the presence of the potassium anion that, by precluding (totally or at least partially) autodetachment, greatly increases the efficiency of the fragmentation channels proposed above against autodetachment. A similar mechanism was already discussed for nitromethane in the previous chapter.

In conclusion, NCO^- formation can be viewed as a multi-step process. Initially, the electron will be captured into a higher energy π*. This π* state was shown to have not sufficient anti-bonding character to be responsible for dissociation whereas non-adiabatic coupling mechanisms with σ* orbitals may be responsible for the fragmentation [69]. At this stage, the difference between DEA and electron transfer by atom-molecule collisions is critical. In the former, the occupation of not only this π* orbital but mainly the σ* orbitals, due to their quite low autodetachment lifetimes, will most likely result in the premature ejection of the electron. However, for the latter, the presence of the potassium cation stabilizes the molecular anion complex long enough so that the electron can more effectively transfer to the σ* and also allow bond stretching to occur long enough for the σ* lifetimes to increase. This is in agreement with the increase in the relative cross section for the total anion yield with decreasing energy, hence increasing collision time. Regardless, after the occupation of the σ*, the dissociation channel can also be viewed in two stages where initially the hydrogen is abstracted, owing to the significant anti-bonding character of the σ* orbital in its initial geometry and to the significantly faster abstraction time of the hydrogen. After the fast abstraction of the hydrogen, the $(T–H)^-$/$(U–H)^-$ will then follow the PES of the populated σ* orbital, eventually leading to the formation of the fragments that stem from the breaking of the ring bonds, particularly yielding NCO^-. This mechanism may follow an adiabatic picture, within the Born-Oppenheimer framework, as discussed above [69].

→ $C_5H_4N_2O_2^-$/$C_4H_2N_2O_2^-$ [$(T\text{-}2H)^-$/$(U\text{-}2H)^-$]

In DEA experiments, the doubly dehydrogenated parent anion of both uracil and thymine shows a peak structure consisting of three resonances. The first is at virtually no energy, the second at 7.22 eV and the third at 10.59 eV [10, 51]. In our experiment, yet we report $(T–2H)^-$/$(U–2H)^-$ as a possible fragmentation channel. Although the resolution of our TOF spectrometer does not allow to unambiguously assign the shoulder in the left of the peak $(T–H)^-$/$(U–H)^-$) (Figure 5.2 and Figure 5.3) as pertaining to the double dehydrogenated parent anion $(T–2H)^-$/$(U–2H)^-$. Recent on-going measurements in our laboratory with deuterated thymine have enabled us to clarify the nature of such

structure in thymine, which should also be valid for uracil. In the case of $(T–2H)^-$, the resonance structures in DEA appear quite similar although the cross section for the ~0 eV resonance is much more intense. In the case of thymine, site selectivity in the doubly dehydrogenated parent anion has been already shown [53]. Studies to determine from which site the hydrogens are abstracted, within our experiment, are being undertaken by making use of deuterated and methylated compounds.

$\rightarrow O^-$

In DEA experiments, the O^- formation is obtained through a single broad resonance at 10.4 eV [51]. Within our experiments, the dissociation channel yielding O^- does not seems to follow a simple bond cleavage of the C-O double bond. Moreover, when comparing the ratio of the yields of O^- and $(U–H)^-$ in DEA experiments [51] and in our charge transfer studies, a significant enhancement in the formation rate of O^- is obtained, which is similar to what happens with the aforementioned NCO^- fragment. When comparing the O^- formation cross section with the dehydrogenated parent anion cross section of U and T in DEA studies, the values appear quite different. In our technique however, this is not the case, i.e. relatively to the parent ion formation, O^- relative cross section appears to have a similar formation rate. This may suggest that the formation of O^- also has the dehydrogenated parent anion as a precursor fragment, therefore agreeing with the DEA studies of thymine embedded in He droplets [73].

$\rightarrow OH^-$

The OH^- formation has not been reported in free electron attachment experiments [51]. In our charge transfer studies with uracil and thymine, the OH^- yield is significantly lower than the O^- for 100 and 70 eV and completely disappears at 30 eV. It should be noted that the OH^- signal associated with the presence of residual gas (water) in the chamber has been removed from the present mass spectra by subtracting the background signal.

Alternatively, if one considers the possibility of tautomerization, where one of the hydrogens (from the nearby N-sites) is moved to the oxygen, the formation of this fragment can be explained by a single bond cleavage of the OH of the tautomer. However, infrared studies [74] of both thymine and uracil do not detect the presence of tautomerization. Furthermore, the conditions of the target molecule in both our studies and in DEA studies are the same, which leads us to expect that the formation of OH^- from the tautomer would be approximately abundant. This, however, is not the case since DEA studies do not report the formation of OH^-. Yet, there is the possibility that the presence of the potassium cation *post-collision* may enhance the possibility of tautomerization and hence allow the resulting enol tautomer to be a precursor for the formation of this fragment.

Another possibility for OH^- formation is the presence of residual water adsorbed in the oven walls, which would be only released when the oven was heated up to the required temperature. This

rationale could account for an eventual increase in the yield of H^-, O^- and OH^-. However, the background spectra were obtained for an oven temperature of 120 ºC, so we do not expect any water contribution.

→ Other Aromatic ring fragmentation (Uracil)

The assignments of the main ring fragment anions from the collision of potassium atoms with thymine/uracil molecules and those from free electron attachment experiments are listed in Table 5.6. The formation of such species requires considerable internal rearrangement in the TNIs and therefore the energy available may only be provided at high impact energies. Although not shown here, we have found that the branching ratios for such species indeed increase with increasing collision energy. The discussion below is mainly focused on the major differences found in potassium impact and free electron attachment experiments.

H^- formation has been extensively studied due to its relevance in understanding mechanisms of site- and bond-selectivity in free electron attachment experiments [53-57]. Although there is no information about this fragment for uracil, we assume that the process follows as in the case of thymine. Preliminary measurements of deuterated thymine in the carbon sites indicate formation of H^- and D^- which reinforces the fact that the hydride anion detection is a contribution from both carbon and nitrogen sites. This will also appear soon in another publication. Both in free electron attachment [10, 51] and in the present charge transfer experiments, fragments of mass 41, 40, 26 and 8 a.m.u are detected. The DEA energy spectra show that all these fragment anions, as well as NCO^- discussed above, share resonances at ~6.8 and ~9.5 eV and are therefore expected to be formed through the same dissociation channels. To a lesser extent, the fragments of mass 50 and 65 a.m.u also show DEA resonances at these energies and therefore are also expected to be obtained through the same mechanisms as NCO^-. While the ~6.8 eV resonance has been tentatively assigned to the occupation of a π_3 orbital [69] the assignment of the ~9.5 eV feature can be attributed to core-excited resonances or Rydberg excitations.

The fragment masses 64, 58, 39, 25, 24, 15 and 13 a.m.u have not been reported in free electron attachment experiments and therefore information on the energy resonance profiles is not available, unabling us to draw significant conclusions as to the reason for the difference between our study and DEA. However, the intensity of the $C_3N_2^-$ fragment as a function of the collision energy is similar to $C_3HN_2^-$, which may suggest that these two negative ions may have a common precursor anion. The $C_3H_2N_2O^-$ fragment is quite weak and only visible at 100 eV. The 39 a.m.u fragment has been tentatively assigned to C_2HN^- (resulting in the loss of a hydrogen atom from $C_2H_2N^-$) or $C_3H_3^-$. The 15 a.m.u fragment has been assigned the imidogen (NH^-) which seems to be supported by preliminary measurements of carbon-deuterated thymine, that do not show the presence of a fragment at 18 a.m.u (which would correspond to CD_3) and therefore further sustain the NH^- anion assignment.

Finally, the presence of the doubly dehydrogenated parent anion is also detected in our study, although it is only visible as a shoulder in the left flank of the peak corresponding to the dehydrogenated parent anion.

→ Other ring fragmentation (Thymine)

As in the previous section, the molecular structures are not known for the tentative assignments of the fragments that are only visible in the present experiments. We have found that the branching ratios for such species indeed increase with increasing collision energy, as was already stated earlier.

The fragment anions at 111 and 15 a.m.u were not reported in the free electron attachment studies [10, 48-49] and have been tentatively assigned to $C_4H_3N_2O_2^-$ and NH^-/CH_3^-, respectively. It is tempting to assign CH_3^- to the abstraction of the methyl group in the parent anion and therefore competing with the formation of $C_4H_3N_2O_2^-$. However, as was already pointed out, carbon deuterated thymine measurements do not show any presence of CD_3^-, which then allows, as in uracil, mass 15 to be attributed to NH^-. It is worth noting that the fragment of mass 71 a.m.u is not detected in our experiments but it is however detected in DEA studies [10]. Interestingly, in the latter studies, its yield is higher than, for example, the yield of $C_3H_2NO^-$. This can point to the conclusion that, since it is not a question of sensitivity of the experimental setup, formation of $C_3H_2NO^-$ in atom–molecule collisions is somehow suppressed in detriment of other fragments.

The fragment of mass 97 a.m.u is most likely to correspond to the thymine analogue of $C_3H_3N_2O^-$ in uracil since the DEA experiments show for these anions a resonance profile peaking at ~6 eV with clear resemblance between each other, both in shape and in magnitude, considering the difference in their cross sectional values, i.e. uracil shows a value a factor of 4 higher than thymine. Regarding the fragments at masses 24, 25, 26, 40 and 41 a.m.u, the mechanism should be similar to uracil. The 39 a.m.u fragment anion is also shared with uracil but was not reported in the free electron attachment studies [10, 48-49]. It is interesting to note that its dehydrogenated analogue ($C_2N^-/C_3H_2^-$) is also present but does not appear in uracil. Finally, it is worth noting that in the present measurements of thymine, a fragment of mass 111 appears which is not reported in DEA. This fragment most likely corresponds to the demethylated anion $(T–CH_3)^-$. Preliminary studies with methylated thymine and uracil also exhibit the presence of such species. Ensuing studies are currently being performed.

5.4 Conclusions

Electron transfer-induced processes in neutral low energy atom-molecule collisions are presently a relatively unexplored field, particularly in respect to biological relevant molecules. These processes can be viewed as a new approach to better understand how exactly do (bound) electrons act as dissociation agents in (biological relevant) molecules and the comparison of this data with DEA experiments is here proven to provide some insight into the fragmentation dynamics of the target molecules. Taking into account that electrons in the physiological environment may exist in bound states, one can argue that our technique is better tuned to simulate electron-induced processes than simple low energy electrons (LEE).

Several earlier studies based in DEA have significantly given a relevance in the role of not only the parent dehydrogenated anion and how electrons can damage macro-molecular structures such as the DNA molecule, but also in the damaging effect that the hydrogen radical can impart on nearby molecular structures. In this study however, the relevance of the presence of a third-body in the collision dynamics is highlighted and some similarities with electron carriers in the biological medium can perhaps be more adequately discussed.

The fragmentation patterns of thymine and uracil with free electrons and potassium atoms have revealed to be significantly different. The first major point in this study is the greatly increased anion yield of fragments that rises from bond breaks in the ring in comparison with DEA studies, where the main fragmentation is due to the dehydrogenated parent anion. Experimental evidences [50] are pointing to the fact that, in DEA experiments, high autodetachment rates are responsible for decreasing the formation of anionic species arising from orbitals associated with ring bonds breaking, especially NCO^- formation. However, in our experiment, the greatly enhanced relative anion yield of fragments that require the breaking of the ring is proposed to arise from the third body stabilizing effect, that decreases autodetachment, hence more easily allowing a transfer to the ring-breaking σ^* orbitals [69, 71]. A similar mechanism has already been proven to work for low energy Rydberg atom-molecule collisions [58-59].

The effects of free electrons can greatly overestimate the relevance of the dehydrogenated parent anion. Indeed, as is striking in the present study, one should not only consider the importance of the dehydrogenated parent anion when studying electron interaction with biological relevant structures but perhaps even more important is the study of the remaining fragmentation reflecting from ring breakings which has so far been somewhat ignored due to its relatively low cross sections. Some of these fragments can have quite high electron affinities and therefore can also be quite damaging to neighbouring molecular structures.

From a more fundamental point of view, the study of these types of molecules with this technique is unprecedented. The fact that both molecules have a relative high dipole moment leads to

the existence of stable dipole-bound states, which have been proven to be an intermediate state to electron capture to a valence orbitals [58-59, 63-64]. According to these studies, one of the requirements is the presence of a third body to help stabilize the complex against autodetachment [75] which they achieve by using laser excited Rydberg-like atoms, namely Xe (nf). As such, our technique can also help provide some insight regarding the formation and dynamics of these dipole-bound states.

Chapter 6

5-Chlorouracil and 5-Fluorouracil

6.1 Introduction

Concomitant cancer chemoradiation therapy is gradually becoming a dominant treatment for oncological patients. By using chemotherapy simultaneously with radiotherapy, allows for the implementation of therapies at low doses when compared with radiotherapy used as a single treatment. This conjunction of procedures involves a radiosensitizer that will enhance DNA damage when subjected to the same amount of dose. Halouracils have long been proposed as radiosensitizers, owing to their ability to easily dissociate when subjected to radiation. These molecules, by replacing their analog in the DNA structure will therefore greatly increase the dissociation yield of DNA, eventually increasing the rate of cell death. The chemical structure of halouracils is very similar to thymine, the methyl group in the C_5 position is replaced by a halogen atom. Prior to irradiation the halogen substitution does not change the DNA genetic sequence or expression [11].

It is known that non-solvated electrons with energies below 30 eV are produced in abundance, at a rate of approximately 5×10^{-4} per MeV of incident energy, via ionising radiation pathways, and are able to induce irreversible damage to DNA and RNA as single (SSB) and double (DSB) strand breaks [6, 76]. The interactions of these electrons with life tissues are still an open and quite unanswered question, not only regarding the exact nature of these interactions but also their relevance regarding DNA damage. As such, physicists, chemists and physical chemists have recently devoted themselves to studying how the individual molecules that compose the DNA structure are affected by the ionising radiation.

Halouracils can dissociate resonantly after electron impact leading to genotoxic radials formation, as long lived anions. Several studies have been carried out concerning interactions of slow electrons (< 30 eV) with 5-halouracils [11, 77-82]. Dissociative electron attachment (DEA) processes via electron capture to halouracils were described not only in those experimental studies but also in theoretical studies, such as DFT calculations [83-84] and other *ab initio* calculations [65, 71, 85]. Several experiments with thymine and halogen-substituted oligonucleotides adsorbed on surfaces have been carried out by Sanche's group [82, 86] and have shown desorption of CN and CNO anions after electrons impact at energies below 30 eV occurs.

Upon electron attachment, the transient negative ion (TNI) may follow several pathways. It may dissipate the excess energy via photon emission or energy transmission to the vicinity (mainly in the case of clustering environment), it can also decay via ion-pair formation or electron detachment or finally, it may decay via dissociative electron attachment (DEA) leading to the formation of different anionic fragments. The fragmentation pattern is unique to each molecule and depends on the energy deposited in the target molecule. In halouracils, high electron affinity elements or group of elements are present, halogen atoms or pseudo-halogen species such as CNO, CN and O groups, which play an important role in the pattern of fragmentation.

Halouracil negative ions can be formed via dipole- or valence-bound states. The dipole moments of uracil, 5FU and 5ClU, are 4.58D, 4.21D and 4.14D [85] respectively. It is well established that these dipole moments allow the formation of stable dipole-bound anions [87]. These halouracils dipole bound anions are formed through trapping of an incoming electron by the dipole moment of the molecule which occupies a diffuse Rydberg orbital. In this case, the geometry of the molecule and its corresponding negative ion have virtually identical geometries. Alternatively, the negative ion may be formed when the extra electron occupies a valence orbital yielding a valence anion. In this negative ion formation process the geometry of neutral differs substantially from the neutral precursor [71]. In the present case, dipole-bound states and valence states can overlap allowing electron transfer between both states. Studies by Sommerfeld have shown that dipole-bound states can act as doorways to the formation of valence states, allowing long lived radical anions formation, as have been proved for uracil and 5-chlorouracil [65].

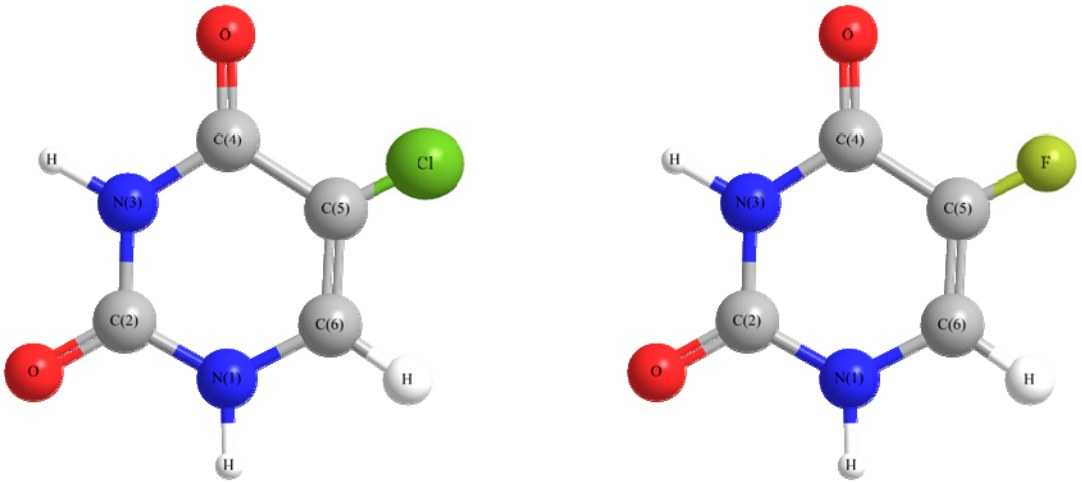

a) b)

Figure 6.1- Schematic representation of a) 5-chlorouracil and b) 5-fluorouracil.

In the present work we will focus on two halouracils, 5-ClU and 5-FU (Figure 6.1). In this study, we attempt to describe the dynamics of negative ions formation via electron transfer in potassium-halouracils collisions. Several studies concerning negative ion formation after free electron attachment have been published. However the formation of such anions through electron transfer is still unknown and is being shown here for the first time. Furthermore, it will be shown that fragmentation patterns for 5-ClU and 5F-U show some similarities in respect to DEA studies, although the total number of ions formed is more abundant (in K-molecules studies).

6.2 Experimental conditions

5-chlorouracil and 5-fluorouracil negative ion formation, arising from the collisions with neutral potassium atoms, was probed with a TOF mass spectrometer at three collisions energies (30, 70 and 100 eV) in the laboratory framework. From equations (4.1) and (4.2) was possible to determine the "available" energy in the CM framework, as show in Table 6.1.

Table 6.1 - CM framework collision energy conversion

E_{LAB}(eV)	E_{CM} 5-chlorouracil(eV)	E_{CM} 5-fluorouracil(eV)
30	21.1±0.7	20.5±0.7
70	49.3±0.7	47.8±0.7
100	70.3±0.7	68.4±0.7

The experimental parameters used in the collection of spectra for both molecules, are shown below:

- **5-Chlorouracil**

Table 6.2 - Experimental acquisition parameters used to measure 5-chlolouracil

Experimental Parameters	30 eV	70 eV	100 eV
K pressure (mbar)	6.65×10^{-7}	6.05×10^{-7}	6.30×10^{-7}
K oven temperature (K)	423	423	423
CE oven temperature (K)	443	443	443
Ion source current (A)	2.05	2.05	2.05
Ion source pulse width (μs)	2	2	2
Neutral Potassium beam (pA)	5.3	42.9	84.5
Collision chamber base pressure (mbar)	2.43×10^{-7}	2.50×10^{-7}	2.42×10^{-7}
Collision chamber work pressure (mbar)	2.43×10^{-7}	2.50×10^{-7}	2.42×10^{-7}
Biomolecules oven temperature (K)	465	466	463
TOF Extracting voltage (V)	–300	–300	–300
TOF Acceleration voltage (V)	–3500	–3500	–3500
TOF Einzel Lens Voltage (V)	–1500	–1500	–1500
TOF Extracting Pulse width (μs)	1	1	1
Total Acquisition time (s)	36000	18000	18000
Acquisition delay (μs)	35.25	22.6	18.5
Acquisition bin width (ns)	8	8	8

Acquisition bin range (channel)	4096	4096	4096
Acquisition repetition rate (Hz)	13.33	16.66	16.66

- **5-Fluorouracil**

Table 6.3 - Experimental acquisition parameters used to measure 5-fluorouracil

Experimental Parameters	30 eV	70 eV	100 eV
K pressure (mbar)	6.24×10^{-7}	6.02×10^{-7}	6.67×10^{-7}
K oven temperature (K)	423	423	423
CE oven temperature (K)	443	443	443
Ion source current (A)	2.05	2.05	2.05
Ion source pulse width (us)	2	2	2
Neutral Potassium beam (pA)	6.45	13.7	46.50
Collision chamber base pressure (mbar)	2.21×10^{-7}	2.02×10^{-7}	2.68×10^{-7}
Collision chamber work pressure (mbar)	2.21×10^{-7}	2.02×10^{-7}	2.68×10^{-7}
Biomolecules oven temperature (K)	465	464	463
TOF Extracting voltage (V)	–300	–300	–300
TOF Acceleration voltage (V)	–3500	–3500	–3500
TOF Einzel Lens Voltage (V)	–1500	–1500	–1500
TOF Extracting Pulse width (μs)	1	1	1
Total Acquisition time (s)	36000	18000	18000
Acquisition delay (μs)	35.25	22.6	18.5
Acquisition bin width (ns)	8	8	8
Acquisition bin range (channel)	4096	4096	4096
Acquisition repetition rate (Hz)	13.33	16.66	16.66

The collected TOF mass spectra, for both 5-chlolouracil and 5-fluorouracil (Figure 6.2 and Figure 6.3), were mass calibrated (equation (3.38)) and normalized (equation (5.2)). Finally, the respective background spectra were subtracted from the actual spectra in order to eliminate anionic contributions from the background in the collision chamber.

6.3 Results and Discussion

The TOF spectra obtained for potassium-(5-chlorouracil) and potassium-(5-fluorouracil) are shown in Figure 6.2 and Figure 6.3, respectively. The most abundant fragmentation of the potassium-(5-chlorouracil) collision comprises the chloride anion $^{35}Cl^-$ followed by its isotope $^{37}Cl^-$, in an isotopic abundance of ~3:1. Furthermore, is possible to identify the formation of NCO^-, $(ClU–HCl)^-$, the parent ion and the dehydrogenated parent anion of both the ^{35}Cl and ^{37}Cl isotopes and some other less intense anionic fragments (see Table 6.4 and Figure 6.2). For potassium-(5-fluorouracil) collisions, the most abundant anion is NCO^- followed by F^-, C_3NO^-, CN^-, the dehydrogenated parent anion and other less abundant species (see Table 6.5 and Figure 6.3).

For comparison purposes, a list of the fragments formed in potassium-(5-chlorouracil/5-fluorouracil) collisions, along with the most recent DEA results are presented in Table 6.6. From this table is possible to infer that the negative ion formation results arising from both experiments present several similarities. Nevertheless, the most striking differences are associated with the clear enhancement of NCO^- formation in potassium-(5-chlorouracil/5-fluoruracil) collisions and the fluorine anion formation (F^-) in potassium-(5-fluorouracil) collisions, which has never been reported in DEA experiments [78, 80]. An explanation regarding such formation in the current experiments will be given below.

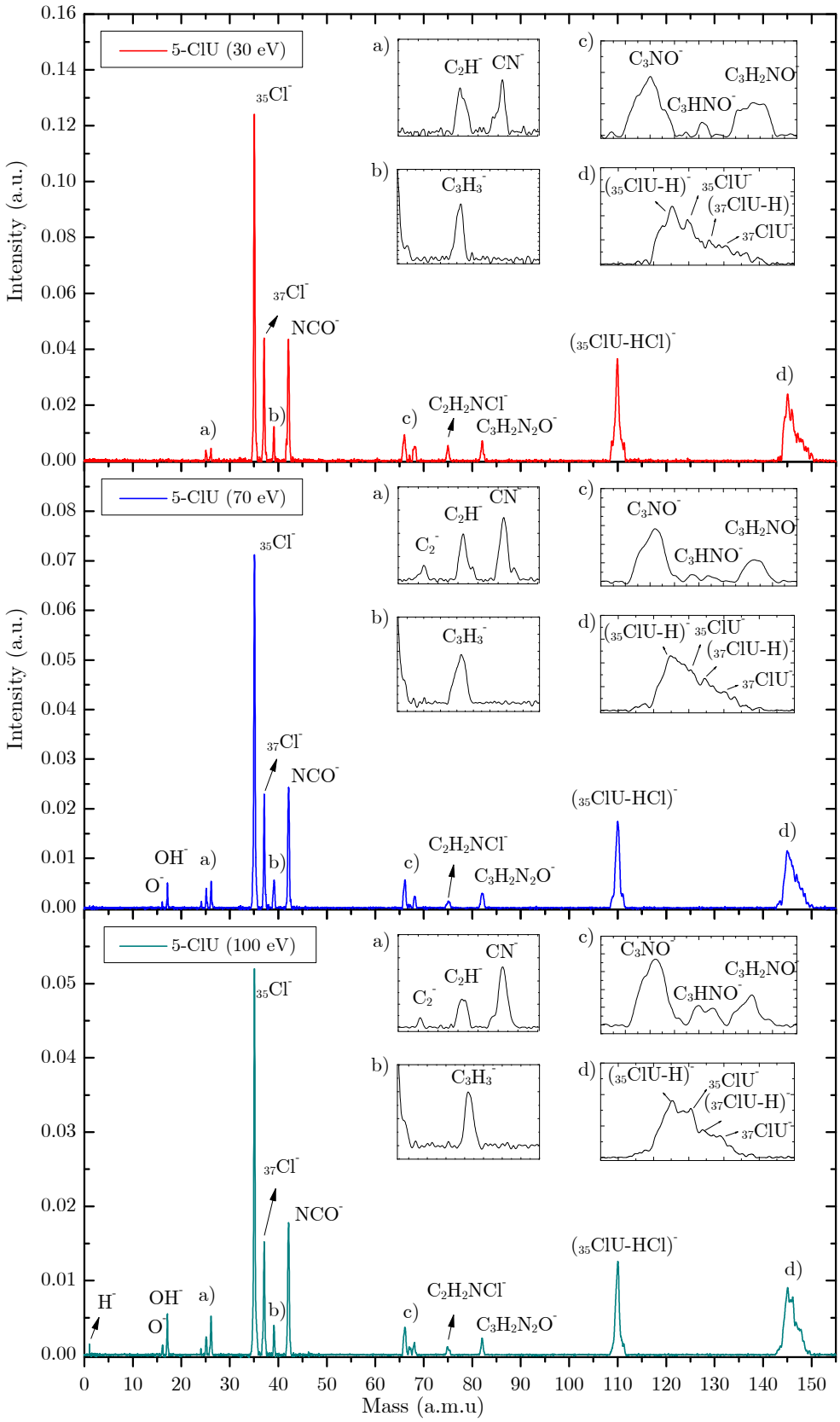

Figure 6.2 - 5-chlorouracil TOF anion mass spectra at three collision energies

Table 6.4 - 5-chlorouracil negative ions assignment and relative partial cross sections at several collision energies

		30 eV	70 eV	100 eV
Anion	Mass (a.m.u)	Partial Relative Cross Section (a.u.)	Partial Relative Cross Section (a.u.)	Partial Relative Cross Section (a.u.)
H^-	1	0	0	0.004
O^-	16	0	0.003	0.008
OH^-	17	0	0.025	0.033
C_2^-	24	0	0.004	0.002
C_2H^-	25	0.022	0.021	0.015
CN^-	26	0.020	0.030	0.032
$^{35}Cl^-$	35	0.763	0.477	0.344
$^{37}Cl^-$	37	0.262	0.126	0.098
$C_3H_3^-$	39	0.059	0.039	0.019
NCO^-	42	0.296	0.159	0.117
C_3NO^-	66	0.076	0.042	0.029
C_3HNO^-	67	0.005	0.002	0.007
$C_3H_2NO^-$	68	0.047	0.015	0.010
$C_2H_2NCl^-$	75	0.034	0.012	0.008
$C_3H_2N_2O^-$	82	0.049	0.026	0.014
(^{35}ClU-)-HCl^-	110	0.427	0.203	0.137
145/146/147/148	-	0.563	0.307	0.230

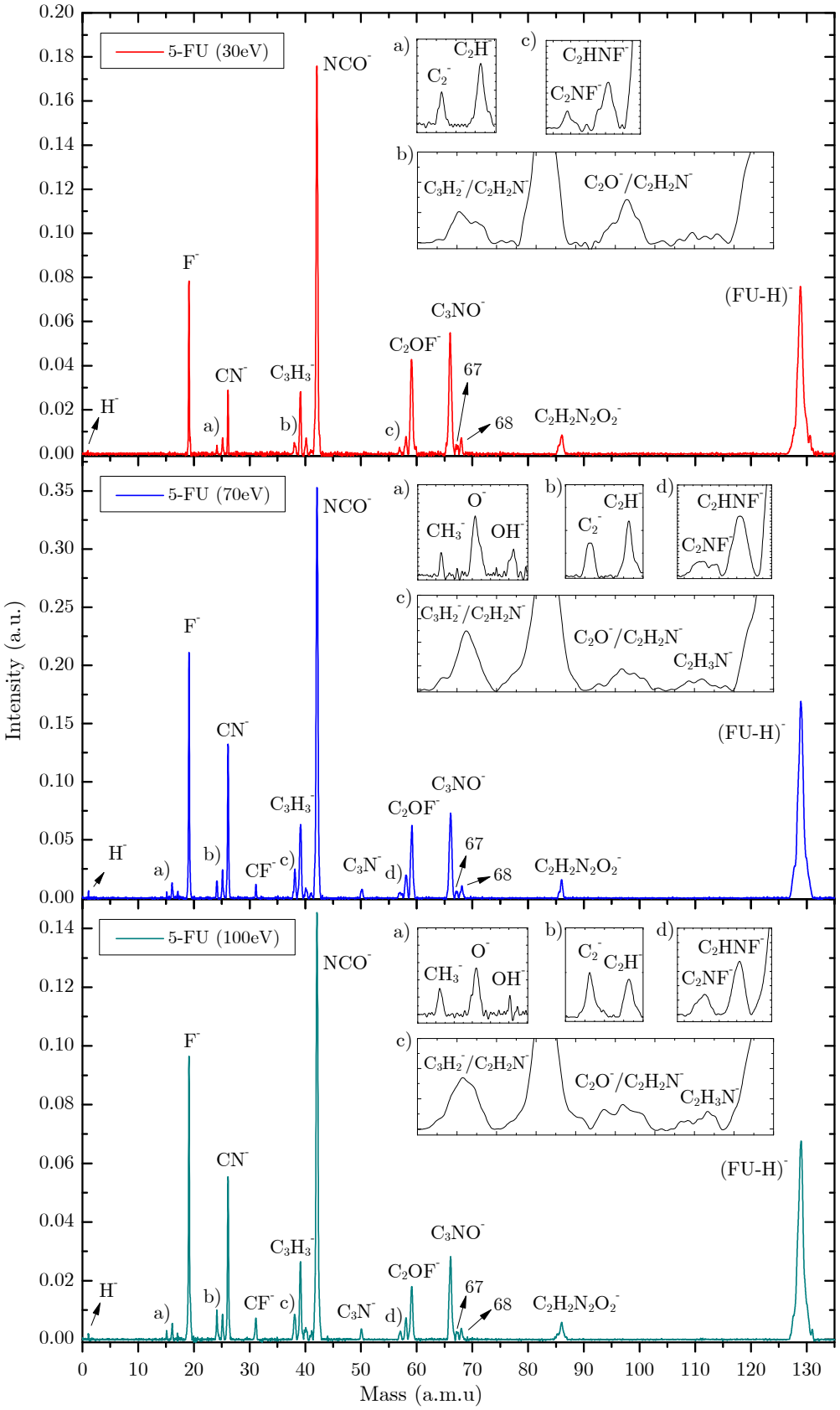

Figure 6.3 - 5-fluorouracil TOF anion mass spectra at three collision energies

Table 6.5 - 5-fluorouracil negative ions assignment and respective relative partial cross sections at several collision energies

		30 eV	70 eV	100 eV
Anion	Mass (a.m.u)	Partial Relative Cross Section (a.u.)	Partial Relative Cross Section (a.u.)	Partial Relative Cross Section (a.u.)
H^-	1	0.002	0.027	0.156
CH_3^-	15	0.000	0.011	0.311
O^-	16	0.000	0.085	0.825
OH^-	17	0.000	0.026	0.086
F^-	19	0.377	1.167	15.926
C_2^-	24	0.013	0.083	1.507
C_2H^-	25	0.036	0.129	1.336
CN^-	26	0.113	0.724	8.504
CF^-	31	0.000	0.047	1.170
$C_3H_2^-/C_2N^-$	38	0.033	0.147	1.609
$C_3H_3^-$	39	0.156	0.459	4.398
$C_2O/C_2H_2N^-$	40	0.039	0.053	0.850
$C_2H_3N^-$	41	0.000	0.013	0.283
NCO^-	42	1.133	2.364	27.165
C_3N^-	50	0.000	0.045	0.474
C_2NF^-/ CN_2OH^-	57	0.008	0.031	0.412
C_2HNF^-	58	0.044	0.141	1.056
C_2OF^-	59	0.339	0.446	3.405
C_3NO^-	66	0.439	0.569	5.541
C_3HNO^-	67	0.026	0.034	0.405
$C_3H_2NO^-$	68	0.034	0.064	0.451
$C_2H_2N_2O_2^-$	86	0.077	0.101	1.409
$C_4H_2FN_2O_2^-$	129	0.972	2.191	22.708

Table 6.6 - Anionic species formed following electron attachment and electron transfer to 5-chlorouracil (left) 5-fluorouracil (right).

Anion	M (a.m.u)	[77-78, 80-81]	This work
H^-	1	✓	✓
O^-	16	✓	✓
OH^-	17	×	✓
C_2^-	24	×	✓
C_2H^-	25	×	✓
CN^-	26	✓	✓
$^{35}Cl^-$	35	✓	✓
$^{37}Cl^-$	37	×	✓
$C_3H_3^-$	39	×	✓
NCO^-	42	✓	✓
C_3NO^-	66	×	✓
C_3HNO^-	67	✓	✓
$C_3H_2NO^-$	68	✓	✓
$C_2H_2NCl^-$	75	×	✓
$C_3H_2N_2O^-$	82	✓	✓
$(^{35}ClU\text{-}HCl)^-$	110	✓	✓
$C_4H_2N_2O_2{}^{35}Cl^-$	145	✓	✓
$C_4H_3N_2O_2{}^{35}Cl^-$	146	✓	✓
$C_4H_2N_2O_2{}^{37}Cl^-$	147	×	✓
$C_4H_3N_2O_2{}^{37}Cl^-$	148	×	✓

Anion	M (a.m.u)	[77-78, 80]	This work
H^-	1	×	✓
CH_3^-	15	×	✓
O^-	16	✓	✓
OH^-	17	×	✓
F^-	19	×	✓
C_2^-	24	×	✓
C_2H^-	25	×	✓
CN^-	26	✓	✓
CF^-	31	×	✓
$C_3H_2^-/C_2N^-$	38	×	✓
$C_3H_3^-$	39	×	✓
$C_2O^-/C_2H_2N^-$	40	×	✓
$C_2H_3N^-$	41	×	×
NCO^-	42	✓	✓
C_3N^-	50	×	✓
C_2NF^-	57	✓	✓
C_2HNF^-	58	×	✓
C_2OF^-	59	×	✓
C_3NO^-	66	×	✓
C_3HNO^-	67	✓	✓
$C_3H_2NO^-$	68	✓	✓
$C_2H_2N_2O_2^-$	86	×	✓
$C_4H_2N_2O_2^-$	110	✓	×
$C_4H_2FN_2O_2^-$	129	✓	✓
$C_4H_3N_2O_2F^-$	130	✓	×

→ (5-ClU-H)$^-$, (5-FU-H)$^-$ and 5ClU$^-$

According to DEA results [77, 80-81], the dehydrogenated parent anions are observed for both 5-FU and 5-ClU molecules. This is also the case for potassium-molecule collisions (Figure 6.2 and Figure 6.3), where these fragments are expected to be formed through the following reaction path:

$$K^0_{Hyper} + 5XU \rightarrow K^+ + 5XU^{\#-} \rightarrow K^+ + (XU - H)^- + H$$

Recent DEA results [77, 80] show that (5-ClU–H)$^-$ is mainly formed through resonances at 0, 0.070, 0.245 , 0.575, 0.960, 1.4 and 3.68 eV, while (5-FU–H)$^-$ at 0.560, 0.85, 1.28 and 1.5 eV.

Additionally, *Scheer et al.* have performed ETS studies as well as empty valence orbitals and dipole-bound properties calculations on uracil and halouuracils [60]. These studies have provided an interesting insight, especially when dealing with the molecular dissociation processes associated with the resonances observed in DEA experiments. In fact, *Scheer et al* . have proposed a mechanism for the dissociation process concerning the low energy sharp DEA resonances, which consists of a coupling of the dipole-bond state and the low lying σ^* resonances (VFRs) [60]. As mentioned in Chapter 5 , concerning uracil, the DEA resonances near 0.69 and 1.01 eV are attributed to the vibrational levels of the dipole bound state ν=2 and 3 [60], that will further couple with the $\sigma^*(N_1\text{-H})$ orbital, leading to dissociation. It would be also expected for the vibrational level ν=1 of the dipole-bound anion to appear near an electron impact energy of 0.34 eV, which is not observed in DEA because it lies below the asymptotic energy dissociation limit (U–H)$^-$ + H.

Because the dipole moments of the halouracils are identical to uracil, equivalent features are expected near these energies [60]. As such, the 5-chlorouracil DEA resonances located at 0.245 , 0.575 and 0.960 eV are attributed to the molecular transition to the dipole-bound vibrational states ν=1,2 and 3, respectively [60]. In this case, however, the $\sigma^*(N_1\text{-H})$ orbital will be strongly mixed with $\sigma^*(C_5\text{-Cl})$, which will cause higher anharmonicity of dipole vibrational levels, causing the energy deviation of equivalent vibrational levels of the U and 5-ClU dipole-bound states. The coupling between the $\sigma^*(N_1\text{-H})$ orbital and the low lying $\sigma^*(C_5\text{-Cl})$ orbitals allows not only for the appearance of the resonance attributed to dipole-bound vibrational state ν=1 (not seen for uracil) but also for opening additional decay channels for the VFRs, such as (ClU–Cl) and (ClU–HCl) that share some of the DEA ressonances [60]. For the higher resonances reported for the (5-Cl–H)$^-$ formation, located at 1.44 and 3.78 eV, it seems to be more clear [60], that they arise from the direct transition to the π_2^* and π_3^* valence states, which will further dissociate through coupling with a σ^* states.

By comparison with 5-chlorouracil, one might suggest that the 5-fluorouracil DEA resonances located at 0.56 , 0.85 and 1.28 eV might be assigned to transitions to dipole-bound vibrational states ν=2,3 and 4. In this case, one must assume that ν=1 is not observed because it lies below the

asymptotic energy separation into (Fluorouracil–H)$^-$ + H. Nevertheless, more theoretical support is necessary to verify this assumption. Additionally, the higher resonance reported for the (FU–H)$^-$ formation, located at ~1.5 eV, could arise from the direct transition to the π_2* [60], which will in turn be coupled with a σ* states, leading to dissociation.

In the present experiment, both ((5-ClU)–H)$^-$ and ((5-FU)–H)$^-$ are observed for the collision energies probed (30,70 and 100 eV). However, while ((5-ClU)–H)$^-$ formation seems to increase with decreasing collision energy, ((5-FU)–H)$^-$ formation presents a relative cross section maximum at 70 eV (see Figure 6.4). At this stage, is not yet clear which role can the positive potassium core take in regard to the VFR´s. However for the higher resonances (concerning initial transition to the π_2* and π_3* molecular orbitals) one would expect for the positive potassium core to provide extra stabilization against autodetachment, allowing these latter transitions to become enhanced and therefore to be the main source for the formation of the dehydrogenated negative ions of both halouracils. It would be very interesting to distinguish which amount of ((5-ClU)–H)$^-$ and ((5-FU)–H)$^-$ is being formed through VFRs and through σ* predissociation of the valence π* states. However, for the probed collision energies, the CM framework collision energy is more than enough to access both processes (Table 6.1) which makes at this time impossible to separate the relevance of either dissociation path over VFRs.

Concerning 5-ClU negative parent ion formation in atom-molecule collisions, one would expect to be formed through the following reaction channel:

$$K^0_{Hyper} + 5XU \rightarrow K^+ + 5XU^{\#-} \tag{5.1}$$

In the present experiments, the negative parent ion is only observed for the 5-ClU molecule and at all collision energies. However, due to the lack of TOF resolution at this mass range (146) it is difficult to estimate the relative cross section of 5-ClU$^-$, mainly because the corresponding mass peak is convoluted not only with the (5-ClU–H)$^-$ but also with the isotopic contributions ((5-^{37}ClU)–H)$^-$ and (5-^{37}ClU)$^-$ (Figure 6.2).

Although the TNI of both molecules is expected to be thermodynamically unstable [81], it appears that the lifetime of 5-ClU$^-$ is long enough to be detected by TOF, while 5-FU$^-$ is not observed, which is in close agreement to DEA results [78]. It seems that in this particular case, the presence of the positive potassium core does not provide enough stabilization of the 5-FU$^-$ with respect to DEA.

Cl^- and F^-

In DEA experiments with gas phase 5-chlorouracil [78, 80-81] the dominant channel reported with a cross section value a order of magnitude higher than the other fragments, was the formation of the halogen anion Cl^-, through the following reaction:

$$e^- + 5\text{–}ClU \rightarrow 5\text{–}ClU^{\#-} \rightarrow Cl^- + Uyl \quad , \tag{5.2}$$

Several resonances contributing to the formation of this fragment have been reported in DEA experiments, the most intense at ~0, 0.09, 0.270 eV [78] followed by two smaller contributions at 1.44 and 3.78 eV [81]. One of the most striking features of the DEA spectra [77-78, 80-81] is the presence of these rather sharp structures at very low energy, which occur at the same energy ~0, 0.09 and 0.270 not only for Cl^- but also for other fragmentation channels, namely $(5\text{-ClU–HCl})^-$ and $(5\text{-ClU–H})^-$. This could be a strong indication of different vibrational modes of a common state which in turn dictate the sort of fragmentation observed. The dissociation may therefore governed by a statistical behaviour.

Despite the fact that the observation of near-zero energy peaks in electron attachment, represents a subtle problem, *Li et al.* [83] DFT theoretical potential energy surfaces for the halouracils dehalogenation, along the C–X coordinate (X = F, Cl, Br and I), show that the lowest anion states have a mixed π* and σ* character, which could therefore be predissociated leading to X^-+U fragments [78]. However, one major point remains when considering the calculated energy thresholds for Cl^- formation (0.78 eV [83] and 0.83 eV [77]). These thresholds are higher than the already mentioned low energy resonances, namely ~0, 0.09 and 0.26 eV, which means that this model on its own cannot account for the DEA observed structures below these thresholds. Thus, it has been suggested that the near-zero eV structures could also arise from the presence of hot band transitions, which could considerably contribute to the ion signal even when considering only a moderate population of excited states [77]. However, to this date no further studies on halouracils have been performed in other to support this assumption.

On the other hand, as reported before in the discussion of the dehydrogenated parent anion, *Scheer et al.* [60] proposed that the structures at 0.09 and 0.270 eV could arise from vibrational Feshbach resonances (VFR), that is, excited vibrational levels of dipole bound states of this molecule. Indeed, as mentioned earlier, *Scheer et al.* proposed a mechanism for this dissociation process, via the coupling of the dipole-bound state and a $\sigma^*(N_1\text{-H})$, which was then shown to be strongly mixed with the $\sigma^*(C_5\text{-Cl})$ state [60]. This explanation appears to be fairly coherent with the fragments sharing these resonances. Additionally, *Sommerfeld's* [65] theoretical calculations further sustain the presence of suitable coupling mechanisms between dipole-bound and valence orbitals in 5-ClU. He has shown that near-zero energy electrons may attach to this molecule due to transitions to dipole-bound states, which can therefore be coupled with dissociative valence states (as is the case of the nitromethane parent anion formation [42]).

For Cl^- high energy resonances 1.44 and 3.78 eV, seems to be more consensual that they could arise from the direct transition to the π_2^* and π_3^* molecular orbitals [60, 78, 81], which can in turn be mixed with repulsive σ^* states leading to dissociation [60, 65]. Indeed, *Sommerfeld's* [65] theoretical PES calculation, on π^* and σ^* valence states of 5-ClU molecule along the C-Cl coordinate and their respective autodetachment times, further sustains that a direct transition to a σ^* valence state is unlikely to be responsible for dissociative processes (due to lower lifetime of this state with respect to autodetachment). Instead it is shown that efficient dissociative electron attachment seems only possible, if initially one of the two low π^* states is formed since both show a considerably longer autodetachment lifetime than the σ^* state. Thus, at the intersections, the π^* anion can hop onto the σ^* surface at a geometry where the autodetachment lifetime of the σ^* state is much longer [71].

As far as DEA results on 5-fluorouracil are concerned, it is interesting to note that, contrarily to other halouracils 5-ClU and 5-BrU [77-78, 80-81], no significant halogen anion F^- is formed. This is not entirely surprising since, considering the PES (C_5-X coordinate) shown in ref. [83]. The F^- formation at low energies seems from an energetic point of view to be less likely to occur in 5-FU in comparison to the formation of its analogue in the other halouracils (e.g. Cl^- in 5-ClU). Indeed, when taking a closer look at the PES shown in ref. [83], is possible to see that the minimum energy point of the $\sigma^*(C_5\text{-X})$ state is below the ground state of the neutral in the case of 5-ClU, in contrast to 5-FU. As such, from a simple energetic point of view (regardless of which intermediate states are involved), from the neutral state to the $\sigma^*(C_5\text{-X})$ state in the case of 5-ClU, the reaction is exothermic whereas in the case of 5-FU is endothermic. This could imply that at low energy electron attachment, the state $\sigma^*(C_5\text{-X})$ associated with the F^- anion formation may be blocked, thus precluding its formation. However, it is necessary to point out that the energy threshold associated with the infinite separation of the halogen anion from the rest of the molecule (i.e. energy threshold for X^- formation) is 0.78 eV for 5-ClU [83] and 2.15 eV for 5-FU[83], meaning that the "complete" halogen anion formation is an endothermic reaction for both 5-ClU and 5-FU. However, it is still to be answered which mechanism is indeed allowing for Cl^- to be formed at energies below the threshold. Nevertheless, one might suggest that whatever process is responsible for this anion formation (Cl^-), it is completely suppressed for F^-, most likely due to the significant difference in terms of the energy threshold for formation of these halogen anions. Despite the absence of F^- formation in DEA results at energies below 2.15 eV, it is rather puzzling why this fragment does not appear at higher energies, namely at ~4 eV where a valence π_3^* state is known to be present, as observed by ETS [60]. As such, one might suggest that, upon electron attachment to 5-FU, a transition from the neutral state to the π_3^* valence state is accessible, but due to fast autodetachment, no further dissociation mechanisms are allowed and thus no DEA structure is observed at this energy range regarding F^- formation.

In the present experiment, the collision K + 5-ClU produces mainly the halogen negative ion Cl^- for all three collision energies 100,70 and 30 eV (Figure 6.4), with relative cross sections of 0.44,

0.60 and 1.02 (Table 6.4), respectively (considering the sum of $^{35}Cl^-$ and $^{37}Cl^-$ contributions). In the collision K + 5-FU, the fluorine anion F^- is the second most intense fragment for energies of 100 and 70 eV and drops to the third most intense anion at 30 eV (Figure 6.4), with relative cross section of 0.61, 1.16 and 0.37 (Table 6.5), respectively.

One of the most striking features arising from the comparison between K+XU and DEA results is the fact that, in the case of K+5-FU collisions, the fluorine anion F^- is one of the most abundant fragments, which was never reported in DEA experiments. Taking into account that for the collision energies probed in the present thesis the "available" energy for electron transfer is always >15 eV (Table 6.1), all electron transfer processes discussed earlier (for DEA) are energetically accessible in K+XU charge exchange processes. This points towards the assumption that the presence of a third body (in this case K^+) may be responsible for not only inducing new fragmentation channels but for changing the cross sections values of the remaining anionic species.

Indeed, considering Sommerfeld's calculated lifetimes of the resonant states $\pi_2^*(C_5\text{-Cl})$ at ~1.44 eV and $\pi_3^*(C_5\text{-Cl})$ at ~3.78 eV for 5-chlorouracil, one can then suggest that the third body stabilization mechanism, suppresses autodetachment, thus allowing time for the electron to hop to the repulsive σ^* state. This leads to a significant increase in the Cl^- yield in K+ClU collisions. Despite the fact that the chlorine anion formation arising from the occupation of these states was previously observed in DEA[81], the positive potassium core could be accounted for enhancing this dissociative pathways associated with the aforementioned π^* states.

As far as 5-fluorouracil is concerned, from the present collisional results, it is rather evident that the presence of a third body (K^+) is allowing for the F^- fragmentation channel. F^- formation in charge exchange experiments could be assigned to a transition from the neutral to a valence $\pi_2^*(C_5\text{-F})$ or $\pi_3^*(C_5\text{-F})$ state of 5-FU molecule, much likely what is suggested to happen in 5-chlorouracil. These states were shown to exist in ETS experiments at similar energies as in 5-chlorouracil, and further to this, it seems also safe to assume that a similar coupling to a $\sigma^*(C_5\text{-F})$ may also exist. As such, the F^- formation in the context of atom-molecule collisions can be explained in a very similar way to the increased formation of Cl^-, i.e. the stabilization against autodetachment provided by the positive core K^+ allowing for an occupation of $\pi_2^*(C_5\text{-F})$ and $\pi_3^*(C_5\text{-F})$ long enough for the coupling with the $\sigma^*(C_5\text{-F})$ to occur, therefore resulting in an enhancement of the F^- yield. This common process is somewhat suppressed in free electron experiments due to the prevalence of autodetachment processes, making it impossible to be observable at any significant DEA structures in this energy range.

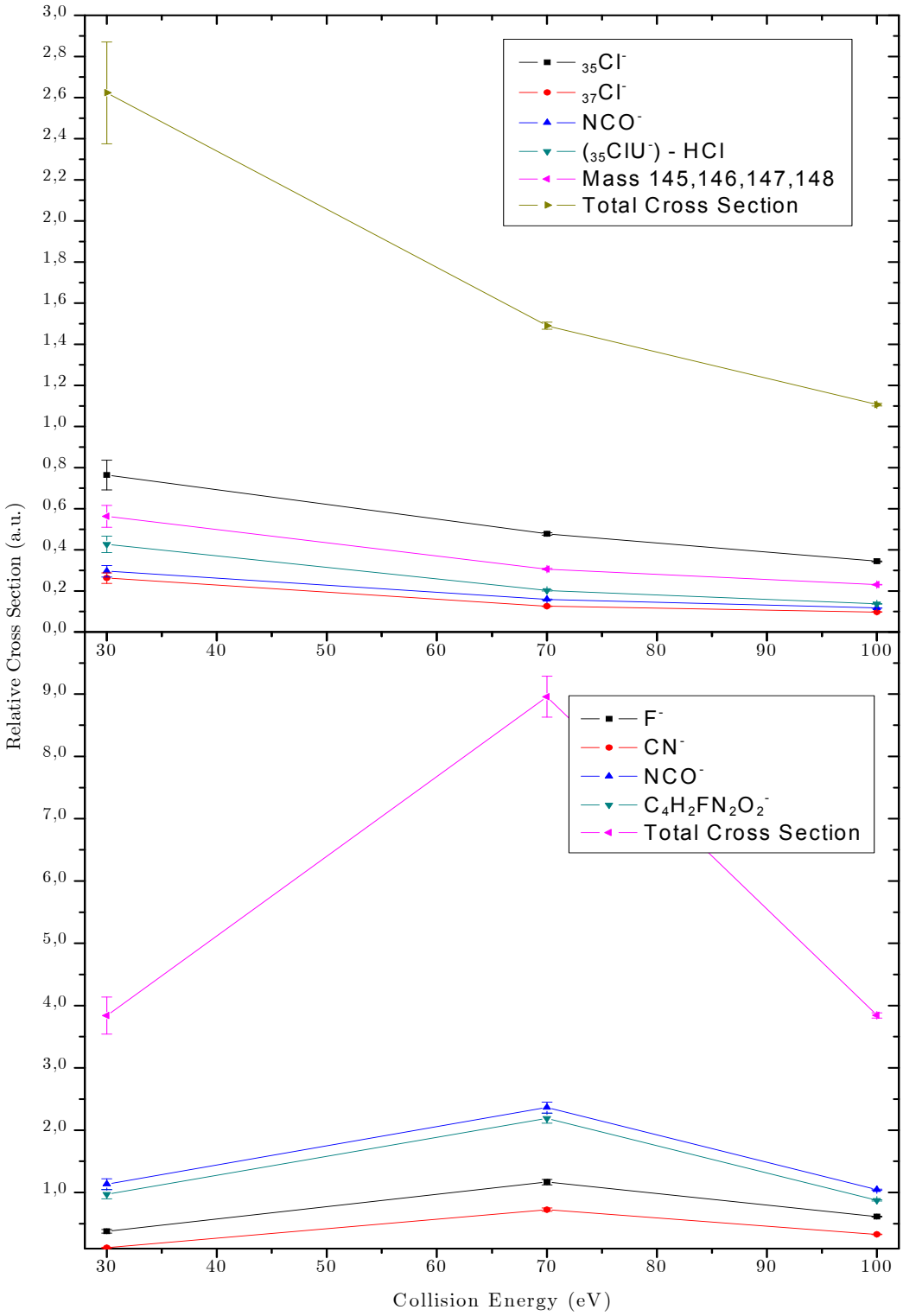

Figure 6.4 - 5-chlorouracil (upper figure) and 5-fluorouracil (lower figure) partial cross sections

As show in Figure 6.4, Cl^- formation increases for lower collisions energies, which is not entirely surprising considering that the collision time, i.e. time between the first and the second crossing of the ionic and covalent PES, is expected to be higher for lower collision energies. Assuming

that this fragment is mainly produced through the process described above, a higher collision time will allow for the enhancement of the dissociative pathway, by more efficiently precluding autodetachment. Nevertheless, this is not the case for F^-. When looking at the relative cross section trending for F^- formation as a function of the collision energy (Figure 6.4), is possible to see that it shows a maximum at 70 eV and not for the lower collision energy (at 30 eV). Unfortunately, there is it not enough theoretical support available at this point to fully understand the mechanisms associated with this behaviour.

→ NCO^-

Contrarily to the previously discussion, NCO^- formation requires ring fragmentation, involving therefore cleavage of several ring bonds and making this fragment formation a far more complex process. In the present experiments, NCO^- is one of the most abundant species formed for both the fragmentation of the 5-halouracils, being the most intense fragment in K+5-FU collisions with relative cross section of 1.04, 2.36 and 1.13 (Table 6.5) for collision energies of 100,70 and 30 eV, respectively (Figure 6.4). In the collisions of K + 5-ClU , NCO^- is one of the most abundant fragment for all collision energies 100, 70 and 30 eV (Figure 6.4), with relative cross section of 0.12, 0.16 and 0.30 (Table 6.4), respectively.

In recent DEA experiments [80-81] on 5-ClU, NCO^- shows resonances centred around 1.4, 3.5, 5.2 and 6.5 eV, where 3.5 eV shows the highest cross section value. As reported before, the resonances at 1.4 eV and 3.5 eV have been assigned to the LUMOs π_2^* and π_3^* [60, 78, 81]. Moreover, it is interesting to note that the other dominant fragmentation channels also show similar DEA structures around the same energy values, namely at ~1.4 eV [$((5\text{-ClU})\text{-HCl})^-$, $((5\text{-ClU})\text{-H})^-$, $((5\text{-ClU})\text{-HCl})^-$, Cl^-, C_3HNO^-, $C_3H_2NO^-$, $C_3H_2N_2O_2^-$] and ~3.5 eV [Cl^-, C_3HNO^-]. This may be a strong indication that, following the occupation of these states (π_2^* and π_3^*), several dissociative paths are available and thus the formation of these fragments are competitive.

As far as DEA results on 5-FU are concerned, NCO^- shows resonances centred at 2, 4.3, 6.2 and 7 eV, where the 4.3 eV shows the highest cross section value. Despite the fact that less information is available for this molecule, it is possible to see that, once again, the lower energy resonances are "shared" between several fragmentation channels (~2 eV[$((5\text{-FU})\text{-H})^-$, $H_2C_3NO^-$] and ~4.3[$H_2C_3NO^-$,CN^-])[80]. Furthermore, following ETS experiments and considering the structural similarity between 5-FU and 5-ClU, the resonances at ~2 and ~4.3 eV can be tentatively assigned to the occupation of π_2^* and π_3^*.

Following the previous explanations on NCO^- formation in Chapter 5 , one may suggest that the presence of the positive core K^+ can be responsible for forcing a longer occupation of these states

(π_2* and π_3*), by precluding autodetachment and allowing enough time for the coupling with a repulsive state to occur. In this particular case, the coupling is expected to occur with a dissociative σ* state on the ring coordinates (see chapter 5) and not on C_5-X coordinate (responsible for the halogen anion formation, as discussed above). So, while the initially occupied π_2* and π_3* states may be shared between the dominant fragments, NCO^- formation may relies on a coupling to different σ* states.

In fact, our experimental results seem to further sustain this assumption. A closer look at the relative cross section for NCO^- formation in K+5-ClU collisions , shows that despite the fact that this fragment is not the most abundant, it has cross section values of the same order of magnitude of the most dominant fragmentation channels for all collision energies studied. In contrast, as far as DEA results are concerned, NCO^- formation cross section value is two orders of magnitude lower than the value for Cl^- formation. Despite the fact that an equivalent comparison is not possible for 5-FU (F^- is not formed in DEA), one may point out that NCO^- is the most abundant fragment in K+5-FU, which is not the case in DEA experiments [80], where the most abundant fragment is $((5\text{-FU})\text{-H})^-$. It seems therefore likely that K^+ could indeed be enhancing NCO^- formation in both molecules, with respect to free electron experiments. Although the NCO^- and X^- formation may arise from the same parent states (π_2* and π_3*) in K+5-XU experiments, it seems that this competitive process is behaving differently in each of the studied halouracils. The NCO^- fragmentation channel seems to overcome the F^- formation in K+(5-FU), while the opposite seems to occur in K+(5-ClU) , as Cl^- is more abundant than NCO^-.

Indeed, the different nature of the halogen atoms in these molecules, namely their sizes, may have an important effect, not only in the energy of the valence states but more importantly in the coupling probability between the "parent" π_2* and π_3* states and the different repulsive σ* states responsible for the dissociation channels. On the other hand, as reported in DEA studies, Cl^- formation could also arise from the occupation of near-zero energy states (presumably through dipole-bound states), whereas F^- formation seems not to occur. Assuming that the presence of a third body K^+ has little effect in these dipole-bound states formation probabilities, it is possible that, in K+(5-ClU) collisions, Cl^- is being formed through the occupation of both π* higher energy valence states (as described above) and near energy dipole-bound states, while F^- formation is only obtained through occupation of π* higher energy valence states. This could also justify the predominance of Cl^- over NCO^- (in 5-ClU), in contrast to the predominance of NCO^- over F^- (in 5-FU). At this point, however, it is not possible to be sure of what is indeed the mechanism responsible for the different behaviour observed in the relative cross sections of the X^- and NCO^- for the different 5-halouracils studied.

6.4 Conclusions

The fragmentation patterns of 5-chlorouracil and 5-fluorouracil obtained upon collisions with free electrons and potassium atoms have revealed to be significantly different from each other. A first general conclusion can be made by looking at the general fragmentation pattern of the presented spectra. It seems likely that, in the context of atom-molecule collisions, the yield of fragments that require ring-breaking (e.g. NCO^-, C_3NO^- $C_2H_2N_2O_2^-$) are greatly enhanced, judging from the absolute cross sections obtained in DEA studies, where some of these fragments have cross sections two orders of magnitude lower than the most intense fragment Cl^-. While some of these less intense fragments may worth of discussion, not much information surrounding the several accessible states exists thus unabling any discussions to be performed.

Concerning 5-chlorouracil, the major point of disparity with DEA is the enhanced formation of the ring breaking fragments, especially NCO^-, similar to what happens in thymine and uracil. Indeed, in atom-molecule collisions NCO^- is the second most abundant fragment for all the collision energies probed (following the formation of Cl^-). In opposition, DEA results show cross section values for NCO^- formation one order of magnitude below the Cl^- formation. As such, and following the reasoning made for NCO^- formation for thymine and uracil, it was suggested that the presence of a third body (K^+) in atom-molecule experiments is responsible for enhancing the occupation of the π_2^* and π_3^* states by precluding autodetachment and allowing time for the coupling with the repulsive σ^* states.

As far as 5-fluorouracil is concerned, the main difference lies in the formation of F^- which, is exclusively obtained through initial access to the higher energy π_2^* and π_3^* states which in turn, due to the presence o the K+, are allowed time to couple with the dissociative σ^*(C-F) state.

From a more general point of view, it is therefore clear that for both 5-chlorouracil and 5-fluorouracil, the π_2^* and π_3^* states may be the mainly accessed states and that the formation of the different fragments lies on a competitive process of coupling with other several σ^* states existing in several parts of the pyrimidine ring.

It is necessary to note that all the reasoning presented in this chapter, as well as in the previous chapter (chapter 5), while being coherent and supported by other studies will ultimately need posterior unambiguous validation. In order to do this, extensive calculations are required. These calculations however are of great complexity and therefore were not attempted both during the course of the work presented herein, nor during the writing up of this thesis.

In conclusion, when comparing the results of thymine/uracil with halouracils, the substitution of the halogen in the C_5 site significantly changes the accessible states, and therefore the resulting fragmentation channels. In particular, the formation of the halogen anion which appears as one of the most intense fragments in both halouracils, whereas in thymine and uracil, the formation of the

corresponding fragment (CH_3^- and H^-) is either absent (in the case of thymine) or at most residual (in the case of uracil). The production of the halogen anion can have interesting consequences in terms of the role of these molecules as radiosensitisers. This will be discussed in Chapter 7 below.

Chapter 7 Conclusions and Future work

The main goal of this thesis was to investigate the negative ion formation through electron transfer processes to isolated DNA basis and halouracils in atom-molecule collisions. In order to achieve such attempt, we have developed a suitable cross molecular beam experimental set-up. Though the work presented in this thesis can be divided into two main categories. The first is associated to the development and improvement of the experimental set-up, the second to performing and obtain a set of experimental results. In order to make a clear distinction between both, they will be addressed separately, in which a work summary (and associated conclusions) will be given. In addition, some suggestions to future work will be addressed.

7.1 Experimental setup

In order to study the negative ion formation in electron transfer processes between a neutral potassium beam and isolated (gas-phase) biological relevant molecules, a crossed molecular beam experimental set-up was developed. This has been successfully accomplished.

The development of such system was a multistage process, which began with the refurbishment and adaptation of a two chamber vacuum system, followed by the improvement of a neutral potassium beam source and the development of a biomolecule's oven, both critical components for the production of the beams. Additionally, in order to measure the negative fragmentation resulting from the atom-molecule collisions, a TOF mass spectrometer was both developed and implemented.

In the course of the experimental work several technical skills were acquired. Among others, it is important to mention technical drawing, electronic and workshop experience acquired and also the development of computer software applications to manage the acquisition and control systems.

7.2 Experimental results

In this section a brief summary of the most relevant experimental results will be presented, covering mainly the data on thymine, uracil and the two 5-halouracils studied in this thesis. As we had

a chance to say before, nitromethane is just briefly mentioned due to its relevance as a calibration molecule in our TOF mass spectrometer.

7.2.1 Nitromethane

Measurements on nitromethane were initially meant for calibration purposes only, especially because its negative ion formation had previously been reported in atom-molecule collisions [27]. However, due to the relatively increased TOF resolution of the present set-up (~m/Δm 120) in contrast to Lobo *et al*. [27], additional fragmentation channels were observed, unveiling interesting results. Even though this molecule is not directly related to biological processes concerning electron induced DNA damage, the discussion on the nitromethane results was important to better ascertain dissociation mechanisms subsequent to the electron transfer process into biological related molecules.

The nitromethane negative ion formation, arising from the collision with neutral potassium atoms was probed at three collision energies defined within a laboratory framework: 30, 70 and 100 eV. In terms of the available energy in the CM, these are equivalent to 16.3, 38.0 and 54.2 eV, respectively. The resulting TOF mass spectra were recorded, and the relative cross section for the fragmentation channels obtained. Comparatively to previous results [27], where only three anionic fragments were observed, in this study was possible to detect nine fragmentation channels. Furthermore and in close agreement with the previous results, the most intense mass peaks were assigned to the formation of NO_2^-, O^- and the parent anion $CH_3NO_2^-$.

In addition, by making use of deuterated nitromethane, it was possible to unambiguously assign the 17 a.m.u anion, previously assigned and proposed to be due to O^- formation through internal isomerisation followed by dissociation, to OH^- formation.

In these charge transfer experiments, was also possible to observe the formation of the negative parent anion, which was never reported in DEA experiments. That is not particularly surprising due to its positive electron affinity. However, such may be possible in a three body interaction due to the stabilization effect provided by the positive potassium core. In fact, following the electron transfer, the TNI may be left in a vibrationally excited state, which due to the presence of K^+ is allowed to relax into a vibrational state below the ground state of the neutral, creating a long lived parent anion. In contrast, in DEA experiments the TNI is more likely to undergo autodetachment and no stable negative parent anion is therefore formed.

The potassium positive core can also have an important role in the formation of the anionic fragment NO_2^-. This fragment, despite the fact of being the most abundant species produced (for all the collision energies probed), is shown to have a pronounced increase in terms of relative cross section at 30 eV. For smaller collision energies, the collision time may be large enough to enable the

molecular behaviour of the target molecule, meaning that bound stretching effects can occur (C-N coordinate) allowing for the formation of NO_2^- through channels that were otherwise unavailable.

7.2.2 Thymine and Uracil

The DNA molecule is known to be particularly susceptible to damage induced by secondary electrons produced by the interaction of the incident ionising radiation with living tissue. In this context, experiments of electron transfer to isolated DNA and RNA constituents are presented to complement the available studies on DEA experiments, aiming to better understand the molecular processes associated with DNA damage occurring in the physiological environment and that can be described at the molecular level.

In this thesis, a neutral potassium beam was used to study the electron transfer and subsequent negative ion formation of the isolated DNA base - thymine and its analogue in RNA – uracil. Both molecules were probed for three different collision energies: 30, 70 and 100 eV (laboratory framework). In terms of available energy in the CM these energies are equivalent to 16.3, 38.0 and 54.2 eV (for thymine) and 19.8, 46.1 and 65.9 eV (for uracil). This energy dependence study was intended not only to understand the influence of the available energy in terms of anionic fragmentation pattern, but more importantly to probe on the effects of the collision time on such target molecules.

The experimental results concerning potassium-thymine/uracil collisions have shown that the most abundant anionic species produced a fragmentation pattern with similar anions: NCO^- followed by the dehydrogenated parent anion ($(T\text{-}H)^-$/$(U\text{-}H)^-$), the former requiring a complex mechanism in the unimolecular decomposition of the TNI by cleavage of several bonds in the molecular ring structure. The identical behaviour in terms of fragmentation pattern was not entirely surprising, further to the structural similarity between thymine and uracil. Furthermore, it was also possible to observe that in terms of the total relative cross sections, the anionic fragmentation probability increased for lower collisions energies, pointing towards the fact that the potassium core is indeed capable of inducing more significant changes to the fragmentation intensity when spending more time near the TNI.

When comparing the relative intensities of the anions with the results from DEA experiments, a major difference is clearly observed. While in atom-molecule collisions the most abundant anionic species produced is NCO^- (for all the collisions energies probed in this thesis), in DEA the most abundant fragment is $(T\text{-}H)^-$/$(U\text{-}H)^-$, with all other fragments having cross sections approximately one order of magnitude lower [10]. Therefore, we suggest in this thesis that the greatly enhanced relative anion yield of fragments that require the breaking of the ring (such as NCO^-) could be attributed to the presence of the third body (K^+). Due to the strong relevant coulombic interaction between K^+ and the TNI, autodetachment suppression may be relevant, therefore allowing sufficient time for an electron

transfer from an otherwise unstable (with respect to autodetachment) orbital to the ring-breaking σ* orbitals to occur (for details see Chapter 5).

Assuming that atom-molecule collisions may indeed, in comparison to DEA experiments, be a more suitable approximation to electron transfer within DNA basis in biological environment, the experimental results in this thesis point towards slight changes in how electron-induced damage to DNA bases has been established. From a free electron attachment point-of-view, the main effect of the secondary electrons is the production $(T\text{-}H)^-/(U\text{-}H)^-$, which does not (directly) require a complete molecular breakdown and hence do not necessarily lead to SSB's. Although the dehydrogenated parent anion formation yields an extremely mobile H radical, which may be extremely reactive and potentially harmful to molecules in the vicinity of the DNA/RNA bases, it is important to note that while the H abstraction mainly occurs from the N_1 position, which in the DNA/RNA molecule is connected to the sugar backbone unit, no biological relevance should be discussed. However, if the H abstraction occurs from the N_3 position, considerable biological implications can be yielded.

However, the results presented herein suggest that these secondary electrons, rather than mainly forming the dehydrogenated parent anion, will mostly lead to extensive damage to the ring structure of thymine and uracil (required to form NCO^-, among others) and therefore greatly enhance the possibility of single and double strand breaks. In conclusion, although it is not possible to make a quantitative comparison between the results herein reported and DEA, these atom-molecule experimental results may expect to point out that a unidimensional analysis of the electron-induced damage relying exclusively on DEA studies may underestimate the true damage capability of these secondary electrons. Furthermore, the extensive nature of the damage that results from ring breaking may be more complex to repair than the damage that results from hydrogen abstraction, which in the physiological environment is exclusive to the N_3-H bond.

7.2.3 Chlorouracil and fluorouracil

Halouracils have long been proposed as radiosensitizers, which are molecules that have the ability of making tumoral cells more sensitive to radiation therapy. Some of the cellular damage is indeed produced directly by the ionising radiation but, as it was recently shown [6], the majority of the DNA damage may be associated with secondary species formed after the cellular irradiation, especially by secondary electrons. As such, experiments on electron transfer to halouracils were presented to probe in which way 'bound' electrons can induce molecular damage and how the damage is indeed more severe than that operated by secondary electrons in isolated DNA/RNA basis.

Electron transfer experiments were conducted on two widely known halouracils, 5-chlorouracil (5-ClU) and 5-fluorouracil (5-FU). Both molecules were probed for three different

collision energies: 30, 70 and 100 eV (laboratory framework), which in terms of available energy in the CM are equivalent to 21.1, 49.2 and 70.2 eV (for 5-chlorouracil) and 20.5, 47.9 and 68.5 eV (for 5-fluorouracil).

Regarding the energy dependence of the total relative cross sections, was observed that for 5-chlorouracil the total anion yield increased for smaller collision energies, especially when going from 70 to 30 eV. In contrast, the 5-fluorouracil experimental results have shown a pronounced increase in terms of total partial cross section when going from 100 to 70 eV and when going from 70 to 30 eV a small decrease. This is in contrast to other molecules that were investigated during the course of the work herein reported. We could not find an explanation for this behaviour yet.

As far as negative ion formation is concerned, 5-chlorouracil results show that the most abundant species (for all collision energies) have been assigned to Cl^-, $(ClU\text{-}HCl)^-$ and NCO^-. It was also possible to observe the formation of the negative parent ions ($^{35}ClU^-$; $^{37}ClU^-$) and the dehydrogenated parent ions (($^{35}ClU\text{-}H)^-$;($^{37}ClU\text{-}H)^-$), which were somewhat convoluted due to limitations in the resolution of the TOF spectrometer. On the other hand, experimental results concerning 5-fluorouracil show that the most abundant anionic species (also for all collision energies) have been assigned to NCO^-, $(FU\text{-}H)^-$ and F^-. In addition, no evidence of a stable negative parent ion $(FU)^-$ was detected. These results lend themselves to a similar conclusion as it was reported for thymine and uracil, i.e. the presence of the third body greatly changes the dominant fragmentation patterns. Indeed, as was the case for thymine and uracil, the fragmentation patterns reported herein greatly differ from those in DEA studies. For 5-chlorouracil, as far as DEA studies are concerned, the dominant fragmentation consists of Cl^- formation, followed by the $(ClU\text{-}HCl)^-$ anion, with significant yields of ClU^- and $(ClU\text{-}H)^-$ [81]. However, in the present studies, while the formation of Cl^- is also the main fragment, ring breaking fragments are greatly enhanced, particularly yielding NCO^-, which now appears as the second most intense fragment. Once again, although absolute comparisons between DEA yields and atom-molecule collisions yields are not possible, it is however possible to assume that, within the context of atom-molecule collisions, the damage to the structural integrity of this molecule is much more likely to occur than what would be expected from a single DEA point of view.

Regarding 5-fluorouracil, the picture is even more dissimilar. In DEA studies, the main fragmentation consists of $(5\text{-}FU\text{-}H)^-$, followed by NCO^- but most importantly no F^- formation is reported. In atom-molecule collisions however, NCO^-appears as the main fragment, followed by F^- and $(5\text{-}FU\text{-}H)^-$ formation. At this point, a major feature lends itself to a more thorough discussion. The unprecedented formation of F^- can have significant consequences in terms of the role of this molecule as a radiosensitiser. As was discussed by Abdoul-Carime *et al*. [11], the high yield of the halogen anion entails a high yield of the corresponding (U-yl) radical, which is known to be highly reactive and therefore associated with the formation of single and double strand breaks [11]. This is particularly relevant in the case of 5-fluorouracil since in the presented studies, there is formation of F^-

and hence (U-yl) radical formation. This reasoning also holds for Cl^- formation in the case of 5-chlorouracil.

In conclusion, the results presented in this thesis appear to reinforce the role of halouracils as effective radiosensitisers. Although we cannot quantitatively compare the cross section values between the 5-chlorouracil/5-fluorouracil and thymine/uracil, it is clear from the presented data that the halogen substitution at the C_5 site results in the appearance of new fragments, particularly the formation of the halogen anion, which becomes one of the dominant channels. Thus, in addition to the ring breaking fragments that are shared with thymine and uracil, new fragmentation channels arise for halouracils. These fragmentation channels are not only important (Cl^-/F^- formation) but some of the complementary fragments may also be very effective at inducing structural damage to other nearby molecules, owing to the high electron affinity of some of these fragments (e.g. (U-yl) radical).

7.3 Future work

In the present experimental results, a quantitative comparison between anion yields was only possible between spectra of the same molecular target (at different collision energies). For a particular molecule, if the biomolecule's oven temperature is kept constant, it is possible to assume that the target beam intensity remains the same throughout the measurements. Unfortunately, when comparing results from different molecules such procedure is no longer valid unless the vapour pressures of the molecules are the same. This limitation is due to an absence of a system to measure the target beam intensity. As such, the development of a detector to measure the target beam intensity is in order. By implementing this improvement it will be possible, for example, to understand if indeed 5-ClU and 5-FU have higher anionic formation yields than thymine or uracil.

As far as the collision energy is concerned, it would be interesting to reduce the "available" energy (CM framework) to values where the formation of particular fragmentation channels is blocked. By doing so, it could be easier to identify the TNI resonant states associated with the formation of particular anionic species. This can be accomplished in three ways: 1) decreasing the mass of the target molecule; 2) changing the alkali atom source (e.g. caesium instead of potassium); 3) decreasing the acceleration voltage of the ionic alkali beam. However, when the energy of the alkali beam is decreased below ~20 eV, the neutral potassium beam intensity is dramatically reduced, making it very difficult to detect the anionic fragmentation resulting from the atom-molecule collisions. To overcome this problem, there are several possibilities: implementing a set of focusing lenses between the potassium positive ion source and the charge exchange oven, a better focused neutral beam can be achieved and therefore an increase in effective intensity is obtained. In addition,

or alternatively, the entire system responsible for producing the neutral potassium beam could be placed closer to the collision centre.

In order to better probe the fundamental mechanisms surrounding atom-molecule collisions, studies of the energy loss of the potassium cation will provide information regarding the electronic excitation of the target. Additionally, measurements of total and differential cross sections of the scattered K^+ can also be performed, thereby obtaining additional understanding of the collision dynamics with the particular attention to the scattering process. In practice, these measurements require the implementation of an energy analyser, which would require an extensive change of the collision chamber, together with the implementation of the analyser.

Other interesting research activities can include extending the collision energies to higher values where formation of positive ions is likely to occur. Such cations' formation should also give relevant information on the collision induced dissociation with the particular attention to momentum transfer and probably pointing towards an increase of excited neutrals.

An urgent need for suitable theoretical support was repeatedly noticed during this work, namely because the most commonly used theory to describe charge exchange processes (Landau-Zener model) is more suited for a direct comparison with atom-atom or, at most, atom-diatomic experiments. In the case of the molecular systems studied in this thesis, all the molecules probed are of polyatomic nature, making the study of collision dynamics a potentially very difficult problem to address. In fact, the interpretation of such atom-molecule collision is hampered by the fact that, in opposition to atom-atom collisions, several covalent (K+M) and ionic states (K^++M^-) have to be considered.

In regard to further molecules to be studied with this technique, two distinct experimental directions may be followed. If, in fact, the main goal is to better understanding the fundamental collision dynamics of charge exchange transfer processes and the resulting anionic formation, then simpler and smaller molecules should be probed. It is worthy to note that the pioneering studies surrounding charge transfer processes with alkali beams were mainly restricted to diatomic molecules or diatomic-like molecules, such as nitromethane, since the complexity of studying larger molecules proved to be somewhat restrictive.

On the other hand, if the intention is to study the effect of 'bound' electron transfer to biological relevant molecules (mainly in terms of anionic fragmentation), then other DNA molecules should be studied, gradually increasing the complexity of the probed molecules. Indeed, studies of thymidine are currently being undertaken in our laboratory.

Finally, obtaining absolute cross sections for these processes is very useful not only from a purely fundamental point of view but also for comparison purposes since these absolute cross sections can be used to directly determine if indeed these results show higher cross section values than in DEA.

References

1. Sonntag, C.v., "*The chemical basis of radiation biology*". 1987, London: Taylor & Francis
2. Ward, J.F., "*Advances in radiation biology*", ed. J.T. Lett and H. Adler. Vol. 5. 1977, New York ; London: Academic Press,181-239.
3. Fuciarelli, A.F.E. and J.D.E. Zimbrick, "*Radiation damage in DNA : structure/function relationships at early times : International workshop : Papers*". 1995, Columbus, Ohio: Battelle Press
4. Sanche, L., "*Low energy electron-driven damage in biomolecules*". European Physical Journal D, 2005. 35(2), 367-390.
5. Cai, Z.L., P. Cloutier, D. Hunting, and U. Sanche, "*Comparison between x-ray photon and secondary electron damage to DNA in vacuum*". Journal of Physical Chemistry B, 2005. 109(10), 4796-4800.
6. Boudaiffa, B., P. Cloutier, D. Hunting, M.A. Huels, and L. Sanche, "*Resonant formation of DNA strand breaks by low-energy (3 to 20 eV) electrons*". Science, 2000. 287(5458), 1658-1660.
7. Lehnert, S., "*Biomolecular action of ionizing radiation*". Series in medical physics and biomedical engineering. 2008, New York: Taylor & Francis
8. Aldrich, J.E., K.Y. Lam, P.C. Shragge, and J.W. Hunt, "*Fast Electron Reactions in Concentrated Solutions of Amino-Acids and Nucleotides*". Radiation Research, 1975. 63(1), 42-52.
9. Illenberger, E. and J. Momigny, "*Gaseous molecular ions : an introduction to elementary processes induced by ionization*". Topics in physical chemistry,. 1992, Darmstadt, New York: Springer-Verlag
10. Denifl, S., S. Ptasinska, M. Probst, J. Hrusak, P. Scheier, and T.D. Mark, "*Electron attachment to the gas-phase DNA bases cytosine and thymine*". Journal of Physical Chemistry A, 2004. 108(31), 6562-6569.
11. Abdoul-Carime, H., M.A. Huels, E. Illenberger, and L. Sanche, "*Sensitizing DNA to secondary electron damage: Resonant formation of oxidative radicals from 5-halouracils*". Journal of the American Chemical Society, 2001. 123(22), 5354-5355.
12. Kleyn, A.W., J. Los, and E.A. Gislason, "*Vibronic Coupling at Intersections of Covalent and Ionic States*". Physics Reports-Review Section of Physics Letters, 1982. 90(1), 1-&.
13. Murrell, J.N. and S.D. Bosanac, "*Introduction to the theory of atomic and molecular collisions*". 1989, Chichester ; New York: J. Wiley
14. Lawley, K.P., "*Molecular scattering : physical and chemical applications*". Advances in chemical physics v. 30. 1975, London ; New York: Wiley
15. Limao-Vieira, P., "*Fragmentação de Iões Negativos de Halobenzenos Induzidos por Colisão*", in *Physics*. 1999, Universidade Nova de Lisboa: Lisboa
16. Olson, R.E., F.T. Smith, and E. Bauer, "*Estimation of Coupling Matrix Elements for One-Electron Transfer Systems*". Bulletin of the American Physical Society, 1970. 15(11), 1506-&.
17. Kleyn, A.W., "*Vibronic Excitation in Atom Molecule Collisions*",154
18. Kendall, G.M. and R. Grice, "*Vibrational Coordinates in Electron Jump Model*". Molecular Physics, 1972. 24(6), 1373-1382.
19. Bernstein, R.B., "*Atom-molecule collision theory : a guide for the experimentalist*". Physics of atoms and molecules. 1979, New York: Plenum Press

20. Baer, M., "*Beyond Born-Oppenheimer : electronic non-adiabatic coupling terms and conical intersections"*. 2006, Hoboken, N.J.: Wiley

21. Maneira, M.J.P., "*Formação de pares de iões em colisões entre átomos e moléculas"*, in *Physics*. 1984, Univesidade Nova de Lisboa: Lisboa

22. HeatWaveLabs, "*TB-118 Aluminosilicate Ion Sources Specifications"*. 2002

23. Cotter, R.J., "*Time-of-flight mass spectrometry : instrumentation and applications in biological research"*. ACS professional reference books. 1997, Washington, DC: American Chemical Society

24. Gross, J.H., "*Mass spectrometry : a textbook"*. 1st ed. 2006, New York: Springer

25. Wiley, W.C. and I.H. Mclaren, "*Time-of-Flight Mass Spectrometer with Improved Resolution"*. Review of Scientific Instruments, 1955. 26(12), 1150-1157.

26. Nandi, D. and E. Krishnakumar, "*Dissociative electron attachment to polyatomic molecules: Ion kinetic energy measurements"*. International Journal of Mass Spectrometry, 2010. 289(1), 39-46.

27. Lobo, R.F.M., A.M.C. Moutinho, K. Lacmann, and J. Los, "*Excitation of the Nitro-Group in Nitromethane by Electron-Transfer"*. Journal of Chemical Physics, 1991. 95(1), 166-175.

28. Alizadeh, E., F.F. da Silva, F. Zappa, A. Mauracher, M. Probst, S. Denifl, A. Bacher, T.D. Mark, P. Limao-Vieira, and P. Scheier, "*Dissociative electron attachment to nitromethane"*. International Journal of Mass Spectrometry, 2008. 271(1-3), 15-21.

29. Brooks, P.R., P.W. Harland, and C.E. Redden, "*Steric asymmetry in electron transfer from potassium atoms to oriented nitromethane (CH3NO2) molecules"*. Journal of Physical Chemistry A, 2006. 110(14), 4697-4701.

30. Compton, R.N., H.S. Carman, C. Desfrancois, H. AbdoulCarmine, J.P. Schermann, J.H. Hendricks, S.A. Lyapustina, and K.H. Bowen, "*On the binding of electrons to nitromethane: Dipole and valence bound anions"*. Journal of Chemical Physics, 1996. 105(9), 3472-3478.

31. Compton, R.N., P.W. Reinhardt, and C.D. Cooper, "*Collisional Ionization between Alkali Atoms and Some Methane Derivatives - Electron-Affinities for Ch3no2, Cf3l, and Cf3br"*. Journal of Chemical Physics, 1978. 68(10), 4360-4367.

32. Goebbert, D.J., K. Pichugin, and A. Sanov, "*Low-lying electronic states of CH3NO2 via photoelectron imaging of the nitromethane anion"*. Journal of Chemical Physics, 2009. 131(16), 164308-164308-7.

33. Lecomte, F., S. Carles, C. Desfrancois, and M.A. Johnson, "*Dipole bound and valence state coupling in argon-solvated nitromethane anions"*. Journal of Chemical Physics, 2000. 113(24), 10973-10977.

34. Modelli, A. and M. Venuti, "*Empty level structure and dissociative electron attachment in gas-phase nitro derivatives"*. International Journal of Mass Spectrometry, 2001. 205(1-3), 7-16.

35. Sailer, W., A. Pelc, S. Matejcik, E. Illenberger, P. Scheier, and T.D. Mark, "*Dissociative electron attachment study to nitromethane"*. Journal of Chemical Physics, 2002. 117(17), 7989-7994.

36. Stockdale, J., F.J. Davis, R.N. Compton, and C.E. Klots, "*Production of Negative-Ions from Ch3x Molecules (Ch3no2, Ch3cn, Ch3i, Ch3br) by Electron-Impact and by Collisions with Atoms in Excited Rydberg States"*. Journal of Chemical Physics, 1974. 60(11), 4279-4285.

37. Suess, L., R. Parthasarathy, and F.B. Dunning, "*Rydberg electron transfer to CH3NO2: Lifetimes and characteristics of the product CH3NO2- ions"*. Journal of Chemical Physics, 2003. 119(18), 9532-9537.

38. Walker, I.C. and M.A.D. Fluendy, "*Spectroscopy and dynamics of nitromethane (CH3NO2) and its anionic states"*. International Journal of Mass Spectrometry, 2001. 205(1-3), 171-182.

39. Adamowicz, L., "*Dipole-Bound Anionic State of Nitromethane - Abinitio Coupled Cluster Study with 1st-Order Correlation Orbitals".* Journal of Chemical Physics, 1989. 91(12), 7787-7790.

40. Arenas, J.F., J.C. Otero, D. Pelaez, J. Soto, and L. Serrano-Andres, "*Multiconfigurational second-order perturbation study of the decomposition of the radical anion of nitromethane".* Journal of Chemical Physics, 2004. 121(9), 4127-4132.

41. Gutsev, G.L. and R.J. Bartlett, "*A theoretical study of the valence- and dipole-bound states of the nitromethane anion".* Journal of Chemical Physics, 1996. 105(19), 8785-8792.

42. Sommerfeld, T., "*Coupling between dipole-bound and valence states: the nitromethane anion".* Physical Chemistry Chemical Physics, 2002. 4(12), 2511-2516.

43. Liu, Y., M. Cannon, L. Suess, F.B. Dunning, V.E. Chernov, and B.A. Zon, "*Electron transfer in collisions of dipole-bound anions with polar targets".* Chemical Physics Letters, 2006. 433(1-3), 1-4.

44. Antunes, R., D. Almeida, G. Martins, N.J. Mason, G. Garcia, M.J.P. Maneira, Y. Nunes, and P. Limao-Vieira, "*Negative ion formation in potassium-nitromethane collisions".* Physical Chemistry Chemical Physics, 2010. 12(39), 12513-12519.

45. Brooks, P.R., P.W. Harland, and C.E. Redden, "*Electron transfer from sodium to oriented nitromethane, CH3NO2: Probing the spatial extent of unoccupied orbitals".* Journal of the American Chemical Society, 2006. 128(14), 4773-4778.

46. Sonntag, C., "*The Chemical Basis for Radiation Biology ".* 1987, London: Taylor & Francis

47. Cobut, V., Y. Frongillo, J.P. Patau, T. Goulet, M.J. Fraser, and J.P. Jay-Gerin, "*Monte Carlo simulation of fast electron and proton tracks in liquid water - I. Physical and physicochemical aspects".* Radiation Physics and Chemistry, 1998. 51(3), 229-243.

48. Abouaf, R., J. Pommier, and H. Dunet, "*Negative ions in thymine and 5-bromouracil produced by low energy electrons".* International Journal of Mass Spectrometry, 2003. 226(3), 397-403.

49. Huels, M.A., I. Hahndorf, E. Illenberger, and L. Sanche, "*Resonant dissociation of DNA bases by subionization electrons".* Journal of Chemical Physics, 1998. 108(4), 1309-1312.

50. Denifl, S., S. Ptasinska, G. Hanel, B. Gstir, P. Scheier, M. Probst, B. Farizon, M. Farizon, S. Matejcik, E. Illenberger, and T.D. Mark, "*Electron attachment to uracil, thymine and cytosine".* Physica Scripta, 2004. T110, 252-255.

51. Denifl, S., S. Ptasinska, G. Hanel, B. Gstir, M. Probst, P. Scheier, and T.D. Mark, "*Electron attachment to gas-phase uracil".* Journal of Chemical Physics, 2004. 120(14), 6557-6565.

52. Hanel, G., B. Gstir, S. Denifl, P. Scheier, M. Probst, B. Farizon, M. Farizon, E. Illenberger, and T.D. Mark, "*Electron attachment to uracil: Effective destruction at subexcitation energies".* Physical Review Letters, 2003. 90(18), 188104.

53. Ptasinska, S., S. Denifl, B. Mroz, M. Probst, V. Grill, E. Illenberger, P. Scheier, and T.D. Mark, "*Bond selective dissociative electron attachment to thymine".* Journal of Chemical Physics, 2005. 123(12), 124302-124302-8.

54. Abdoul-Carime, H., S. Gohlke, and E. Illenberger, "*Site-specific dissociation of DNA bases by slow electrons at early stages of irradiation".* Physical Review Letters, 2004. 92(16), 168103.

55. Ptasinska, S., S. Denifl, V. Grill, T.D. Mark, E. Illenberger, and P. Scheier, "*Bond- and site-selective loss of H- from pyrimidine bases".* Physical Review Letters, 2005. 95(9), 093201.

56. Ptasinska, S., S. Denifl, V. Grill, T.D. Mark, P. Scheier, S. Gohlke, M.A. Huels, and E. Illenberger, "*Bond-selective H- ion abstraction from thymine".* Angewandte Chemie-International Edition, 2005. 44(11), 1647-1650.

57. Ptasinska, S., S. Denifl, P. Scheier, E. Illenberger, and T.D. Mark, "*Bond- and site-selective loss of H atoms from nucleobases by very-low-energy electrons (< 3 eV)".* Angewandte Chemie-International Edition, 2005. 44(42), 6941-6943.

58. Desfrancois, C., H. AbdoulCarime, and J.P. Schermann, "*Electron attachment to isolated nucleic acid bases".* Journal of Chemical Physics, 1996. 104(19), 7792-7794.

59. Desfrancois, C., V. Periquet, Y. Bouteiller, and J.P. Schermann, "*Valence and dipole binding of electrons to uracil".* Journal of Physical Chemistry A, 1998. 102(8), 1274-1278.

60. Scheer, A.M., K. Aflatooni, G.A. Gallup, and P.D. Burrow, "*Bond breaking and temporary anion states in uracil and halouracils: Implications for the DNA bases".* Physical Review Letters, 2004. 92(6), 068102.

61. Aflatooni, K., G.A. Gallup, and P.D. Burrow, "*Electron attachment energies of the DNA bases".* Journal of Physical Chemistry A, 1998. 102(31), 6205-6207.

62. Scheer, A.M., C. Silvernail, J.A. Belot, K. Aflatooni, G.A. Gallup, and P.D. Burrow, "*Dissociative electron attachment to uracil deuterated at the N-1 and N-3 positions".* Chemical Physics Letters, 2005. 411(1-3), 46-50.

63. Hendricks, J.H., S.A. Lyapustina, H.L. de Clercq, and K.H. Bowen, "*The dipole bound-to-covalent anion transformation in uracil".* Journal of Chemical Physics, 1998. 108(1), 8-11.

64. Hendricks, J.H., S.A. Lyapustina, H.L. deClercq, J.T. Snodgrass, and K.H. Bowen, "*Dipole bound, nucleic acid base anions studied via negative ion photoelectron spectroscopy".* Journal of Chemical Physics, 1996. 104(19), 7788-7791.

65. Sommerfeld, T., "*Intramolecular electron transfer from dipole-bound to valence orbitals: Uracil and 5-chlorouracil".* Journal of Physical Chemistry A, 2004. 108(42), 9150-9154.

66. Burrow, P.D., G.A. Gallup, A.M. Scheer, S. Denifl, S. Ptasinska, T. Mark, and P. Scheier, "*Vibrational Feshbach resonances in uracil and thymine".* Journal of Chemical Physics, 2006. 124(12), 124310-124310-7.

67. Gianturco, F.A. and R.R. Lucchese, "*Radiation damage of biosystems mediated by secondary electrons: Resonant precursors for uracil molecules".* Journal of Chemical Physics, 2004. 120(16), 7446-7455.

68. Tonzani, S. and C.H. Greene, "*Low-energy electron scattering from DNA and RNA bases: Shape resonances and radiation damage".* Journal of Chemical Physics, 2006. 124(5), 054312-054312-11.

69. Gianturco, F.A., F. Sebastianelli, R.R. Lucchese, I. Baccarelli, and N. Sanna, "*Ring-breaking electron attachment to uracil: Following bond dissociations via evolving resonances".* Journal of Chemical Physics, 2008. 128(17), 174302-174302-8.

70. Takayanagi, T., T. Asakura, and H. Motegi, "*Theoretical Study on the Mechanism of Low-Energy Dissociative Electron Attachment for Uracil".* Journal of Physical Chemistry A, 2009. 113(16), 4795-4801.

71. Sommerfeld, T., "*Electron-induced chemistry of 5-chlorouracil".* Chemphyschem, 2001. 2(11), 677-679.

72. Antunes, R., D. Almeida, G. Martins, N.J. Mason, G. Garcia, M.J. Maneira, Y. Nunes, and P. Limao-Vieira, "*Negative ion formation in potassium-nitromethane collisions".* Physical Chemistry Chemical Physics, 2010. 12(39), 12513-9.

73. Denifl, S., F. Zappa, A. Mauracher, F.F. da Silva, A. Bacher, O. Echt, T.D. Mark, D.K. Bohme, and P. Scheier, "*Dissociative electron attachment to DNA bases near absolute zero temperature: Freezing dissociation intermediates".* Chemphyschem, 2008. 9(10), 1387-1389.

74. Colarusso, P., K.Q. Zhang, B.J. Guo, and P.F. Bernath, "*The infrared spectra of uracil, thymine, and adenine in the gas phase".* Chemical Physics Letters, 1997. 269(1-2), 39-48.

75. Desfrancois, C., H. Abdoulcarime, N. Khelifa, and J.P. Schermann, "*From 1/R to 1/R(2) Potentials - Electron-Exchange between Rydberg Atoms and Polar-Molecules".* Physical Review Letters, 1994. 73(18), 2436-2439.

76. Martin, F., P.D. Burrow, Z.L. Cai, P. Cloutier, D. Hunting, and L. Sanche, "*DNA strand breaks induced by 0-4 eV electrons: The role of shape resonances".* Physical Review Letters, 2004. 93(6), 068101.

77. Denifl, S., S. Matejcik, S. Ptasinska, B. Gstir, M. Probst, P. Scheier, E. Illenberger, and T.D. Mark, "*Electron attachment to chlorouracil: A comparison between 6-ClU and 5-ClU".* Journal of Chemical Physics, 2004. 120(2), 704-709.

78. Abouaf, R. and H. Dunet, "*Structures in dissociative electron attachment cross-sections in thymine, uracil and halouracils".* European Physical Journal D, 2005. 35(2), 405-410.

79. Abouaf, R., J. Pommier, and H. Dunet, "*Electronic and vibrational excitation in gas phase thymine and 5-bromouracil by electron impact".* Chemical Physics Letters, 2003. 381(3-4), 486-494.

80. Abdoul-Carime, H., M.A. Huels, E. Illenberger, and L. Sanche, "*Formation of negative ions from gas phase halo-uracils by low-energy (0-18 eV) electron impact".* International Journal of Mass Spectrometry, 2003. 228(2-3), 703-716.

81. Denifl, S., S. Matejcik, B. Gstir, G. Hanel, M. Probst, P. Scheier, and T.D. Mark, "*Electron attachment to 5-chloro uracil".* Journal of Chemical Physics, 2003. 118(9), 4107-4114.

82. Abdoul-Carime, H., P.C. Dugal, and L. Sanche, "*Damage induced by 1-30 eV electrons on thymine- and bromouracil-substituted oligonucleotides".* Radiation Research, 2000. 153(1), 23-28.

83. Li, X.F., L. Sanche, and M.D. Sevilla, "*Dehalogenation of 5-halouracils after low energy electron attachment: A density functional theory investigation".* Journal of Physical Chemistry A, 2002. 106(46), 11248-11253.

84. Dobrowolski, J.C., J.E. Rode, R. Kolos, M.H. Jamroz, K. Bajdor, and A.P. Mazurek, "*Ar-matrix IR spectra of 5-halouracils interpreted by means of DFT calculations".* Journal of Physical Chemistry A, 2005. 109(10), 2167-2182.

85. Wetmore, S.D., R.J. Boyd, and L.A. Eriksson, "*A theoretical study of 5-halouracils: electron affinities, ionization potentials and dissociation of the related anions".* Chemical Physics Letters, 2001. 343(1-2), 151-158.

86. Dugal, P.C., H. Abdoul-Carime, and L. Sanche, "*Mechanisms for low-energy (0.5-30 eV) electron-induced pyrimidine ring fragmentation within thymine- and halogen-substituted single strands of DNA".* Journal of Physical Chemistry B, 2000. 104(23), 5610-5617.

87. Abdoul-Carime, H. and C. Desfrancois, "*Electrons weakly bound to molecules by dipolar, quadrupolar or polarization forces".* European Physical Journal D, 1998. 2(2), 149-156.